DISSERTATIONES
PHYSICAE
UNIVERSITATIS
TARTUENSIS
116

ARDI LOOT

Enhanced spontaneous parametric down-conversion in plasmonic and dielectric structures

DISSERTATIONES PHYSICAE UNIVERSITATIS TARTUENSIS
116

DISSERTATIONES PHYSICAE UNIVERSITATIS TARTUENSIS
116

ARDI LOOT

Enhanced spontaneous parametric down-conversion in plasmonic and dielectric structures

UNIVERSITY OF TARTU
Press

The study was carried out at the Institute of Physics, University of Tartu, Estonia.

The dissertation was admitted on 05.06.2018 in partial fulfilment of the requirements for the degree of Doctor of Philosophy in Physics, and was allowed for defence by the Council of the Institute of Physics, University of Tartu.

Supervisors: Dr. Vladimir Hizhnyakov, University of Tartu, Estonia
Dr. Valter Kiisk, University of Tartu, Estonia
Dr. Ilmo Sildos, University of Tartu, Estonia

Opponent: Dr. Sergey K. Sekatskii
Laboratory of the Physics of Living Matter,
Ecole polytechnique fédérale de Lausanne, Switzerland

Defence: August 22, 2018, University of Tartu, Estonia

Publication of this thesis was financially supported by Graduate School of Functional materials and technologies receiving funding from the European Regional Development Fund (2014-2020.4.01.16-0027) in University of Tartu, Estonia

ISSN 1406-0647
ISBN 978-9949-77-821-8 (print)
ISBN 978-9949-77-822-5 (pdf)

University of Tartu Press
www.tyk.ee

Contents

List of publications

The thesis is based on the following original publications:

I **A. Loot**, I. Sildos, and V. Hizhnyakov, "Enhanced spontaneous parametric down-conversion in a metal-dielectric interface", *IEEE Xplore*, 7342484, pp. 451–453, 2015.

II **A. Loot**, I. Sildos, V. Kiisk, T. Romann, V. Hizhnyakov, "Steps towards the experimental realization of surface plasmon polariton enhanced spontaneous parametric down-conversion", *Optik*, 171, pp. 557–564, 2018.

III **A. Loot** and V. Hizhnyakov, "Extension of standard transfer-matrix method for three-wave mixing for plasmonic structures", *Applied Physics A*, 123:152(3), pp. 1–7, 2017.

IV **A. Loot** and V. Hizhnyakov, "Modeling of enhanced spontaneous parametric down-conversion in plasmonic and dielectric structures with realistic waves", *Journal of Optics*, 20(055502), pp. 1–15, 2018.

V **A. Loot** and V. Hizhnyakov, "Leaky Dyakonov surface plasmon polaritons for birefringent crystals", *Applied Physics A*, 122:327(4), pp. 1–8, 2016.

Author's contribution

The author's contribution to the publications referred to by their Roman numerals is indicated as follows:

I Numerical modeling and data analysis. Preparing the manuscript and the figures.

II Conducting experimental work, doing the numerical modeling and the data analysis. Preparing the manuscript and the figures.

III Developing the theory for the extension of transfer-matrix method. Writing the program code, doing the numerical modeling and the data analysis. Preparing the manuscript and the figures.

IV Developing the theory for the modeling of spontaneous parametric down-conversion with realistic waves. Writing the program code, doing the numerical modeling and the data analysis. Preparing the manuscript and the figures.

V Developing the program code, doing the numerical modeling and the data analysis. Preparing the manuscript and the figures.

Publications not included in the thesis

1. **A. Loot**, V. Palm, and V. Hizhnyakov, "Numerical simulation of light propagation in metal-coated SNOM tips," *Proc. Est. Acad. Sci.*, 66(4), pp. 430–436, 2017.
2. T. Kangur, V. Kiisk, **A. Loot**, M. Timusk, and M. Järvekülg, "Optical functionality of micro- and nanostructured silica surfaces prepared by a sol-gel phase separation method," *Thin Solid Films*, 622, pp. 11–16, 2017.
3. I. Sildos, **A. Loot**, V. Kiisk, L. Puust, V. Hizhnyakov, A. Yelisseyev, A. Osvet, I. Vlasov, "Spectroscopic study of NE8 defect in synthetic diamond for optical thermometry," *Diamond and Related Materials*, 76, pp. 27–30, 2017.
4. V. Palm, M. Pärs, **A. Loot**, M. Rähn, and V. Hizhnyakov, "On mesoscopic effect of spectral modulation and its potential influence on hyperspectral SNOM imaging results," In: Méndez-Vilas, A. (Ed.). Microscopy and imaging science: practical approaches to applied research and education (610–619). Badajoz (Spain): Formatex Research Center. (Formatex Microscopy book series; 7), 2017.
5. V. Hizhnyakov, **A. Loot**, and S.C. Azizabadi, "Enhanced dynamical Casimir effect for surface and guided waves," *Applied Physics A*, 122:333(4), pp. 1–6, 2016.
6. L. Dolgov, V.I. Kondratiev, **A. Loot**, V. Kiisk, and S. Lange, "Resonant control of fluorescence from aluminium doped zinc oxide films," *Optical and Quantum Electronics*, 48:522(11), pp. 1–10, 2016.
7. A. Šutka, M. Timusk, **A. Loot**, U. Joost, and T. Käämbre, "Polarizable Nanowire Colloids for Power Free Naked Eye Optical Detection of Electrostatic Surface Charges," *Advanced Materials Technologies*, 1(9), pp. 2–4, 2016.
8. A. Šutka, M. Timusk, M. Järvekülg, **A. Loot**, U. Joost, R. Lõhmus and K. Saal, "Counterintuitive increase in optical scattering efficiency during negentropic orientational transition in dilute ZnO nanowire suspensions," *RSC Adv*, 5(126), pp. 104149–104154, 2015.
9. V. Hizhnyakov, **A. Loot**, and S.C. Azizabadi, "Dynamical Casimir effect for surface plasmon polaritons," *Physics Letters A*, 379(5), pp. 501–505, 2015.
10. V. Boiko, G. Dovbeshko, L. Dolgov, V. Kiisk, I. Sildos, **A. Loot**, and V. Gorelik, "Angular shaping of fluorescence from synthetic opal-based photonic crystal.," *Nanoscale Research Letters*, 10(1), pp. 1–7, 2015.

Abbreviations

BBO	beta-barium borate
DFG	difference-frequency generation
DSPPs	Dyakonov surface plasmon polaritons
FFT	fast Fourier transform
GDWs	guided dielectric waves
IML	index matching liquid
LDSPPs	leaky Dyakonov surface plasmon polaritons
LRSPPs	long-range surface plasmon polaritons
NIR	near-infrared
NLTMM	nonlinear transfer-matrix method
OA	optical axis
OR	optical-rectification
PMT	photomultiplier tube
PPLN	periodically poled lithium niobate
QPM	quasi-phase-matching
SFG	sum-frequency generation
SHG	second-harmonic generation
SPDC	spontaneous parametric down-conversion
SPPs	surface plasmon polaritons
TIR	total internal reflection
TMM	transfer-matrix method

1 Introduction

1.1 Introduction and overview

An efficient generation of light in an entangled state has become increasingly important because of perspective applications in quantum optical experiments like quantum teleportation, quantum computing and quantum key distribution. The most common source of entangled photon pairs is a spontaneous parametric down-conversion (SPDC) process in a bulk nonlinear crystal – a spontaneous decay of pump photons into two due to nonlinear interaction with matter. However, the process of SPDC is very inefficient and only a small fraction of pump photons are transformed into photon pairs. The aim of this thesis is to explore the novel idea to enhance the process of SPDC with surface waves both theoretically and experimentally.

The work begins with an overview of the previous work on the enhancement of SPDC. Next, general background for understanding the thesis will be given in chapter 2. Firstly, theoretical basics are introduced to establish common definitions and notations. Secondly, several kinds of surface waves are briefly described along with possible excitation methods. Finally, the process of SPDC is reviewed.

In the first original part of the thesis (chapter 3), the idea of the enhancement of SPDC with surface waves is introduced (publication I) and the experimental work towards the realization of the enhanced SPDC is described (publication II). Theoretical considerations are limited to the calculation of enhancement factors and phase-matching conditions, no detailed modeling of SPDC is attempted.

Next, chapter 4, based on publications III and IV, is devoted to the realistic numerical modeling of SPDC process in structures supporting surface plasmon polaritons (SPPs), long-range SPPs (LRSPPs) and guided dielectric waves (GDWs). The aim of this chapter is to assess the suitability of surface waves for the enhancement of SPDC, compare different types of surface waves and address main limiting factors of the process. An extra care is taken to realistically model the interaction of light with very narrow resonances of LDSPPs and GDWs. To do that, several extensions for transfer-matrix method (TMM) were developed: support for second-order nonlinear processes, calculations with realistic Gaussian beams and the quantum theory of SPDC.

The last original part (chapter 5), based on publication V, focuses on the new variation of leaky Dyakonov SPPs (LDSPPs) in the context of enhanced SPDC. The chapter begins with an introduction to methods used to predict the

existence and to describe the leaky nature of this new kind of waves. The main advantage of discovered LDSPPs, the built-in excitation method, is studied to simplify the structure required to enhance SPDC with surface waves.

Through the entire work, the scope is limited to numerical modeling of the classical parameters of the SPDC like the efficiency of the process. The quantum properties of the generated light are not studied and are left for future work.

Finally, the conclusions are made and the results are discussed in the context of the future work.

1.2 Previous work

A need for a more efficient source of entangled photons than ordinary SPDC in a bulk has been under interest for several decades. Here the previous work in the field of enhanced SPDC will be reviewed.

One of the first steps towards enhanced SPDC was reported in 1999 by P. G. Kwiat, et. al. [1]. By using a two-crystal geometry, the enhancement of the rate of the generation of polarization-entangled photon pairs by a factor of ten was experimentally verified. The main limitation of usual type-II phase-matched SPDC was, that only a small part of the generated photon pairs was polarization entangled (only along two special directions) [2]. The enhancement of the two-crystal structure results from the fact, that all of the photon pairs generated are entangled [1]. Although the process of SPDC itself was not enhanced (only the generation of polarization-entangled states), the work of P. G. Kwiat, et. al. was one of the first to explore the field of enhanced SPDC.

Next, the potential of resonant optical cavities was realized for the enhancement of SPDC [3–8]. The first proof-of-concept demonstration of the use of a cavity for a pump laser was conducted in 2000 by M. Oberparleiter, et. al. [3]. They used resonant enhancement of optical cavities, tuned to the frequency of the pump beam, to increase the nonlinear interaction with a nonlinear crystal and experimentally demonstrated an enhancement factor around 7 (theoretically up to 50) [3]. Alternatively, resonant cavities at the signal and idler frequencies could be used to increase the correlation time between conjugate photons while sustaining the rates of the photon pairs [5, 7].

Shortly after, in 2001, a new kind of entangled photon pair source based on periodically poled lithium niobate (PPLN) waveguides was proposed [9]. They reported huge enhancement, more than four orders of magnitude, in the rate of the pair generation. Experimentally conversion rate of 10^{-6} pairs per pump photon was demonstrated. The effect here is twofold. Firstly, the periodical reversal of the sign of the second-order susceptibility allows

quasi-phase-matching (QPM) – especially beneficial in highly nonlinear crystals where phase-matching is not otherwise possible. I.e. it allows using the highest nonlinear coefficient of lithium niobate otherwise not accessible. Secondly, the SPDC in waveguides allows the confinement of the pump beam over the interaction length. In usual SPDC setup, the interaction length is limited by the transverse walk-off, in the case of the waveguide structure, it is not an issue, as the signal is generated into a single mode of the waveguide [10].

The field of the enhancement of SPDC in waveguides has since attracted a lot of attention. Different materials have been explored [11], energy-time entangled photon pair sources have been reported [12], different splitting ratios and pump wavelengths have been demonstrated [13–15]. Moreover, the generation of SPDC in nanophotonic waveguides [16] and the heralded single-photon source for telecom wavelengths have been demonstrated [17]. The use of periodically poled materials and QPM has not been limited only to the waveguides, the enhanced generation of SPDC in bulk periodically poled potassium titanyl phosphate was demonstrated in Ref. [18].

More recently, the enhancement of SPDC was theoretically studied in photonic crystals [19, 20], in negative index materials [21] and in semiconductor Bragg reflector waveguides [22, 23].

The topic of this thesis, enhancement of SPDC by plasmonic and dielectric modes, is virtually unexplored. The idea of SPP-enhanced SPDC is only mentioned in two papers by the same group [24, 25]. Their approach is based on k-space spectroscopy to probe plasmonic enhancement of second-harmonic [24] and sum-frequency generation [25], however, they also recognize the importance of the reverse process (plasmonically enhanced SPDC). In Ref. [24] they mention "A striking example would be the inverse process to plasmon SHG, namely, parametric down-conversion, which could be a source of entangled SP pairs at compact length scales." and in Ref. [25] "The inverse of the observed nonlinear interaction – an exotic form of parametric down-conversion – would act as a source of surface plasmons in the near-field that are quantum correlated with photons in the far-field.". No work towards plasmonically enhanced SPDC is attempted in these papers.

2 Background

2.1 Theoretical basics

In the entire work, bold mathematical symbols represent vector or matrix values if not denoted otherwise. The position vector in 3D Cartesian coordinate system is given by $\mathbf{r} = x\hat{\mathbf{x}} + y\hat{\mathbf{y}} + z\hat{\mathbf{z}}$, where $\hat{\mathbf{x}}$, $\hat{\mathbf{y}}$ and $\hat{\mathbf{z}}$ denote the unit vectors. Hat symbol represents unit vectors only in the case of symbols x, y and z, otherwise, hat symbol is used for representing column vectors

$$\hat{\mathbf{M}} = \begin{bmatrix} M^{+} \\ M^{-} \end{bmatrix}, \tag{2.1}$$

for compact representation of forward- (M^{+}) and backward-propagating (M^{-}) components (e.g. incident/transmitted and reflected fields). If x, y or z symbol is used in the subscript of the vector, then it represents the noted vector component.

2.1.1 Maxwell equations

Maxwell equations are the base equations for the propagation of electromagnetic fields. In general form, the macroscopic Maxwell equations are given by

$$\nabla \times \mathbf{E}(\mathbf{r}, t) = -\frac{\partial \mathbf{B}(\mathbf{r}, t)}{\partial t}, \tag{2.2}$$

$$\nabla \times \mathbf{H}(\mathbf{r}, t) = \frac{\partial \mathbf{D}(\mathbf{r}, t)}{\partial t} + \mathbf{j}(\mathbf{r}, t), \tag{2.3}$$

$$\nabla \cdot \mathbf{D}(\mathbf{r}, t) = \rho(\mathbf{r}, t), \tag{2.4}$$

$$\nabla \cdot \mathbf{B}(\mathbf{r}, t) = 0, \tag{2.5}$$

where $\nabla = \frac{\partial}{\partial x}\hat{\mathbf{x}} + \frac{\partial}{\partial y}\hat{\mathbf{y}} + \frac{\partial}{\partial z}\hat{\mathbf{z}}$ denotes the Nabla operator, $\mathbf{E}$ the electric field, $\mathbf{H}$ the magnetic field, $\mathbf{D}$ the electric displacement, $\mathbf{B}$ the magnetic induction, $\mathbf{j}$ the free current density, ρ the free charge density and t the time [26]. The electric displacement and the magnetic induction are usually discussed in terms of the macroscopic polarization $\mathbf{P}$ and magnetization $\mathbf{M}$

$$\mathbf{D}(\mathbf{r},t) = \varepsilon_0 \mathbf{E}(\mathbf{r},t) + \mathbf{P}(\mathbf{r},t), \quad (2.6)$$

$$\mathbf{B}(\mathbf{r},t) = \mu_0 [\mathbf{H}(\mathbf{r},t) + \mathbf{M}(\mathbf{r},t)], \quad (2.7)$$

where ε_0 and μ_0 are the permittivity and the permeability of vacuum, respectively. The macroscopic polarization $\mathbf{P}$ and magnetization $\mathbf{M}$ describe how the material behaves under the influence of the electric $\mathbf{E}$ and magnetic field $\mathbf{H}$, respectively. In order to solve Maxwell equations, these material relations, also known as constitutive relations, must be defined.

2.1.2 Linear medium

2.1.2.1 Wave equation

Maxwell equations defined by Eqs. 2.2 – 2.7 are general. However, to simplify the algebra often several assumptions are made. In this work, we assume that in the case of a linear medium:

- The system interacts only with a harmonic monochromatic light with frequency ω. As a consequence, the time ($e^{-i\omega t}$) and the space ($\mathbf{E}(\mathbf{r})$) dependence of the field (electric field given as an example) could be separated
$$\mathbf{E}(\mathbf{r},t) = \mathbf{E}(\mathbf{r}) e^{-i\omega t} + c.c, \quad (2.8)$$
where *c.c.* denotes complex conjugate.

- The electric response of materials is linear and materials are not spatially dispersive
$$\mathbf{P}(\mathbf{r}) = \varepsilon_0 \boldsymbol{\chi}(\omega) \mathbf{E}(\mathbf{r}), \quad (2.9)$$
where χ denote the electric susceptibility tensor. Equivalently from Eq. 2.6
$$\mathbf{D}(\mathbf{r}) = \varepsilon_0 \boldsymbol{\varepsilon}(\omega) \mathbf{E}(\mathbf{r}), \quad (2.10)$$
where $\boldsymbol{\varepsilon}(\omega) = 1 + \boldsymbol{\chi}(\omega)$ is dielectric permittivity tensor. In the case of isotropic medium, the electric susceptibility and dielectric permittivity tensors reduce to a scalar.

- Materials have no magnetic response ($\mathbf{M}(\mathbf{r}) = 0$).

- There are no free currents or charges ($\mathbf{j}(\mathbf{r},t) = 0$ and $\rho(\mathbf{r},t) = 0$). The effect of conduction currents is incorporated into constitutive relations.

- Optical medium is piecewise homogeneous. On the boundaries, the tangential components of $\mathbf{E}(\mathbf{r})$ and $\mathbf{H}(\mathbf{r})$ are continuous.

In such case, the Maxwell equations reduce to

$$\begin{aligned} \nabla \times \mathbf{E}(\mathbf{r}) &= i\omega\mu_0 \mathbf{H}(\mathbf{r}), && (2.11) \\ \nabla \times \mathbf{H}(\mathbf{r}) &= -i\omega\varepsilon_0 \boldsymbol{\varepsilon}(\omega) \mathbf{E}(\mathbf{r}), && (2.12) \\ \nabla \cdot \mathbf{E}(\mathbf{r}) &= 0, && (2.13) \\ \nabla \cdot \mathbf{H}(\mathbf{r}) &= 0. && (2.14) \end{aligned}$$

Eqs. 2.11 - 2.14 could be combined to a single wave equation

$$\nabla^2 \mathbf{E}(\mathbf{r}) + \frac{\omega^2}{c^2} \boldsymbol{\varepsilon}(\omega) \mathbf{E}(\mathbf{r}) = 0, \tag{2.15}$$

also called Helmholtz equation. One of the simplest solutions of Helmholtz equation (Eq. 2.15) is an infinite plane wave (or the sum of plane waves)

$$\mathbf{E}(\mathbf{r}) = \mathbf{A} e^{i\mathbf{k}\cdot\mathbf{r}}, \tag{2.16}$$

where $\mathbf{A}$ is a amplitude vector, $\mathbf{k}$ is a wavevector with condition $|\mathbf{k}| = \omega n(\omega)/c$ and

$$n(\omega) = \sqrt{\varepsilon(\omega)} \tag{2.17}$$

is a refractive index.

The refractive index may be complex to account for losses

$$n(\omega) = \tilde{n} + i\tilde{\kappa}, \tag{2.18}$$

where $\tilde{n}$ is the real and $\tilde{\kappa}$ is the imaginary part, also named to extinction coefficient, of the refractive index. It also follows, that the wavevector may be complex.

2.1.2.2 Isotropic medium

In the case of isotropic medium, the dielectric permittivity reduces from a second rank tensor to a scalar. The consequence of this is the decoupling of polarizations: two different polarizations appear (both determined only by one scalar field), that could be solved separately. If the plane of incidence is taken to be xz-plane, then p-polarized (also called to TM polarization) electrical field has only x- and z-components and s-polarized (also TE polarization) electrical field has only y-component.

For example, s-polarized monochromatic electrical field is given by $\mathbf{E}(\mathbf{r}) = E_y(\mathbf{r})\,\hat{\mathbf{y}}$ and from Eq. 2.11 the nonzero components of the magnetic field are

$$\mathbf{H}(\mathbf{r}) = \frac{1}{i\omega\mu_0}\left[\frac{\partial E_y(\mathbf{r})}{\partial z}\hat{\mathbf{x}} - \frac{\partial E_y(\mathbf{r})}{\partial x}\hat{\mathbf{z}}\right]. \tag{2.19}$$

It is clear, that the only independent variable here is the $E_y(\mathbf{r})$, as the magnetic field directly follows from it.

Similarly, for p-polarized monochromatic wave, the only independent variable is $H_y(\mathbf{r})$ and the corresponding electrical field components are given by

$$\mathbf{E}(\mathbf{r}) = \frac{-1}{i\omega\varepsilon_0\varepsilon(\omega)}\left[\frac{\partial H_y(\mathbf{r})}{\partial z}\hat{\mathbf{x}} - \frac{\partial H_y(\mathbf{r})}{\partial x}\hat{\mathbf{z}}\right]. \tag{2.20}$$

2.1.2.3 Anisotropic medium

In the case of electrically anisotropic mediums, the dielectric permittivity in Eq. 2.15 is given by a 2-rank tensor

$$\boldsymbol{\varepsilon} = \begin{bmatrix} \varepsilon_{xx} & \varepsilon_{xy} & \varepsilon_{xz} \\ \varepsilon_{yx} & \varepsilon_{yy} & \varepsilon_{yz} \\ \varepsilon_{zx} & \varepsilon_{zy} & \varepsilon_{zz} \end{bmatrix} \tag{2.21}$$

instead of a scalar: electric field in one direction can cause polarization in the other direction [27]. However, not all variables of the dielectric tensor are independent. It turns out, that it is always possible to select the axes (principal axes 1, 2, 3) so that the dielectric tensor is diagonalized

$$\boldsymbol{\varepsilon} = \boldsymbol{S}_x(\xi)\cdot\boldsymbol{S}_z(\psi)\cdot\begin{bmatrix} \varepsilon_1 & 0 & 0 \\ 0 & \varepsilon_2 & 0 \\ 0 & 0 & \varepsilon_3 \end{bmatrix}\cdot\boldsymbol{S}_z(-\psi)\cdot\boldsymbol{S}_x(-\xi), \tag{2.22}$$

where $\boldsymbol{S}_x(\xi)$ and $\boldsymbol{S}_z(\psi)$ are the rotation matrices around the x- and z-axis, respectively [28]. Now five independent variables remain: three components of the dielectric tensor (ε_1, ε_2, ε_3) and two angles of rotation of the principal axes in respect to laboratory frame (ξ, ψ). Often refractive index is preferred over dielectric permittivity (equivalent), connected in the same way as in the case of isotropic medium (Eq. 2.17).

Moreover, in the case of uniaxial crystals, only two elements of the dielectric permittivity tensor are independent

$$\boldsymbol{\varepsilon} = \begin{bmatrix} \varepsilon_o & 0 & 0 \\ 0 & \varepsilon_o & 0 \\ 0 & 0 & \varepsilon_e \end{bmatrix}, \tag{2.23}$$

where ε_o and ε_e represent ordinary and extraordinary dielectric permittivities, respectively and the optical axis (OA) is along the third principal axis. If the light travels along the OA, the propagation is only influenced by the ordinary refractive index (dielectric permittivity) of the uniaxial crystal despite the polarization. In the case of any other direction of propagation, two different waves appear that feel the material differently (birefringence): the ordinary beam (dielectric permittivity ε_o) and the extraordinary beam (dielectric permittivity between ε_o and ε_e). The ordinary and the extraordinary beams are independent and are the natural choice of the polarization base like p- and s-polarization in the case of isotropic medium (Sec. 2.1.2.2).

Uniaxial crystals are classified into positive ($\varepsilon_e > \varepsilon_0$) and negative ($\varepsilon_e < \varepsilon_0$) crystals and described by the anisotropy parameter

$$\eta = \frac{\varepsilon_e}{\varepsilon_o} - 1. \tag{2.24}$$

2.1.3 Second-order nonlinear medium

2.1.3.1 Nonlinear wave equation

In the case of nonlinear mediums, it is assumed similarly to Sec. 2.1.2 that materials have no magnetic response, there are no free currents or charges and optical mediums are piecewise homogeneous. We also assume, that we are working with two harmonic monochromatic light beams (also named pump beams). The time-dependent electrical field is then given by (analogously to Eq. 2.8)

$$\mathbf{E}(\mathbf{r},t) = \mathbf{E}_1(\mathbf{r})\, e^{-i\omega_1 t} + \mathbf{E}_2(\mathbf{r})\, e^{-i\omega_2 t} + c.c., \tag{2.25}$$

where 1 and 2 denote the first and the second beam, respectively. In the case of second-order nonlinear medium, the macroscopic polarization $\mathbf{P}(\mathbf{r},t)$ depends also on the second power of the electric field

$$\begin{aligned} \mathbf{E}(\mathbf{r},t)^2 \;=\; & \mathbf{E}_1(\mathbf{r})^2\, e^{-i2\omega_1 t} + c.c. + \\ & \mathbf{E}_2(\mathbf{r})^2\, e^{-i2\omega_2 t} + c.c. + \\ & 2\mathbf{E}_1(\mathbf{r})\,\mathbf{E}_2(\mathbf{r})\, e^{-i(\omega_1+\omega_2)t} + c.c. + \\ & 2\mathbf{E}_1(\mathbf{r})\,\mathbf{E}_2^*(\mathbf{r})\, e^{-i(\omega_1-\omega_2)t} + c.c. + \\ & 2\left(\mathbf{E}_1(\mathbf{r})\,\mathbf{E}_1^*(\mathbf{r}) + \mathbf{E}_2(\mathbf{r})\,\mathbf{E}_2^*(\mathbf{r})\right). \end{aligned} \tag{2.26}$$

It is evident, that new frequencies arise in the second-order nonlinear medium leading to second-harmonic generation (SHG), sum-frequency generation (SFG), difference-frequency generation (DFG) and optical rectification (OR). In practice, only one of those processes is concurrently under interest and the others

are ignored. It allows writing the polarization similar to the linear case (Eq. 2.9)

$$\mathbf{P}(\mathbf{r}) = \varepsilon_0 \chi(\omega)\, \mathbf{E}(\mathbf{r}) + \mathbf{P}_{NL}(\mathbf{r}), \tag{2.27}$$

where $\mathbf{P}_{NL}(\mathbf{r})$ is addition to ordinary linear polarization and depends on the process under interest

$$\begin{aligned}
\mathbf{P}_{NL}(\mathbf{r};\omega = 2\omega_1) &= \varepsilon_0 \chi^{(2)} : \mathbf{E}_1(\mathbf{r})\, \mathbf{E}_1(\mathbf{r}), \quad \text{(SHG)} && (2.28)\\
\mathbf{P}_{NL}(\mathbf{r};\omega = 2\omega_2) &= \varepsilon_0 \chi^{(2)} : \mathbf{E}_2(\mathbf{r})\, \mathbf{E}_2(\mathbf{r}), \quad \text{(SHG)} && (2.29)\\
\mathbf{P}_{NL}(\mathbf{r};\omega = \omega_1 + \omega_2) &= \varepsilon_0 \chi^{(2)} : \mathbf{E}_1(\mathbf{r})\, \mathbf{E}_2(\mathbf{r}), \quad \text{(SFG)} && (2.30)\\
\mathbf{P}_{NL}(\mathbf{r};\omega = \omega_1 - \omega_2) &= \varepsilon_0 \chi^{(2)} : \mathbf{E}_1(\mathbf{r})\, \mathbf{E}_2^*(\mathbf{r}) \quad \text{(DFG)} && (2.31)
\end{aligned}$$

and ω denotes the newly generated frequency. Through the entire work, the pump beams are denoted by numbers 1, 2 and the generated beam has no subscript. The strength of the nonlinear interaction is given by second-order nonlinear susceptibility tensor $\chi^{(2)}$ and : denotes the double product [29]. Note, that the frequency dispersion of second-order nonlinear susceptibility tensor is non explicitly stated in this work. Often effective nonlinearity $\chi^{(2)}_{eff}$ is used to reduce the susceptibility tensor to a scalar by taking into account the polarizations of the pump beams so that

$$\chi^{(2)}_{eff} \|\mathbf{E}_1(\mathbf{r})\| \, \|\mathbf{E}_2(\mathbf{r})\| \cdot \frac{\mathbf{P}_{NL}}{\|\mathbf{P}_{NL}\|} = \chi^{(2)} : \mathbf{E}_1(\mathbf{r})\, \mathbf{E}_2(\mathbf{r}), \tag{2.32}$$

where $\|\mathbf{E}\| = \sqrt{|E_x|^2 + |E_y|^2 + |E_z|^2}$ denotes L2-norm of complex vector.

The polarization defined by Eq. 2.27 leads to the nonlinear wave equation

$$\nabla^2 \mathbf{E}(\mathbf{r}) + \frac{\omega^2}{c^2} \varepsilon(\omega)\, \mathbf{E}(\mathbf{r}) = -\frac{\omega^2}{\varepsilon_0 c^2} \mathbf{P}_{NL}(\mathbf{r}) + \nabla\left(\nabla \cdot \mathbf{E}(\mathbf{r})\right), \tag{2.33}$$

where the term $\nabla(\nabla \cdot \mathbf{E}(\mathbf{r}))$ is often neglected or incorporated into effective nonlinear polarization.

2.1.3.2 Non-depleted pump wave approximation

As an example, the wave equations of the DFG are

$$\nabla^2 \mathbf{E}_1(\mathbf{r}) + \frac{\omega_1^2}{c^2}\varepsilon(\omega_1)\mathbf{E}_1(\mathbf{r}) = -\frac{\omega_1^2}{c^2}\chi^{(2)} : \mathbf{E}_2(\mathbf{r})\mathbf{E}(\mathbf{r}), \tag{2.34}$$

$$\nabla^2 \mathbf{E}_2(\mathbf{r}) + \frac{\omega_2^2}{c^2}\varepsilon(\omega_2)\mathbf{E}_2(\mathbf{r}) = -\frac{\omega_2^2}{c^2}\chi^{(2)} : \mathbf{E}_1(\mathbf{r})\mathbf{E}^*(\mathbf{r}), \tag{2.35}$$

$$\nabla^2 \mathbf{E}(\mathbf{r}) + \frac{\omega^2}{c^2}\varepsilon(\omega)\mathbf{E}(\mathbf{r}) = -\frac{\omega^2}{c^2}\chi^{(2)} : \mathbf{E}_1(\mathbf{r})\mathbf{E}_2^*(\mathbf{r}), \tag{2.36}$$

where the first two describe pump beams (subscripts 1 and 2) and the last one describes the DFG beam (no subscript, $\omega = \omega_1 - \omega_2$). It is evident, that these three wave equations are coupled. The generation of the difference-frequency depletes the first pump beam and amplifies both the second pump beam and the generated beam. However often, if the nonlinear interaction is very weak (the usual case), non-depleted pump beam approximation can be made. Essentially it discards the right-hand sides of Eqs. 2.34 and 2.35 reducing wave equations to ordinary Helmholtz equations. Now pump beams could be solved independently and the right-hand side of the Eq. 2.36 could be precalculated.

2.1.3.3 Solution to the nonlinear wave equation

In Sec. 2.1.2.1 we noted that the simplest solution of linear wave equation (Helmholtz equation) is a simple plane wave. In this section, we find the solution for the nonlinear wave equation (Eq. 2.33) by using non-depleted pump wave approximation.

Let's assume for now, that pump waves are given as a sum of forward- and backward-propagating plane waves (i.e. incident/transmitted and reflected beams)

$$\mathbf{E}_k(\mathbf{r}) = \mathbf{E}_k^+(\mathbf{r}) + \mathbf{E}_k^-(\mathbf{r}) = \mathbf{A}_k^+ e^{i\mathbf{k}_k^+\cdot\mathbf{r}} + \mathbf{A}_k^- e^{i\mathbf{k}_k^-\cdot\mathbf{r}}, \tag{2.37}$$

where subscript $k \in \{1,2\}$ represent the index of the pump wave. In such case, the nonlinear polarization (Eq. 2.31) of DFG (as an example) could be expressed also as a forward- and backward-propagating parts as

$$\mathbf{P}_{NL}(\mathbf{r}) = \varepsilon_0\chi^{(2)} : \mathbf{E}_1(\mathbf{r})\mathbf{E}_2^*(\mathbf{r}) = \mathbf{P}_{NL}^+(\mathbf{r}) + \mathbf{P}_{NL}^-(\mathbf{r}), \tag{2.38}$$

$$\mathbf{P}_{NL}^\pm(\mathbf{r}) = \mathbf{p}_s^\pm e^{i\mathbf{k}_s^\pm\cdot\mathbf{r}} + \mathbf{p}_a^\pm e^{i\mathbf{k}_a^\pm\cdot\mathbf{r}}, \tag{2.39}$$

where $\mathbf{k}_s^{\pm} = \mathbf{k}_1^{\pm} - \mathbf{k}_2^{\pm *}$ and $\mathbf{k}_a^{\pm} = \mathbf{k}_1^{\pm} + \mathbf{k}_2^{\pm *}$ are nonlinear source wavevectors (denoted by s and a by arbitrary choice). Note that the magnitude of the nonlinear source wavevectors are not equal to an ordinary expression $\left|\mathbf{k}_{s|a}^{\pm}\right| \neq \omega n\left(\omega\right)/c$. The terms $\mathbf{p}_{s|a}^{\pm}$ (subscript $s|a$ means, that the expression holds for both nonlinear source waves) are the amplitudes of the nonlinear polarization and are given by

$$\mathbf{p}_s^{\pm} = \varepsilon_0 \chi^{(2)} : \mathbf{A}_1^{\pm} \mathbf{A}_2^{\pm *}, \tag{2.40}$$

$$\mathbf{p}_a^{\pm} = \varepsilon_0 \chi^{(2)} : \mathbf{A}_1^{\pm} \mathbf{A}_2^{\mp *}. \tag{2.41}$$

It is evident, that if the amplitudes of pump plane waves $\mathbf{A}_k^{\pm}$ are known, then the calculation of nonlinear polarization given by Eq. 2.38 is straightforward. As both, the forward- and backward-propagating waves must satisfy the nonlinear wave equation, it is convenient to use column vectors introduced in Sec. 2.1. Then the nonlinear wave equation could be written as

$$\nabla^2 \hat{\mathbf{E}}\left(\mathbf{r}\right) + \frac{\omega^2}{c^2} \varepsilon\left(\omega\right) \hat{\mathbf{E}}\left(\mathbf{r}\right) = -\frac{\omega^2}{\varepsilon_0 c^2} \left[\hat{\mathbf{p}}_s e^{i\hat{\mathbf{k}}_s \cdot \mathbf{r}} + \hat{\mathbf{p}}_a e^{i\hat{\mathbf{k}}_a \cdot \mathbf{r}}\right]. \tag{2.42}$$

The solution of the nonlinear wave equation is no longer a single plane wave because of the additional source terms on the right-hand side of Eq. 2.42. The general solution of Eq. 2.42 consists of a sum of homogeneous (linear wave equation) and inhomogeneous solutions

$$\hat{\mathbf{E}}\left(\mathbf{r}\right) = \hat{\mathbf{A}} e^{i\hat{\mathbf{k}} \cdot \hat{\mathbf{r}}} + \hat{\mathbf{B}}_s e^{i\hat{\mathbf{k}}_\mathbf{s} \cdot \hat{\mathbf{r}}} + \hat{\mathbf{B}}_a e^{i\hat{\mathbf{k}}_\mathbf{a} \cdot \hat{\mathbf{r}}}. \tag{2.43}$$

The amplitudes of the inhomogeneous waves could be easily found by substituting Eq. 2.43 into Eq. 2.42

$$\mathbf{B}_{s|a}^{+} = -\frac{\omega^2}{c^2 \varepsilon_0} \frac{\mathbf{p}_{s|a}^{+}}{k^2 - k_{s|a}^2}, \tag{2.44}$$

$$\mathbf{B}_{s|a}^{-} = -\frac{\omega^2}{c^2 \varepsilon_0} \frac{\mathbf{p}_{s|a}^{-}}{k^2 - k_{s|a}^2} e^{ik_{s|a}d}. \tag{2.45}$$

Note, that the additional phase factor $e^{ik_{s|a}d}$ for backward-propagating inhomogeneous wave is added for compact notation used in Sec. 4.2.3, where d denotes the thickness of the nonlinear medium. Also note, that the only unknown of the solution given by Eq. 2.43 is the amplitude of the homogeneous plane wave $\hat{\mathbf{A}}$, like in the case of linear medium.

The magnetic field follows from the electrical field and is given by

$$\hat{\mathbf{H}}(\mathbf{r}) = \frac{1}{\omega\mu_0}\left[\left(\hat{\mathbf{k}}\times\hat{\mathbf{E}}(\mathbf{r})\right)+\left(\left(\hat{\mathbf{k}}_s-\hat{\mathbf{k}}\right)\times\hat{\mathbf{B}}_s\right)e^{i\hat{\mathbf{k}}_s\cdot\mathbf{r}}+ \left(\left(\hat{\mathbf{k}}_a-\hat{\mathbf{k}}\right)\times\hat{\mathbf{B}}_a\right)e^{i\hat{\mathbf{k}}_a\cdot\mathbf{r}}\right]. \tag{2.46}$$

The final solution is given by the sum of forward- and backward-propagating waves $\mathbf{E}(\mathbf{r}) = \mathbf{E}^+(\mathbf{r}) + \mathbf{E}^-(\mathbf{r})$ and $\mathbf{H}(\mathbf{r}) = \mathbf{H}^+(\mathbf{r}) + \mathbf{H}^-(\mathbf{r})$.

2.1.3.4 A simple model for DFG

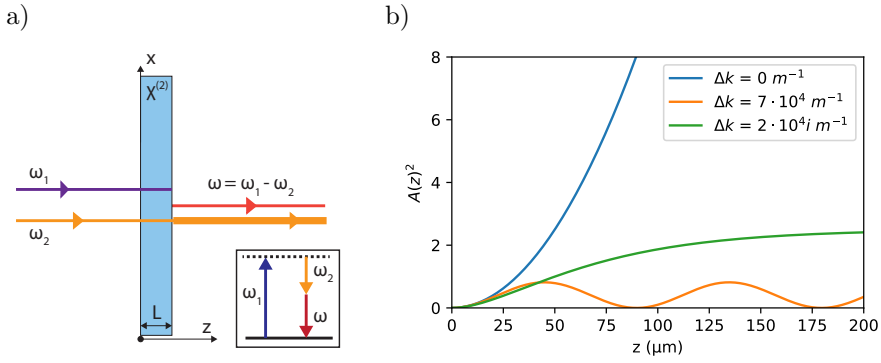

Figure 2.1: a) An example of a DFG in a nonlinear crystal with a thickness L and a second-order susceptibility $\chi^{(2)}$. Pump lasers have frequencies ω_1 and ω_2 and the generated beam has frequency ω. b) The dependence of signal buildup curves on the phase mismatch factor Δk.

As a concrete example, let's look the generation of DFG in a nonlinear crystal (see Fig. 2.1a). The medium is linear in semi-infinite half-spaces ($z < 0$ and $z > L$) and nonlinear in $0 \leq z \leq L$. The refractive indices of all mediums are the same. The pump plane waves are propagating in z-direction ($\mathbf{k}_1^+ = k_1\hat{\mathbf{z}}$ and $\mathbf{k}_2^+ = k_2\hat{\mathbf{z}}$) and have only forward-propagating parts

$$\mathbf{E}_k(\mathbf{r}) = \mathbf{E}_k^+(\mathbf{r}) = \mathbf{A}_k^+ e^{i\mathbf{k}_k^+\cdot\mathbf{r}}. \tag{2.47}$$

The nonlinear polarization amplitudes follow from Eqs. 2.40 – 2.41 and the only non-zero component is

$$\mathbf{p}_s^+ = \varepsilon_0\chi^{(2)} : \mathbf{A}_1^+\mathbf{A}_2^{+*}. \tag{2.48}$$

To solve the nonlinear wave equation (Eq. 2.42) the ansatz given by Eq. 2.43 must be used. The continuity of tangential components of electric and magnetic fields at the boundary $z = 0$ allows expressing the amplitude of the DFG wave in a nonlinear medium

$$A(z) = \frac{\omega^2 \chi^{(2)}_{eff} A_1 A_2}{c^2 k_z} \cdot \frac{e^{i\Delta k z} - 1}{\Delta k}, \tag{2.49}$$

where $\chi^{(2)}_{eff}$ is the effective nonlinearity, $A_k = \|\mathbf{A}_k\|$ denotes the amplitude of the pump waves, k_z is the wavevector component along the direction of propagation of the generated wave, $\Delta k = k_1 - k_2 - k$ is a phase-mismatch factor.

The effect of phase matching is illustrated in Fig. 2.1b. In the case of a perfect phase-matching ($\Delta k = 0$), the intensity ($\propto A(z)^2$) of the generated wave increases as $\propto z^2$. Here we name it as a coherent buildup of the generated signal. If the phase mismatch is not zero (e.g. due to the refractive index dispersion), then the buildup of the signal is disrupted by the destructive interference (see the orange curve in Fig. 2.1b) and no efficient generation of DFG is possible. If a nonlinear material has losses, then Δk can have a significant imaginary component. In such a case, the signal will reach some limiting amplitude after a characteristic length

$$\delta_c = \frac{1}{2\ \mathrm{Im}\left[\Delta k\right]} \tag{2.50}$$

of propagation and no further buildup is possible (the green curve in Fig. 2.1b).

By using Poynting law, it is possible to rewrite the Eq. 2.49 also in terms of powers

$$P = P_1 \frac{\chi^{(2)}_{eff} |A_2|^2}{k_{z1} k_z} \frac{\omega^3 \omega_1}{c^4} L^2 \mathrm{sinc}^2\left(\frac{\Delta k L}{2}\right), \tag{2.51}$$

where P_1 and P are the powers of the pump laser and DFG signal, respectively.

2.1.4 Angular spectrum representation

Angular spectrum representation is a general technique to describe optical fields in a homogeneous medium and it is especially useful in the case of propagation and focusing of laser beams. Mathematically it is given by

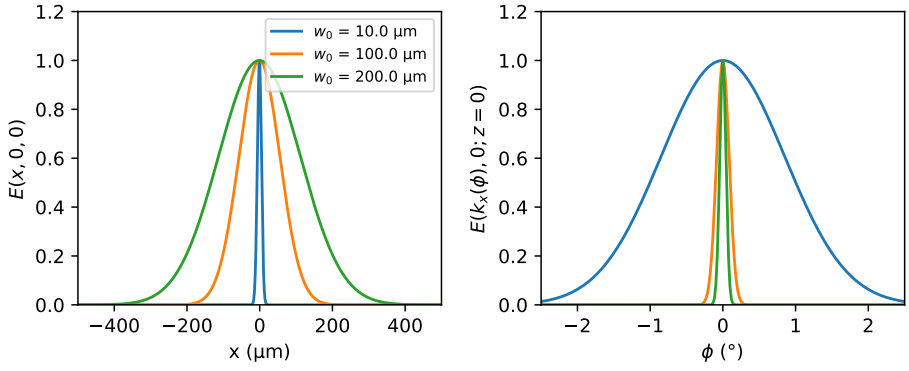

Figure 2.2: a) The profiles of Gaussian beams with different waist sizes (w_0) at plane $z = 0$. b) The amplitudes of plane wave components traveling to different directions of Gaussian beams given in Fig. 2.2a.

$$\mathbf{E}(x, y, z) = \iint_{-\infty}^{\infty} \mathbf{E}(k_x, k_y; z = 0)\, e^{i(k_x x + k_y y + k_z z)} dk_x dk_y, \tag{2.52}$$

where $\mathbf{E}(k_x, k_y; z = 0) = \mathcal{F}[\mathbf{E}(x, y, 0)]$ is the Fourier transform of the electrical fields at plane $z = 0$ and $k_z = \sqrt{k^2 - k_x^2 - k_y^2}$ follows from the fixed magnitude of the wavevector. The selection of z-axis is arbitrary, however, in the case of laser beams, it is convenient to use the axis of propagation. The Eq. 2.52 expresses two important properties. Firstly, in the homogeneous medium, we only have to know the fields at one plane ($\mathbf{E}(x, y, 0)$) – we can calculate the fields everywhere by Eq. 2.52. Secondly, the fields are just a sum of plane waves – under the integration we just have plane waves propagating to different directions with different amplitudes.

As an example, let's look the propagation of a Gaussian beam along the z-axis. For simplicity lets ignore y-axis, so only x- and z-coordinates remain. The cross sections of Gaussian beams with different waist sizes (w_0) are shown in Fig. 2.2a and Fourier transforms, also Gaussian profiles, are shown in Fig. 2.2b, where the angle $\varphi = \mathrm{asin}(k_x/k)$ is between the wavevector and the z-axis. It is evident, that narrow Gaussian beam ($w_0 = 10\,\mu$m) has wider angular spread – the beam requires the inclusion of plane waves traveling also at larger angles to the z-axis. Also the contrary is true, if the Gaussian beam is taken to be wider ($w_0 = 200\,\mu$m), then the angular spread is respectively narrower.

As an example, angular spectrum representation (Eq. 2.52) is used to calculate the propagation of $10\,\mu$m wide Gaussian beam, when only its cross section at plane $z = 0$ is known. The field distribution is shown in Fig. 2.3.

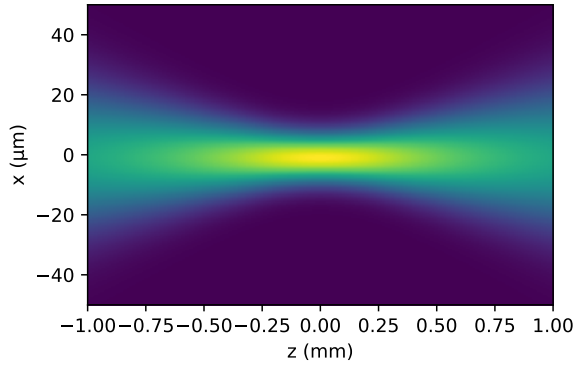

Figure 2.3: A propagation of a Gaussian beam in xz-plane with waist size $w_0 = 10\,\mu$m.

2.2 Surface waves

2.2.1 Surface plasmon polaritons (SPPs)

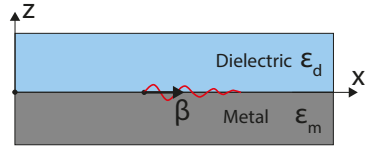

Figure 2.4: The interface of semi-infinite dielectric (permittivity ε_d) and metal (permittivity ε_m) mediums that support SPP mode with propagation constant β.

Surface plasmon polaritons (SPPs) are one of the best known surface waves in the field of optics. They exist only for p-polarization at the boundary of metal and dielectric and are fundamentally caused by the oscillation of free conduction charges at the surface of the metal. In the simplest geometry (see Fig. 2.4a), at the boundary of semi-infinite metal (permittivity $\mathrm{Re}\left[\varepsilon_m\left(\omega\right)\right] < 0$) and dielectric (permittivity $\mathrm{Re}\left[\varepsilon_d\left(\omega\right)\right] > 0$), the dispersion relationship of SPPs could be expressed as

$$\beta = \frac{\omega}{c}\sqrt{\frac{\varepsilon_d\left(\omega\right)\varepsilon_m\left(\omega\right)}{\varepsilon_d\left(\omega\right)+\varepsilon_m\left(\omega\right)}},$$

where $\beta = \mathbf{k}\cdot\hat{\mathbf{x}}$ is the propagation constant. [26, 30, 31]

In order to be a surface wave, the propagation constant must be larger than the magnitude of the wavevector in the dielectric and in the metal, otherwise, the mode will not be bounded to the surface (i.e the mode is not exponentially decaying away from the surface). It also means, that it is not possible to excite SPPs just by shining light to a metal surface, as the propagation constant of SPPs is always larger than the magnitude of the wavevector of light in the dielectric.

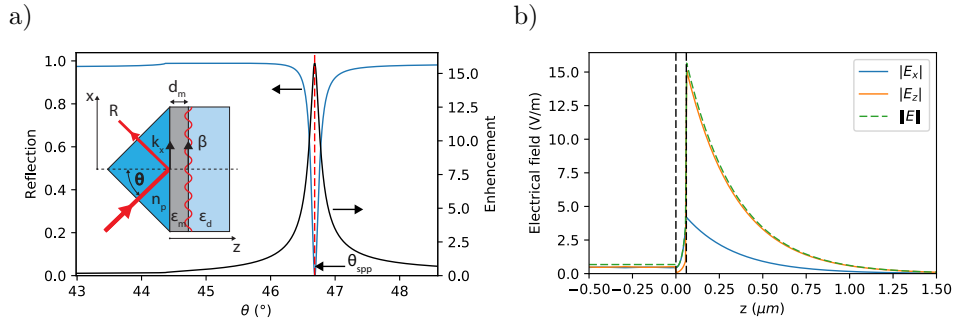

Figure 2.5: a) Reflection and enhancement curves ($\lambda = 802\,\text{nm}$) of the structure in the inset. θ is the angle of incidence, the prism has refractive index $n_p = 2.2$ and the permittivities of the metal ($d_m = 60\,\text{nm}$) and the dielectric are $\varepsilon_m = -31.2 + 0.41i$ and $\varepsilon_d = 2.37$, respectively. b) The electrical field distribution of the structure in the inset of Fig. 2.5a in the case of resonance angle.

To excite SPPs, several different methods have been proposed: excitation with high refractive index coupling prism, with the near fields of fluorescent molecules, with properly designed gratings, with tips of fibers and with electrons [30, 32–36]. Probably the most popular ones are Kretschmann, also used in this work, and Otto configuration [30, 37].

Kretschmann configuration (see the inset of Fig. 2.5a) consists of a high refractive index ($n_p(\omega)$) prism, thin (d_m) metal film (usually gold or silver) and dielectric medium attached to it (can also be air). The structure is illuminated through the high refractive index prism and SPPs are excited at the boundary of the metal and the dielectric. In order to excite SPPs, the tangential wave-vector of the exciting light

$$k_x(\theta) = \frac{\omega}{c} n_p(\omega) \sin\theta$$

must match the propagation constant of SPPs. It is a usual condition for exciting waveguide modes and corresponds to the conservation of the momentum [30]. The angle of incidence of the exciting light, which fulfills the phase-matching condition ($k_x(\theta_{spp}) = \beta$), is called the resonance angle of SPPs. In order to work, Kretschmann configuration requires the metal film to be thin,

as otherwise, the evanescent field of the total internal reflection (TIR) would not penetrate through it. If the metal film is too thin, then the SPPs would be again inefficiently excited due to high leakage losses to the prism. Optimal thickness for silver and gold is in range 40 – 60 nm.

The excitation of SPPs manifests itself as a sharp minimum in a reflection curve (the dependence of the reflection coefficient on the angle of incidence). As an example, the reflection curve is calculated at a wavelength $\lambda = 802\,\text{nm}$ for a prism with refractive index $n_p = 2.2$, a thin silver film ($d_m = 60\,\text{nm}$ and $\varepsilon_m = -31.2 + 0.41i$ from Ref. [38]) and a single crystal alpha quartz ($n_d = 1.538$ from Ref. [39]). The reflection drops to almost zero at angle $\theta_{spp} \approx 45.69°$ and corresponds to the case where almost all of the energy is transferred to SPPs. The field distribution at the resonance condition is shown in Fig. 2.5b. The surface wave at the boundary of silver and quartz is clearly visible: the fields have a maximum at the interface and decay exponentially to both mediums. As SPPs are p-polarized, only x- and z-components of the electrical fields are non-zero. The strongest field component is perpendicular to the interface (E_z).

From Fig. 2.5b it is also visible, that the fields of the SPPs are also greatly enhanced in comparison to the exciting fields. Indeed, as the incident field amplitude is fixed to 1 V/m (given in vacuum), then the field enhancement, in this case, is over 15 times. Field enhancement is one of the most important properties of resonant waves and has motivated many scientific studies and applications. Also this thesis relies on the field enhancement properties of SPPs and the other resonant modes. Two main physical mechanisms are responsible for the enhanced fields of SPPs. Firstly, the SPP mode is highly confined near the metal film leading to the field enhancement through the focusing effect. Secondly, the SPP mode is basically a resonant cavity with a good quality factor that piles up energy in time, leading to the enhanced electrical fields.

The topic of plasmonics has been very popular in the recent decades and many interesting applications have been proposed. One of the main applications, already commercialized by several companies, is surface plasmon resonance sensor for real-time observation of biomolecular interactions [40, 41]. It is based on the refractive index changes due to the biomolecular interactions near a metal film, which results in shifting of the resonance angle of SPPs. Another interesting field of plasmonics utilizes the tight confinement beyond the diffraction limit of the SPP mode to guide the light in subwavelength waveguides in order to miniaturize photonic circuits [42, 43]. A typical example of a benefiting application is interconnects between a central processing unit and a memory to increase the bandwidth and to access the true potential of silicon transistors [44]. Another very interesting field has emerged from a coupling of SPPs and emitters, inducing substantial changes in the emission properties like surface plasmon-coupled emission and strong coupling [34, 45, 46].

The field of nonlinear plasmonics is closely related to the topic of this

thesis [47]. Probably the first work in this field is by H. J. Simon, et. al. where they report first theoretical and experimental investigation of the second-harmonic generation with SPPs in silver films [48]. They report enhancement of SHG of one and a half orders of magnitude due to the excitation of SPPs at the silver-air interface, where the only source of the second-order susceptibility is the interface causing the symmetry breaking. The SPP-enhanced SHG from the interface of silver and nonlinear crystal (alpha quartz) was experimentally observed a few years later [49]. Since the first publication of SPP-enhanced SHG the field of nonlinear plasmonics has attracted significant scientific interest and many other nonlinear processes (difference-frequency generation, third-harmonic generation, four-wave mixing, etc.) have been studied in different geometries supporting SPPs [47]. Only recently, the role of plasmonic and photonic modes in the enhancement of SHG was studied by momentum-space spectroscopy [24].

2.2.2 Long-range surface plasmon polaritons (LRSPPs)

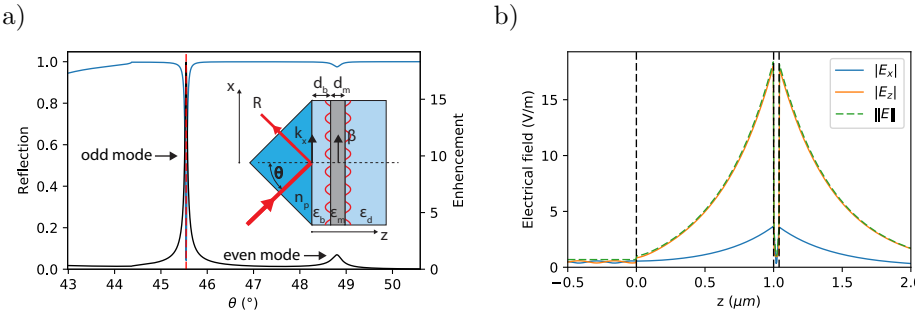

Figure 2.6: a) Reflection and enhancement curves ($\lambda = 802\,\text{nm}$) of the structure in the inset. θ is the angle of incidence, the prism has refractive index $n_p = 2.2$ and the permittivities of the buffer layer ($d_b = 1\,\mu\text{m}$), metal ($d_m = 40\,\text{nm}$) and dielectric are $\varepsilon_b = \varepsilon_d$, $\varepsilon_m = -31.2 + 0.41i$ and $\varepsilon_d = 2.37$, respectively. b) The electrical field distribution of the structure in the inset of Fig. 2.6a in the case of resonance angle.

Another type of surface waves is possible in a three-layer structure consisting of dielectric (buffer), thin metal (thickness d_m) and dielectric (substrate) layers (inset of Fig. 2.6a without a prism) – long-range surface plasmon polaritons (LRSPPs). LRSPPs were first predicted by D. Sarid in 1981 (Ref. [50]) and experimentally detected in 1983 by J. C. Quail, et. al (Ref. [51]). LRSPPs are composed of two usual SPP modes excited on both metal-dielectric interfaces. If the metal layer is thin, then modes on each interface become coupled. The dispersion relationship could only be expressed implicitly

$$e^{-4\beta d_m} = \frac{\beta/\varepsilon_m + k_{z,b}/\varepsilon_b}{\beta/\varepsilon_m - k_{z,b}/\varepsilon_b} \cdot \frac{\beta/\varepsilon_m + k_{z,d}/\varepsilon_d}{\beta/\varepsilon_m - k_{z,d}/\varepsilon_d}, \tag{2.53}$$

where β is the propagation constant, $k_{z,b}$ and $k_{z,d}$ are the z-components of the wavevectors in the buffer and dielectric layer, respectively [31, 50, 52, 53].

Due to the coupling of the two SPPs, new modes arise: odd and even mode. In the case of odd mode, electrical fields of SPPs on each interface interfere destructively in the metal film and as a result the electrical fields in the metal decay very fast. Consequently, such kind of modes display very low losses and propagate further than usual SPPs (up to several millimeters) – it is also the reason for the naming of LRSPPs. The other, even mode, is usually ignored, as it has inferior properties: the propagation length is shorter and the field enhancement is lower. Moreover, LRSPPs are mainly studied/used in symmetric structures, where the refractive index of the buffer and the substrate layers are the same because it provides longest propagation distances [54].

To excite LRSPPs, similar schemes as in the case of usual SPPs must be employed. As an example, LRSPPs are studied in Kretschmann configuration (inset of Fig. 2.6a). Again, a reflection curve is calculated at a wavelength $\lambda = 802\,\text{nm}$ for a prism with refractive index $n_p = 2.2$, buffer layer ($d_b = 1\,\mu\text{m}$ and $n_b = 1.538$), a thin silver film ($d_m = 40\,\text{nm}$ and $\varepsilon_m = -31.2 + 0.41i$ [38]) and a single crystal alpha quartz ($n_d = 1.538$). Two minima are visible in Fig. 2.6 corresponding to the odd and to the even mode. The field distribution of the odd mode is shown in Fig. 2.6b. Indeed, the fields are mainly located outside of the metal.

The thicknesses of buffer and metal layer selected for the example are not optimal for a maximum propagation distance nor for a maximum field enhancement. The general dependency is, that thinner metal layer with appropriately thicker buffer layer provides better performance and also narrower resonances. As resonances can become very narrow, it becomes essential to take also into account the limitations arising from realistic laser beams (see Sec. 2.1.4).

Applications of LRSPPs, in general, are similar to the applications of ordinary SPPs: sensing, the enhancement of light interaction with matter, wave-guiding, nonlinear interactions, etc [53, 55–57].

2.2.3 Guided dielectric waves (GDWs)

Both, SPPs and LRSPPs, require metal layer in the structure. As real metals are always lossy, then also the excitation and the propagation of these modes are inherently accommodated with losses – often the main limiting factor of possible applications [58]. For that reason, the scientific focus has again started to shift towards all-dielectric structures [59–63]. One possible all-dielectric

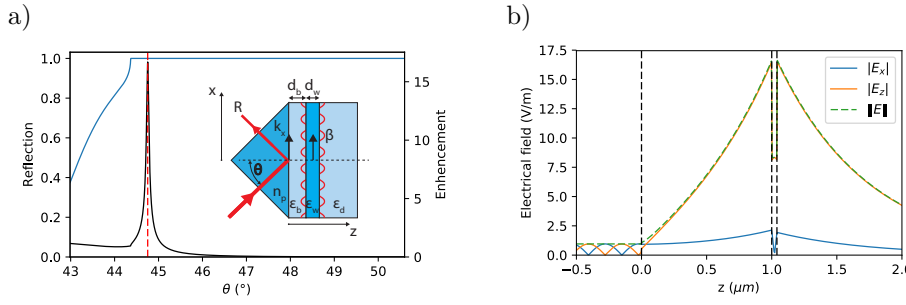

Figure 2.7: a) Reflection and enhancement curves ($\lambda = 802\,\text{nm}$) of the structure in the inset. θ is the angle of incidence, the prism has refractive index $n_p = 2.2$ and the permittivities of the buffer layer ($d_b = 1\,\mu\text{m}$), waveguide ($d_w = 40\,\text{nm}$) and dielectric are $\varepsilon_b = \varepsilon_d$, $\varepsilon_w = 4.84$ and $\varepsilon_d = 2.37$, respectively. b) The electrical field distribution of the structure in the inset of Fig. 2.7a in the case of resonance angle.

structure supporting resonant modes is identical to the structure supporting LRSPPs, except the metal layer is replaced with a waveguiding layer with high refractive index [59, 64]. In this work, we name resonant modes supported by such structure to guided dielectric waves (GDWs). GDWs are in general very similar to LRSPPs. The dispersion relationship for p-polarized GDWs are also given by Eq. 2.53, however, also s-polarized GDWs are supported by the structure.

The resonances of GDWs can also become very narrow and the general dependency to have higher field enhancements is to have a very thin waveguide layer and an appropriately thick buffer layer. The excitation of p-polarized GDWs is shown in Fig. 2.7a, where all the parameters are the same as in the case of LRSPPs, except the metal film is replaced with waveguide layer with refractive index $n_w = 2.2$. Now the resonances are only visible by enhancement factor, as the structure contains no lossy materials and all of the light has to be reflected. In some cases, it is computationally convenient to add very small losses to the materials to make the resonances visible. Also, the field distribution is very similar to LRSPPs (see Fig. 2.7b) – fields are enhanced near the waveguiding layer.

In Ref. [59] it is claimed, that the structure in the inset of Fig. 2.7a could produce arbitrarily large optical field enhancements only limited by the fabrication tolerances of the structure. In Sec. 4.3.3 we show, that it is only so in the limit of infinite plane wave approximation – in the case of realistic light beams, the maximum enhancement is greatly limited by the narrow resonances of GDWs.

2.2.4 Dyakonov SPPs (DSPPs)

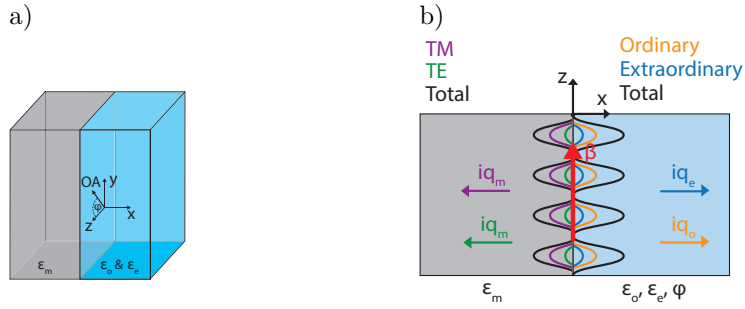

Figure 2.8: a) A interface of a metal (permittivity ε_m) and an uniaxial anisotropic crystal with ordinary and extraordinary permittivities ε_o, ε_e, respectively. The OA of the uniaxial anisotropic crystal is taken to be in yz-plane and the angle between the z-axis and the OA is denoted by φ. b) The cross-section of the structure in Fig. 2.8a. The propagation constant of DSPP mode is denoted by β and the four components are marked by different colors. [V]

More exotic types of surface waves exist at the boundary of isotropic and anisotropic mediums. Such kind of surface waves was first theoretically predicted by Dyakonov in 1988 [65]. As requirements for the appearance of Dyakonov waves are demanding, the experimental observation was accomplished only recently at the interface of KTP crystal and index-matching liquid [66]. A good review of Dyakonov waves is given in Ref. [67] and several applications have been proposed in the field of optical switching [68], wave-guiding [69] and sub-diffraction imaging [70].

Another variation of Dyakonov waves, Dyakonov SPPs (DSPPs), was found to exist at the interface of a metal and an anisotropic crystal [67, 71, 72]. Here a short overview of DSPPs will be given to introduce the background for the chapter 5 of the thesis. The structure under the interest is shown in Fig. 2.8a. The dielectric permittivity of the metal half-space ($x < 0$) is ε_m and the uniaxial anisotropic crystal is described by ordinary ε_o and extraordinary ε_e dielectric permittivities. The OA of the anisotropic crystal is fixed to lie in the yz-plane and the angle between the OA and the z-axis is denoted by φ. Note the different orientation of the xyz-axes in comparison to previous sections: the orientation of axes are different in this section and in chapter 5 in order to match the notation used in Ref. [V].

DSPPs, like usual Dyakonov waves, are hybridized – the surface wave has no single polarization. DSPPs are described by a superposition of TM- and TE-polarization in the metal and by an ordinary and extraordinary mode in the anisotropic medium. In other words, a DSPP mode consists of four evanescent

waves: two in the metal and the other two in the anisotropic medium (see Fig. 2.8b).

Wavevectors of the two evanescent waves in the metal are the same

$$\mathbf{k}_m = -iq_m\hat{\mathbf{x}} + \beta\hat{\mathbf{y}}, \tag{2.54}$$

where β is the propagation constant of DSPPs (continuous at the interface) and q_m is the decay constant into the metal defined by

$$q_m = \sqrt{\beta^2 - \varepsilon_m}. \tag{2.55}$$

Note, that in this section, all wavevectors are scaled by the vacuum wave number ω/c as it is in Ref. [V] and also in the original derivation by Dyakonov [65]. Similarly, wavevectors of the ordinary and extraordinary evanescent waves are

$$\mathbf{k}_o = iq_o\hat{\mathbf{x}} + \beta\hat{\mathbf{y}}, \tag{2.56}$$
$$\mathbf{k}_e = iq_e\hat{\mathbf{x}} + \beta\hat{\mathbf{y}}, \tag{2.57}$$

where the decay constants are

$$q_o = \sqrt{\beta^2 - \varepsilon_o}, \tag{2.58}$$
$$q_e = \sqrt{\beta^2\left(1 + \eta\cos^2\varphi - \varepsilon_e\right)}. \tag{2.59}$$

The parameter η denotes the degree of anisotropy defined by Eq. 2.24.

Requiring the continuity of the tangential components of electric and magnetic fields yields the dispersion relationship originally derived by Dyakonov (Ref. [65])

$$\left(q_m + q_e\right)\left(q_e + q_o\right)\left(\varepsilon_m q_o + \varepsilon_o q_e\right) = \left(\varepsilon_e - \varepsilon_m\right)\left(\varepsilon_m - \varepsilon_o\right)q_o. \tag{2.60}$$

This dispersion relationship was first studied in 2008 in the context of DSPPs and necessary conditions and regimes for the existence of DSPPs (named to hybridized SPPs) were presented [71]. It has been shown, that in the case of a positive crystal ($\varepsilon_e > \varepsilon_o$), the necessary condition for the existence of DSPPs is

$$\eta > \frac{\varepsilon_e}{|\varepsilon_m|}. \tag{2.61}$$

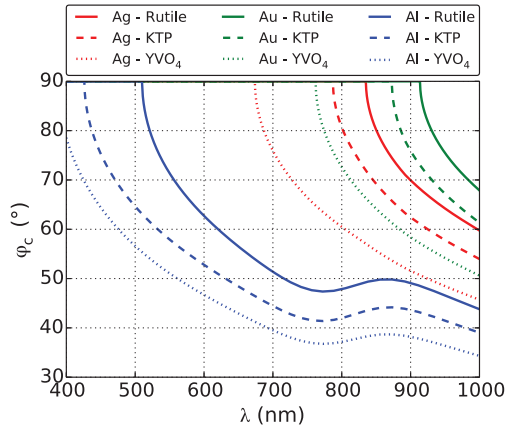

Figure 2.9: The dependence of the critical angle (φ_c) of DSPPs on the wavelength and on the different choices of materials. [V]

In the case of silver ($\lambda = 900\,\mathrm{nm}$), the condition given by Eq. 2.61 is fulfilled for a number of well-known anisotropic crystals: TiO_2 (Rutile), YVO_4 and KTP (almost uniaxial crystal with positive birefringence) [38, 73–75]. Moreover, DSPPs only exists for specific orientations $\varphi < \varphi_c$ of the OA of the crystal – the DSPPs disappear if the extraordinary decay constant becomes zero ($q_e = 0$). The critical angle is approximated by

$$\varphi_c \backsimeq \operatorname{asin} \sqrt{\frac{\varepsilon_e^2 \left(\varepsilon_o + |\varepsilon_m|\right)}{\left(\varepsilon_o \left(\varepsilon_e + |\varepsilon_m|\right)^2 + \varepsilon_e^2 |\varepsilon_m|\right) \left(\varepsilon_e - \varepsilon_o\right)}} \tag{2.62}$$

if $-\operatorname{Re}[\varepsilon_m] \gg \varepsilon_e, \varepsilon_o, \operatorname{Im}[\varepsilon_m]$ like in the case of usual metals [V]. The wavelength dependence of the critical angle for the combination of metals and anisotropic crystals is shown in Fig. 2.9 [V]. In the case of silver and gold, the critical angle exists only in the red part of the spectrum – the DSPPs exists for all the orientations of OA for the blue part of the spectrum. On the other hand, in the case of aluminum, the orientation of the OA is more important, as the critical angle exists over the entire visible spectrum.

To excite DSPPs, similar excitation schemes must be used as in the case of other surface waves. As an example, the excitation of DSPPs in Kretschmann configuration is shown in Fig. 2.10 at wavelength $\lambda = 802\,\mathrm{nm}$. The structure consists (the inset of Fig. 2.10a) of high refractive index prism ($n_p = 2.5$), thin silver film ($d_m = 60\,\mathrm{nm}$, $\varepsilon_m = -31.2 + 0.41i$) and KTP crystal ($\varepsilon_o = 3.06$, $\varepsilon_e = 3.40$ and $\varphi = 40°$). Results are very similar to usual SPPs, the p-polarized reflection (Fig. 2.10a) displays a minimum, that is accompanied by field enhancement. Also, the field distribution in Fig. 2.10b is very similar to the usual SPPs, however, a small hybridization effect is also visible: every field component is present in the crystal.

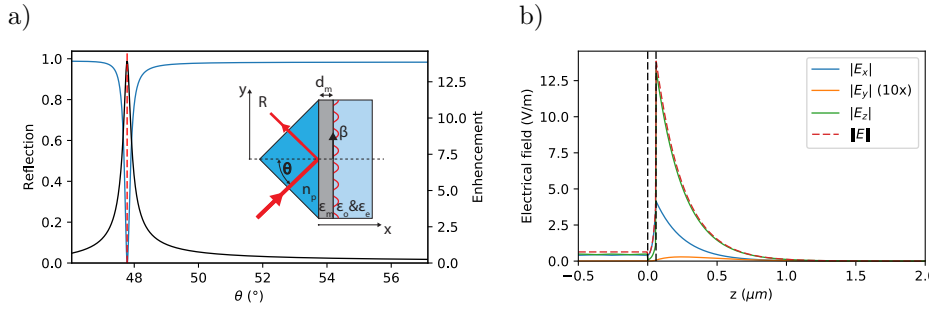

Figure 2.10: a) Reflection and enhancement curves ($\lambda = 802\,\text{nm}$) of the structure in the inset. θ is the angle of incidence, the prism has refractive index $n_p = 2.5$ and the permittivities of the silver layer ($d_m = 60\,\text{nm}$), ordinary and extraordinary waves of the crystal are $\varepsilon_m = -31.2 + 0.41i$, $\varepsilon_o = 3.06$, $\varepsilon_e = 3.40$, respectively. The orientation of the OA is taken to be $\varphi = 40°$. b) The electrical field distribution of the structure in the inset of Fig. 2.10a in the case of resonance angle.

The background presented in this section will be used in chapter 5, where the properties of DSPPs are studied further to propose a new excitation scheme for surface waves.

2.3 Spontaneous parametric down-conversion (SPDC)

2.3.1 Introduction

Spontaneous parametric down-conversion (SPDC) was first experimentally observed in 1967 by S. E. Harris, et. al. [76] and theoretically investigated by D. N. Klyshko [77–79]. A little later, in 1970, first quantum properties of the light generated by SPDC were experimentally shown by D. C. Burnham and D. L. Weinberg. They showed that the signal and idler photons appeared simultaneously, in pairs, within the capabilities of the measurement setup [80]. Since then, SPDC has received a considerable interest due to the possible interesting quantum properties of photon pairs – quantum entanglement. Probably the most significant are the Bell's inequality experiments to rule out the hypothesis of a local hidden variable in quantum mechanics [1, 2, 81].

Usual setup for SPDC is shown in Fig. 2.11. The pump laser (frequency ω_p) is incident on the nonlinear crystal with non-zero second-order susceptibility tensor $\chi^{(2)}$ and due to the nonlinear interaction a small fraction of the pump photons split to two: idler (ω_i) and signal ($\omega_s = \omega_p - \omega_i$) photons (historical naming convention) [82, 83]. In classical nonlinear optics, such process is not possible as nonlinear polarization for generating signal photons requires

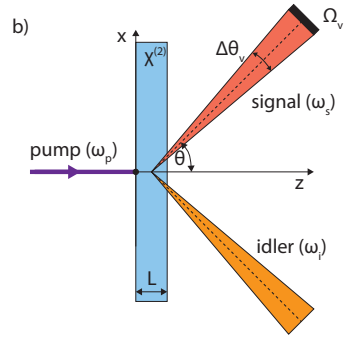

Figure 2.11: Typical setup for SPDC. The pump laser (frequency ω_p) is incident on the nonlinear crystal with second-order susceptibility $\chi^{(2)}$ and thickness L. Due to nonlinear interaction, the pump photons splits into a signal (ω_s) and idler beams (ω_i). The signal beam is detected with the sensor (solid angle Ω_v and angular span θ_v) under the angle of incidence θ. [IV]

two fields to be present (Eq. 2.31): a pump field and another field at the idler frequency [29].

Here, however, this nonlinear process takes place only by a participation of a single pump wave. Evidently, SPDC is a process that could only be explained by quantum optics. Moreover, SPDC is a direct consequence of quantum optical vacuum fluctuations (zero photon state $|0\rangle$). Instead of having second field present, required by classical optics, it is replaced by vacuum fluctuations. The process of SPDC is described as

$$|N\rangle_p |0\rangle_s |0\rangle_i \overset{\chi^{(2)}}{\rightarrow} |N-1\rangle_p |1\rangle_s |1\rangle_i , \tag{2.63}$$

where initially there are N photons in the pump mode and zero photons in both signal and idler mode. Due to the interaction with the nonlinear medium, the state evolves into $|N-1\rangle_p |1\rangle_s |1\rangle_i$. It corresponds to the splitting of a single pump photon into signal and idler modes.

2.3.2 Phase matching

For an efficient generation of photon pairs in SPDC, the conservation of energy and momentum must be fulfilled, like in the case of classical nonlinear processes,

$$\hbar\omega_p = \hbar\omega_s + \hbar\omega_i, \tag{2.64}$$
$$\mathbf{k}_p = \mathbf{k}_s + \mathbf{k}_i, \tag{2.65}$$

where $\mathbf{k}_p$, $\mathbf{k}_s$ and $\mathbf{k}_i$ represent the wavevectors (momentums) of the corresponding photons. In an isotropic medium with normal dispersion, it is not possible to simultaneously fulfill the conditions given by Eqs. 2.64 and 2.65. As a workaround, birefringent crystals are used, where orthogonal polarizations display different refractive index dispersions. With a careful orientation of a anisotropic crystal, phase-matching conditions could be met. Most common nonlinear and birefringent crystals for SPDC experiments are $Ba(BO_2)_2$ (BBO) and KH_2PO_4 (KDP).

In usual SPDC experiment, the splitting of pump photons happens not only equally ($\omega_s = \omega_s = \omega_p/2$), but into a wide range of frequencies. The spiting ratio (ω_s/ω_i) and the spectral width of the idler and the signal beam depend on the refractive index dispersion of the birefringent crystal and on the positioning of the crystal.

2.3.3 Quantum theory of SPDC

The quantum theory of SPDC has been developed by many authors [77, 79, 84–86]. Here a short overview of the quantum theory mainly based on Ref. [84] will be given. The formulations are generalized and converted into SI units. According to this theory, the rate of the transition equals to

$$\Gamma = \frac{2\pi}{\hbar^2}\delta\left(\omega_p - \omega_s - \omega_i\right)\left|\langle N,0,0|\, H'\, |\mathbf{k}_i, \mathbf{k}_s, N-1\rangle\right|^2, \tag{2.66}$$

where $\delta(\omega)$ is the Dirac delta function, $\langle N,0,0|$ is the initial state with N photons in the pump laser mode and no photons in the signal and idler mode, $|\mathbf{k}_i, \mathbf{k}_s, N-1\rangle$ is one of the final states with a single photon both in the signal mode (denoted by $\mathbf{k}_s$) and in the idler mode (denoted by $\mathbf{k}_i$). We assume that only signal photons are detected in the experiment. The nonlinear interaction Hamiltonian is given by

$$H' = \int_V d\mathbf{r} \int_0^{\mathbf{E}_t} \mathbf{P}_{NL} \cdot d\mathbf{E}_t, \tag{2.67}$$

where V is volume and $\mathbf{E}_t$ represents the sum of all fields [84].

To obtain the power of the generated SPDC signal, we must integrate over certain values of $\mathbf{k}_s$ which fall into a wavelength band $\Delta\lambda$ and into a solid angle window Ω_v (given in vacuum) detectable by a sensor. As vacuum fluctuations are present in every idler mode $\mathbf{k}_i$, the signal is also generated into a wide range of modes $\mathbf{k}_s = \mathbf{k}_p - \mathbf{k}_i$. The power of the SPDC signal detectable by a sensor (in xz-plane) from a specific direction (determined by θ in Fig. 2.11) is

$$P_s = \Delta\lambda \frac{\Omega_v}{\Delta\theta_v} \frac{\hbar\chi^2}{8\pi^4\varepsilon_0} \frac{\omega_s^6 \omega_p \omega_i^2}{c^8} P_p \times \\ \times \int_{\bar{k}_{xi}-\Delta k_{xi}}^{\bar{k}_{xi}+\Delta k_{xi}} dk_{x2} \frac{L^2}{k_{zs} k_{zp} k_i} \mathrm{sinc}\left(\frac{\Delta k L}{2}\right)^2, \tag{2.68}$$

where $\Delta\theta_v$ denotes the angular span of the detector (in vacuum) in xz-plane (see Fig. 2.11), P_p is the power of the pump beam, L is the length of the nonlinear crystal, Δk is the phase mismatch, ε_0 is vacuum permittivity and k_{xi}, k_{zp}, k_{zs} are the components of the corresponding wavevectors to specific directions.

Eq. 2.68 contains integration over a specific range of wavevectors of modes representing vacuum fluctuations (k_{xi}). Originally this integral was over a specific range of generated SPDC modes falling onto the sensor in the wavelength band $\Delta\lambda$ and over all idler modes. However, it was more convenient to integrate over the specific range of idler modes (integral over k_{xi}). In other words, only the specific range ($\bar{k}_{xi} - \Delta k_{xi} ... \bar{k}_{xi} + \Delta k_{xi}$) of vacuum fluctuation modes will participate in the generation of SPDC for a fixed position of the sensor. Limits of the integration are given by

$$\bar{k}_{xi} = k_{xp} - \frac{\omega}{c} n_0 \sin(\theta) \tag{2.69}$$

$$\Delta k_{xi} = \frac{\sqrt{\omega^2 n_0^2/c^2 - \left(k_{xp} - \bar{k}_{xi}\right)^2}}{2n_0} \Delta\theta_v, \tag{2.70}$$

where θ determines the position of the sensor, k_{xp} follows from the angle of the incidence of the pump laser and n_0 is the refractive index of out-coupling medium (see Fig. 2.11b).

From Eq. 2.68 it is clear, that SPDC is linear with respect to the power of the pump wave. It means, that in the case of SPDC the focusing of the pump beam has no effect on the efficiency of the process.

3 SPP-enhanced SPDC (publication I, II)

3.1 Introduction

This chapter begins with a theoretical introduction to SPP-enhanced SPDC. Firstly, one of the possible structures supporting SPP-enhanced SPDC is introduced and the enhancement factors of SPDC are estimated from the plasmonic field enhancement factors. Next, phase-matching conditions are reviewed and different processes for SPP-enhanced SPDC are listed. Note, that the full modeling of SPP-enhanced SPDC is postponed until chapter 4.

In the second part of this chapter, the experimental work towards the realization of SPP-enhanced SPDC is reviewed. Firstly, the experimental details of the fabrication of the structure supporting SPP-enhanced SPDC are given. Secondly, the custom-made experimental setup is described and the experimental methods are outlined. Finally, the results of the experimental work are presented.

3.2 Theory

In a usual SPDC (see Fig. 3.1a) a small fraction of pump photons split directly to signal and idler photons due to nonlinear interaction with matter. The idea behind SPP-enhanced SPDC is to split pump photons into signal and idler plasmons instead of photons [I]. It is possible in a structure similar to Kretschmann configuration (see Fig. 3.1b), which consists of (from left to right) a high refractive index prism, thin metal film and nonlinear crystal. Under the specific angle of incidence of the pump beam (phase-matching condition), it is possible that pump photons split to signal and idler plasmons instead of photons. As plasmonic modes have enhanced electrical fields and as SPDC is a nonlinear process, it is evident that also the conversion efficiency of the pairs of plasmons is enhanced. After short propagation, the signal and idler plasmons will leak back to the prism as photons.

3.2.1 Enhancements

From the quantum theory of SPDC, it is known that the interaction Hamiltonian (Eq. 2.67) of SPDC is linearly proportional to each of the participating electrical fields (pump, signal, idler). If the pump, signal and idler fields are

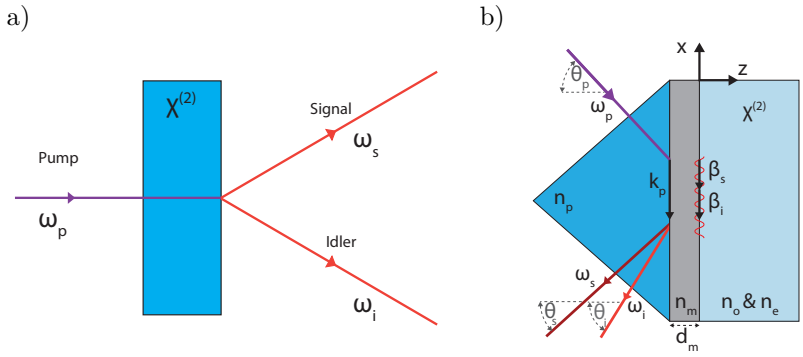

Figure 3.1: a) The typical setup of SPDC where pump photons (ω_p) split to signal (ω_s) and idler (ω_i) photons due to second-order susceptibility ($\chi^{(2)}$) of the crystal. b) The setup of SPP-enhanced SPDC. The structure consists of a high refractive index prism, thin metal film (thickness d_m) and nonlinear crystal. The pump beam is incident through the prism and in the case of perfect phase-matching ($k_p = \beta_s + \beta_i$) splits into two plasmons (propagation constants β_s and β_i) instead of photons. The signal and idler plasmons sequentially outcouple back to the prism as photons. [I]

correspondingly enhanced by factors η_p, η_s, η_i, then also the rate of the SPDC signal (Eq. 2.66) will be enhanced by a factor

$$\Upsilon\left(\omega_p, \omega_s, \omega_i\right) = \left(\eta_p\left(\omega_p\right)\eta_s\left(\omega_s\right)\eta_i\left(\omega_i\right)\right)^2 . \tag{3.1}$$

Alternatively, in terms of classical nonlinear optics, if the pump, signal and idler fields are enhanced, then the nonlinear polarization for the generation of signal would be enhanced by a factor $\eta_p\eta_i$. As also the field of the generated signal is enhanced by factor η_s, then the total field enhancement is $\eta_p\eta_s\eta_i$. The corresponding power flow (rate of generated photons) is proportional to the square of the electrical field amplitude and again the total enhancement factor of SPDC would be given by Eq. 3.1.

Available enhancement factors were studied by us in Ref. [I] for the structure (see Fig. 3.1b) consisting of Rutile prism (refractive index $n_p = 2.5$), thin silver film and BBO crystal (refractive indices from Refs. [38, 87]) by TMM calculations. The enhancement factor dependence of the signal and idler plasmons (identical) on the wavelength and metal film thickness is shown in Fig. 3.2a. Enhancement factors up to ≈ 25 are available in the NIR region of spectrum for $d_m = 60\,\text{nm}$ thick silver film.

The dependence of the enhancement factor of SPP-enhanced SPDC (Eq. 3.1) on the pump wavelength is shown in Fig. 3.2b (assuming equal splitting $\omega_s = \omega_i = \omega_p/2$). The maximum enhancement factor of SPDC is up to $\Upsilon = 40 \cdot 10^3$ times for p-polarized pump laser at wavelength $\lambda_p = 540\,\text{nm}$.

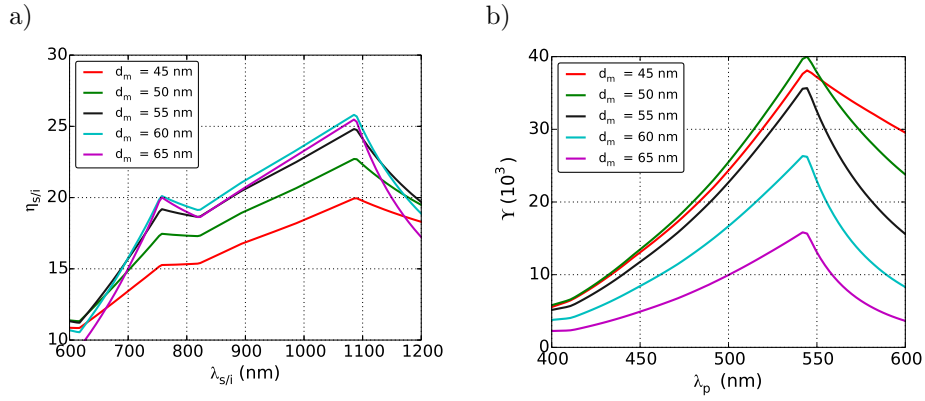

Figure 3.2: a) The enhancement factor ($\eta_{s/i}$) of the signal and idler plasmons (identical) dependence on the wavelength ($\lambda_{s/i}$) and metal film thickness (d_m). b) The enhancement factor of SPP-enhanced SPDC (Eq. 3.1) dependence on the pump wavelength (assuming equal splitting $\omega_s = \omega_i = \omega_p/2$). [I].

Such enhancement could enhance the yield of SPDC from 10^{-12} up to 10^{-8}. The optimal thickness of the silver film is reduced to $d_m = 50\,\text{nm}$ because of the pump enhancement factor $\eta_p \approx 0.5$, which is less than one (attenuation instead of enhancement) because the pump light has to penetrate through the silver film.

3.2.2 Phase-matching conditions

Another important factor for the efficient generation of SPDC is fulfilling phase-matching conditions (Eqs. 2.64 and 2.65). In the case of SPP-enhanced SPDC, phase-matching conditions are given by

$$\omega_p = \omega_s + \omega_i, \tag{3.2}$$
$$k_p(\omega_p, \theta_p) = \beta_s(\omega_s) + \beta_i(\omega_i), \tag{3.3}$$

where $k_p = \omega_p n_p(\omega_p)\sin(\theta_p)/c$ is the tangential component of the pump wavevector, θ_p is the angle of incidence of the pump beam inside the prism, β_s and β_i are the propagation constants of the signal and idler SPP modes, respectively [I]. To illustrate the possibility for the phase-matched generation of the SPP-enhanced SPDC, both sides of Eq. 3.3 are plotted in Fig. 3.3 for different splitting ratios. It is evident, that indeed perfect phase-matching is possible by careful tuning of the angle of incidence of the pump beam (denoted by red circles in Fig. 3.3). Moreover, it is possible to select the splitting ratio

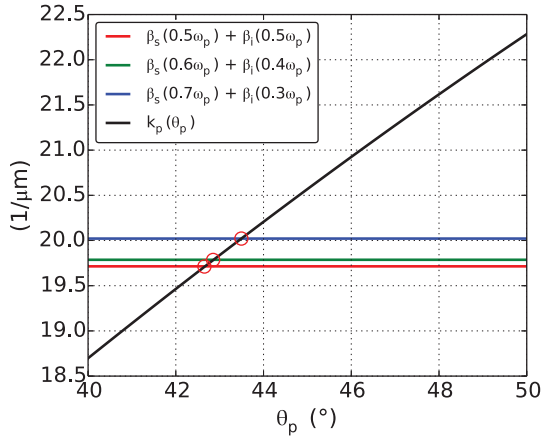

Figure 3.3: The illustration of the possibility of the perfect phase-matching for different splitting ratios by tuning the angle of incidence θ_p. [I]

(ω_s/ω_i) of pump photons by tuning the angle of incidence θ_p of the pump laser.

3.2.3 Processes of SPP-enhanced SPDC

Table 3.1: The list of different processes of SPDC enhancement, where f and p denote photons and plasmons, respectively.

#	Code	Process
1	fff	$f(\omega_p) \rightarrow f(\omega_i) + f(\omega_s)$
2	pff	$p(\omega_p) \rightarrow f(\omega_i) + f(\omega_s)$
3	fpf	$f(\omega_p) \rightarrow p(\omega_i) + f(\omega_s)$
4	ffp	$f(\omega_p) \rightarrow f(\omega_i) + p(\omega_s)$
5	ppf	$p(\omega_p) \rightarrow p(\omega_i) + f(\omega_s)$
6	pfp	$p(\omega_p) \rightarrow f(\omega_i) + p(\omega_s)$
7	**fpp**	$f(\omega_p) \rightarrow p(\omega_i) + p(\omega_s)$
8	ppp	$p(\omega_p) \rightarrow p(\omega_i) + p(\omega_s)$

So far we have only considered a process, where both idler and signal are in a enhanced plasmonic mode. All the other variations of enhanced SPDC are listed in table 3.1, where f and p denote photons and plasmons, respectively.

Process #1 is pure photonic process, where pump photon $f(\omega_p)$ split to two other photons due to photonic mode $f(\omega_i)$. No plasmonic enhancement of such process is possible. In processes #2 to #4, however, the enhancement of

SPDC due to the participating plasmonic mode is possible (Eq. 3.1). For an example, in the process #3, the pump photon $f(\omega_p)$ splits due to the enhanced plasmonic mode $p(\omega_i)$ (idler) and the signal photon $f(\omega_s)$ is generated. Moreover, in processes #5 to #7 two participating fields are in plasmonic modes. Such processes are greatly enhanced according to Eq. 3.1. The most enhanced process is denoted by "ppp", where all participating modes are enhanced: the pump plasmon $p(\omega_p)$ splits to the signal plasmon $p(\omega_s)$ due to vacuum fluctuations in the idler mode $p(\omega_i)$. Note, that the pump plasmon $p(\omega_p)$ is created from the pump photon $f(\omega_p)$.

Usually only one of the processes in table 3.1 happen effectively at the same time due to different phase-matching conditions. In other words, it is possible to select the process of enhanced SPDC by tuning the angle of incidence of the pump beam. An exception is the process "ppp", where all participating fields are in plasmonic modes and consequently no phase matching by the tuning of the angle of incidence is possible. For this reason, processes #5 to #7, where the enhancement by two plasmonic modes are available and phase matching is possible, are most promising.

This work mainly focuses on the process "fpp", where pump photons $f(\omega_p)$ split to signal plasmons $p(\omega_s)$ due to vacuum fluctuations in the other plasmonic mode $p(\omega_i)$.

3.3 Experiment

The goal of this section is to give an overview of the experimental realization of the idea of SPP-enhanced SPDC introduced in Sec. 3.2. For the experimental work, a structure supporting SPP-enhanced SPDC was fabricated and custom-made goniometric measurement system was designed and built. To the best of our knowledge, it is the first experimental work towards SPP-enhanced SPDC.

3.3.1 Structure

The structure used for the experimental realization of the SPP-enhanced SPDC is shown in Fig. 3.4. It consists of X-cut single crystal quartz (SiO_2) with the main second-order susceptibility component $\chi_{xxx} = 0.6\,\mathrm{pm/V}$ and was selected due to relatively small refractive index [39]. Next, approximately 50 nm thick silver film was deposited on the quartz crystal and it was subsequently covered by approximately 10 nm thick aluminium oxide layer. The deposition was done by AJA International ultra-high vacuum magnetron sputtering system at room temperature. The Al_2O_3-Ag-SiO_2 structure was attached to the high refractive index N-SF11 right angle prism (Endmund Optics, @47-276, side length 15 mm) by index-matching liquid (IML) from Cargille (Series M, refractive index 1.77).

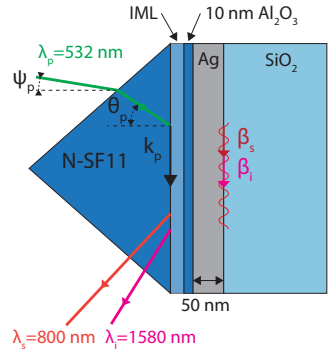

Figure 3.4: The structure used for the experimental realization of the SPP-enhanced SPDC: N-SF11 right angle prism, index-matching liquid (IML), 10 nm thick aluminium oxide layer, 50 nm thick silver film and nonlinear X-cut single crystal quartz (from left to right). The structure is illuminated by a green laser ($\lambda_p = 532$ nm) under the angle of incidence Ψ_p outside and θ_p inside the prism. The generated signal and idler plasmons are denoted by β_s and β_i, respectively. After short propagation, signal and idler plasmons outcouple to the prism as photons (wavelengths λ_s and λ_i, respectively). [II]

3.3.2 Methods

3.3.2.1 Goniometric setup

To measure the structure in Fig. 3.4, a custom-made two-axis goniometric setup in Fig. 3.5 was built (details in Ref. [II]). It consists of four lasers (see Fig. 3.5b): violet 402 nm, green 532 nm and two NIR lasers 802 nm and 1064 nm. All lasers were collimated and spectrally filtered (if necessary) and then aligned by two mirrors to be parallel to the surface of the optical table and to coincide the axis of the goniometer O. To ease the alignment process, two pinholes, PH1 and PH2, were installed. The mirrors FM1 to FM4 are flip mounted for easy switching between the lasers. To control the polarization of the lasers, the half-wave plate H1 was used for the violet laser and the Fresnel rhomb FR1 for other wavelengths. A small fraction of light was reflected to the photodiode D1 by the quartz beamsplitter BS1 for monitoring the laser power during measurements. Finally, the laser light was cleaned by additional filters in the position F2.

The goniometer consists of two motorized rotational stages mounted on top of each other (see Fig. 3.5c) and are controlled from a computer by a two-axis stepper motor controller.

On the detection side, different filters F3, analyzers A1 and detectors D2 were used and will be specified shortly.

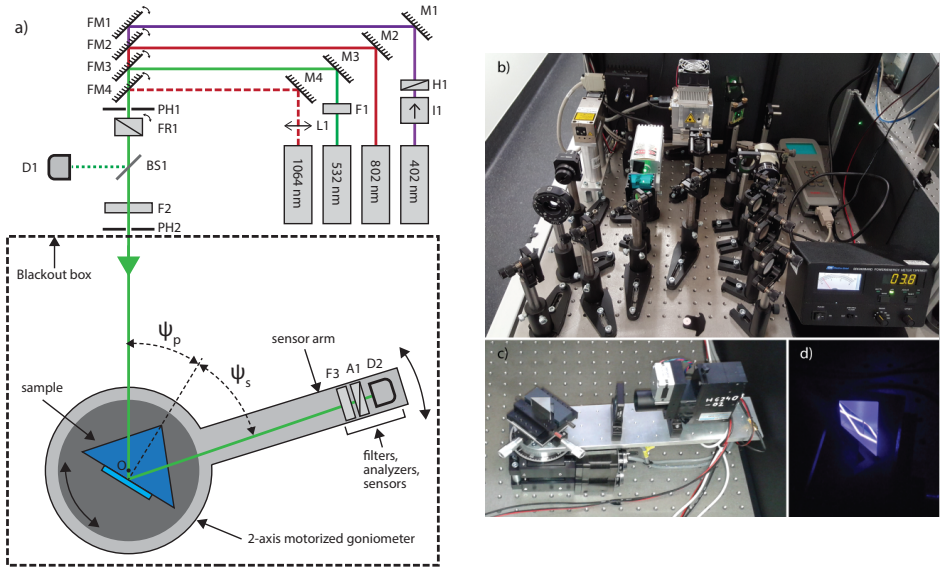

Figure 3.5: The schematic of the goniometric setup (a) and the pictures of the lasers (b), goniometer with lock-in detection system (c) and N-SF11 prism under illumination of violet laser. [II]

3.3.2.2 Lock-in detection

The signal of SPDC is in general weak and sensitive detection system is required. In this work, Hamamatsu H6240-02 photomultiplier tube (PMT) was used. Two main sources of noise limit the minimum detectable signal. Firstly, as the PMT was not cooled, dark counts around $400\,\mathrm{s}^{-1}$ were present due to thermionic emission. Secondly, although the goniometric setup is entirely inside the blackout box, still considerable amount of background signal was generated by the interaction of laser with the structure (e.g. the prism). Moreover, the shot noise from the photon counting fundamentally limits the achievable signal-to-noise ratio.

To suppress the background noise, lock-in amplification was employed. The idea is to modulate the detectable signal at a known frequency and to detect only the signal that is modulated at the same frequency – discarding all noise at other frequencies. The modulation of the signal is usually achieved by modulating the laser intensity, however, in this case, the modulation by rotating analyzer was preferred. As the SPP-enhanced SPDC signal must be p-polarized and the background noise is unpolarized, then rotating the analyzer with frequency f_r in front of the PMT modulates the detected signal $\Gamma(t)$ by Malus's Law

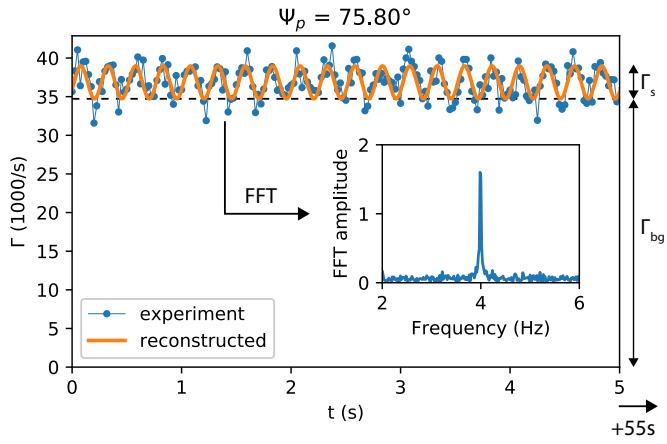

Figure 3.6: An example of measured time series for lock-in detection along with reconstructed signal. The Fourier spectrum of the time series is in the inset. [II]

$$\Gamma(t) = \Gamma_{bg} + \Gamma_s \cos^2(2\pi f_r t) = \left(\Gamma_{bg} + \frac{1}{2}\Gamma_s\right) + \frac{1}{2}\Gamma_s \cos(2\pi f_m t), \qquad (3.4)$$

where Γ_{bg} is the rate of background counts, Γ_s is the polarized signal rate we are interested in, t is time and $f_m = 2f_r$ is the modulation frequency. Clearly, the detected time series $\Gamma(t)$ is modulated by the frequency f_m and the modulation amplitude corresponds to half of the SPP-enhanced SPDC rate Γ_s.

In the experiment, a custom-made motorized rotator was used in position A1 in Fig. 3.5a to rotate the analyzer. The rotation frequency was $f_r = 2\,\text{Hz}$ resulting in the modulation frequency $f_m = 4\,\text{Hz}$. The time series of the PMT was detected with LabJack U6 in stream mode at the detection rate 40 Hz over $T = 60\,\text{s}$ time period.

The logic of lock-in amplification was conducted in software as a post-processing step [88, 89]. The signal rate is given by $\Gamma_s = 2\sqrt{X^2 + Y^2}$, where

$$X = \frac{1}{T}\int_0^T dt\,\Gamma(t)\cos(2\pi f_m t), \qquad (3.5)$$

$$Y = \frac{1}{T}\int_0^T dt\,\Gamma(t)\sin(2\pi f_m t). \qquad (3.6)$$

An example of lock-in amplification is shown in Fig. 3.6. The experimental data is indeed modulated with frequency 4 Hz (see the Fourier spectrum

in the inset of Fig. 3.6) and the reconstructed signal by lock-in amplification clearly follows the noisy experimental data.

3.3.3 Results

The structure in Fig. 3.4 was measured in the custom-built goniometer in three different configurations. First, the SPP resonances of the structure were measured at different wavelengths in order to characterize the structure and to map the angles of the SPP resonances for later use. Secondly, the nonlinear properties of the structure were verified by plasmonically enhancing SHG. Finally, the goniometric setup was configured to measure the SPP-enhanced SPDC by unequal splitting of $\lambda_p = 532\,\text{nm}$ pump laser into $\lambda_i = 1580\,\text{nm}$ idler and $\lambda_s = 800\,\text{nm}$ signal beams.

3.3.3.1 Reflection curves

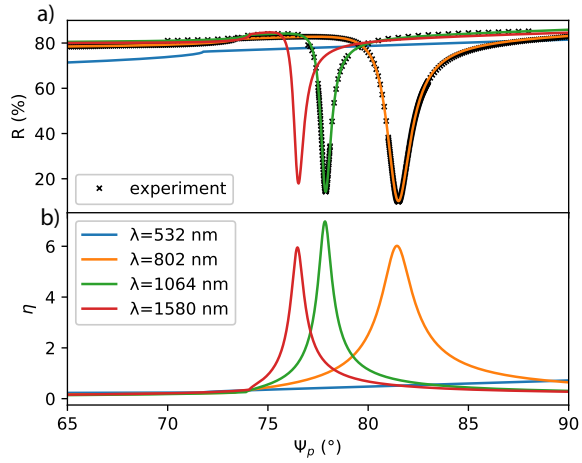

Figure 3.7: a) Measured (black crosses) and modeled (solid lines) dependence of the reflection coefficient (R) on the angle of incidence Ψ_p of the laser beam for different wavelengths λ. b) The theoretical enhancement factor (η) near Ag-SiO_2 surface. [II]

The resonances of the structure were measured at two wavelengths: 802 nm and 1064 nm. The laser beams were p-polarized with the Fresnel rhomb FR1, the additional cleanup filter F2 was not necessary and on the sensor arm, only the detector D2 was used. In the case of 802 nm laser, photodiode Thorlabs PM100 with S130A head was used and in the case of the pulsed 1064 nm laser, Melles Griot 13 PEM 001 with thermopile sensor head was used instead.

Measured reflection curves (black crosses) are shown in Fig. 3.7a along with theoretical modeling (solid lines). Sharp plasmonic resonances are clearly visible as a minimum in the reflection (R) and as a maximum in the theoretical field enhancement factor (η) in Fig. 3.7b. The modeling of reflection curves and the calculation of enhancement factors were done by a standard TMM and the unknown parameters were fitted. An excellent overlap of the experimentally measured and theoretically modeled reflection curves was achieved (see Fig. 3.7a). The derived thicknesses (d) and complex refractive indices (n) of the layers of the modeled structure are listed in table 3.2. The refractive indices of the N-SF11 and SiO_2 perfectly match the known values from www.schott.com and from Ref. [39]. The Al_2O_3 layer in the model is effective and also accounts for the losses in the IML layer and consequently the thickness of this layer is also effective. The fitting of the silver layer parameters revealed, that, indeed, the thickness of the silver layer is close to 50 nm as expected. The complex refractive index of the silver film match quite well with the values reported in Ref. [90].

Table 3.2: The thicknesses (d) and complex refractive indices (n) of the layers of the structure in Fig. 3.4 for different wavelengths. [II]

	$\lambda = 802\,\text{nm}$		$\lambda = 1064\,\text{nm}$	
	d (nm)	n	d (nm)	n
N-SF11		1.765		1.754
Al_2O_3	10.0	$1.76 + 0.055i$	10.0	$1.76 + 0.055i$
Ag	52.9	$0.146 + 5.80i$	50.8	$0.204 + 8.07i$
SiO_2		1.538		1.534

The enhancement factors and the reflection curves were also estimated for wavelengths 532 nm and 1580 nm by using the refractive index data from Refs. [39, 90]. In the case of the green laser, the plasmonic resonance is shifted out of the measurable range of the angle of incidence of the pump beam and no sharp minimum in the reflection curve is visible. On the other hand, in the case of wavelength 1580 nm a good quality plasmonic resonance is visible and the field enhancement around six times is predicted. Overall, the maximum field enhancement is up to seven times, which is considerably lower than the values predicted in our previous theoretical calculations in Fig. 3.2a. This difference is accounted for the different data for the silver refractive index. In Ref. [I], the silver refractive index data from P. B. Johnson and R. W. Christie [38] was used, however, in this case, the refractive index of the silver is more similar to the data measured by A. D. Rakic [90]. Such significant variance of the silver refractive index on the deposition and measurement process is well known [91]. It is also concluded, that the quality of the deposited silver film could be significantly improved by the optimization of the deposition process.

3.3.3.2 SPP-enhanced SHG

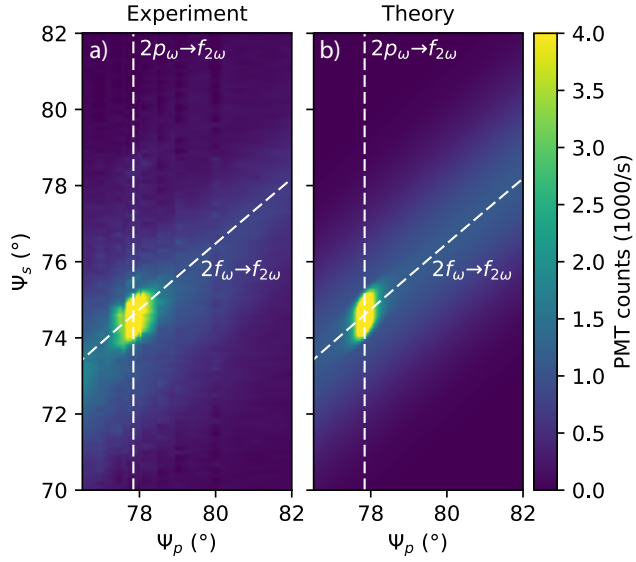

Figure 3.8: The experimentally measured (a) and theoretically predicted (b) signal rates of SPP-enhanced SHG. [II]

Next, the nonlinearities of the structure were tested by plasmonically enhancing the SHG. To do that, the pulsed 1064 nm pump laser was p-polarized by Fresnel rhomb FR1 and was spectrally cleaned by three interference filters (Semrock FF01-593-LP, BLP01-633R and FF01-715-LP) in the position F2. After the interaction with the object, the laser was filtered out by two interference filters (Semrock FF01-535/150-25 and FF03-525/50-25) in the position F3 and the SHG signal was detected through p-polarized analyzer A1 by Hamamatsu H6240-02 PMT. The output pulses of the PMT were counted by LabJack U6 with collection time 1 s at the distance 22.3 cm from the rotational axis O.

The experimental results are shown in Fig. 3.8a, where the SHG signal is scanned over the angle of incidence of the pump beam Ψ_p and over the angle of the sensor Ψ_s. In our case, two competing processes of SHG can happen. Firstly, pure photonic process ($2f_\omega \rightarrow f_{2\omega}$), where two photons at the pump frequency produce one photon at twice the frequency. Secondly, SPP-enhanced SHG ($2p_\omega \rightarrow f_{2\omega}$), where pump laser excites two plasmons at the pump frequency, which produce single photon at twice the frequency. The first, pure photonic process, can take place for every angle of the incidence of the pump beam (see dashed line in Fig. 3.8a), however, the SPP-enhanced SHG can only take place at a specific angle of incidence of the pump beam corresponding to the plasmonic resonance. Indeed, the experimental results in

Fig. 3.8a display a weak SHG signal at the predicted angles of the sensor and strongly enhanced SHG signal near the plasmonic angle of the pump beam. It is a direct evidence, that our structure supports the plasmonic enhancement of second-order nonlinear processes.

The theoretical calculations in Fig. 3.8 were done by nonlinear TMM [III], which will be described in Sec. 4.2.3. The match between the experimentally measured and theoretically predicted values is really good.

3.3.3.3 SPP-enhanced SPDC

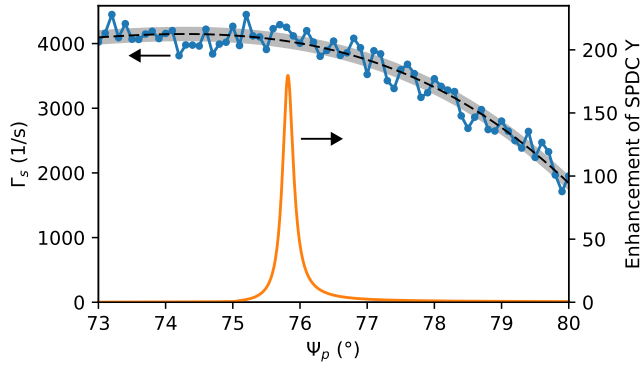

Figure 3.9: The measured SPDC signal Γ_s dependence on the angle of incidence of the pump beam Ψ_p. The dashed black line shows the general trend and the shaded region around it corresponds to 95 % confidence interval resulting from the shot noise. The theoretical enhancement factor of SPDC is displayed in the second axis. [II]

Finally, the goniometric setup was configured to measure SPP-enhanced SPDC by unequal splitting of $\lambda_p = 532\,\text{nm}$ pump laser into $\lambda_i = 1580\,\text{nm}$ idler and $\lambda_s = 800\,\text{nm}$ signal beams. The initial plan was to observe the equal splitting of 402 nm laser, however, the IML and the N-SF11 prisms were incompatible with the violet laser – the prism become luminescent (see Fig. 3.5d) and IML was not photostable. As a workaround, an unequal splitting of the green laser was observed instead. In the experiment, only the signal beam with wavelength $\lambda_s = 800\,\text{nm}$ was observed due to the spectral sensitivity restrictions of the sensor.

Two laser cleanup filters (Semrock FF01-535/150-25 and FF03-525/50-25) were added to the position F2. On the detection side, three interference filters (one Semrock BLP01-633R and two Semrock FF01-800-12) were employed to filter out the pump laser and to register only the signal beam. To boost the signal-to-noise ratio, the lock-in amplification by rotating analyzer was used (described in Sec. 3.3.2.2). As the generated SPP-enhanced SPDC

signal originates from the plasmonic mode, then the corresponding angle of the sensor could be easily precalculated on the basis of the reflection curve measurements in Fig. 3.7a. The only remaining free parameter is the angle of incidence of the pump laser that was scanned to select desired splitting ratio.

The results are shown in Fig. 3.9. The measured SPDC signal Γ_s dependence on the angle of incidence of the pump beam Ψ_p is given by blue solid lines with dots. It is expected to have a single maximum around $\Psi_p \approx 75.8°$ (see the second axis of Fig. 3.9), however, it is not observed in the experimental results. The dependence of the SPDC signal on the angle of incidence of the pump laser is smooth and has a decreasing trend. The dashed black line shows the general trend and the shaded region around it corresponds to 95 % confidence interval resulting from the shot noise – the noise in our measurements is bit higher, but still close to the theoretical limitation by shot noise.

From Fig. 3.9, it is estimated, that the noise of the measurement is around $400\,\mathrm{s}^{-1}$. It corresponds to a minimum detectable yield of SPDC, calculated from the power of the pump laser and from the quantum efficiency of the PMT, around $6 \cdot 10^{-14}$. As no peak of the signal around the predicted angle is visible, it is concluded, that the yield of SPP-enhanced SPDC must be lower than the minimum detectable yield of SPDC of our measurement system. This, however, contradicts our predictions, that SPP-enhanced SPDC is enhanced around 200 times (see the second axis of Fig. 3.9) from usual yield around 10^{-12}.

3.4 Conclusions

In this chapter theoretical introduction to the SPP-enhanced SPDC was given and a possible experimental realization was described. The modeling in this chapter was only limited to the calculation of enhancement factors and no full modeling was attempted. The enhancement factor of SPDC up to $4 \cdot 10^4$ was predicted in the case of 50 nm thick silver film and phase-matching conditions were studied to illustrate the possibility of perfect phase-matching.

In the second part, the experimental details were reviewed and the results were presented. It was shown that the yield of SPP-enhanced SPDC must be lower than $6 \cdot 10^{-14}$. This, however, contradicts our theoretical predictions. To get insight into the reasons for this discrepancy between the experimental work and the enhancement calculations, a full modeling of the SPP-enhanced SPDC is required and will be the topic of the next chapter.

4 Modeling of enhanced SPDC (publications III, IV)

4.1 Introduction

An idea to enhance SPDC by SPPs was introduced in chapter 3 and the enhancement up to $4 \cdot 10^4$ were estimated by simple considerations of field enhancement. However, these simple considerations are only useful for illustrating the great potential of SPP-enhanced SPDC. Otherwise, they provide only very limited insight into the process.

Up to now, we have assumed, that the yield of SPDC is on the order of 10^{-12}. This, however, is the yield of SPDC in the case of 1 mm thick good nonlinear crystal in the case of perfect phase-matching by birefringence. Assuming the same yield from the modified geometry supporting SPPs (Fig. 3.1b) is not justified, as the materials, participating fields and the geometry are completely different. Therefore, to calculate the yield of SPP-enhanced SPDC, more complex methods must be used to fully model the generation of SPDC in the structure in Fig. 3.1b. Only in this way, it is possible to predict if the large enhancement of SPPs is overcoming the losses introduced by the different geometry and to explain the results of the experimental work. The main factors influencing the generation of SPDC in the SPP-enhanced structure are:

1. **Enhancement**

The enhancement calculations presented in Sec. 3.2 are only rough estimates. The problem of calculating the true field enhancements is twofold.

Firstly, vacuum fluctuations and the enhancement of vacuum fluctuations in plasmonic mode must be correctly accounted. Up to now, it is assumed that all the participating vacuum fluctuations are in plasmonic modes that are equally enhanced. This, however, might not be true, as the resonances of surface waves are narrow. To realistically model the enhancements, it must be taken into account that the vacuum fluctuations are only enhanced in a narrow angular range supporting plasmons.

Secondly, up to now, only infinite plane waves were considered. This approximation holds reasonably well in the case of ordinary SPDC geometry (Fig. 3.1a), however, in the case of structures supporting resonant modes the enhancement factor starts to depend on the exciting beam properties (e.g. the waist size of a Gaussian beam). To realistically model the structures supporting very narrow resonant modes, the plane wave approximation must be dismissed and realistic beams (e.g. Gaussian beam) must be used.

2. **Out-coupling efficiency**

Another factor, irrelevant in the case of ordinary SPDC, is the efficiency of the out-coupling. In the case of ordinary SPDC, all signal and idler photons generated inside the nonlinear crystal will be radiated out of the nonlinear crystal as there is no absorption. However, in the case of SPP-enhanced SPDC, the signal and idler are in plasmonic mode – they might get absorbed in the metal. So, high out-coupling efficiency is essential for enhancing SPDC – otherwise, the effect of the enhancement would be lost by the absorption of the generated quanta.

3. **Phase-matching and coherent buildup**

Fulfilling phase-matching conditions are really important for an efficient SPDC as otherwise, no coherent buildup of a signal can take place. Here, the structures of ordinary and SPP-enhanced SPDC have a significant difference. In the case of ordinary SPDC, birefringence must be employed for a perfect phase-matching and a coherent buildup happens along the z-axis (Fig. 3.1a). Contrary, in the case of SPP-enhanced SPDC, a perfect phase-matching is possible without birefringent materials and a coherent buildup can only take place along the x-axis (Fig. 3.1b). In addition to different phase-matching requirements and different coherent buildup direction, also the losses of SPPs pose limitations and must be carefully studied.

4. **Effective nonlinearity**

Another problem with the simple model is taking account the interaction with a nonlinear crystal. In the case of usual SPDC, all participating fields are inside nonlinear medium (Fig. 3.1a), however, in the case of SPP-enhanced SPDC (Fig. 3.1b), only a part of the fields of the plasmonic mode are inside the nonlinear medium (the metal is taken to be linear). In other words, the effective nonlinearity is reduced because the fields are only partially inside the nonlinear medium.

5. **Beam width study**

Finally, the pump beam width must be considered. The effect here is twofold. Firstly, the beam width influences the enhancement factors (see point 1) and secondly, it influences the coherent buildup. As already discussed, the coherent buildup in the case of SPP-enhanced SPDC is taking place in the x-direction (see Fig. 3.1b). However, as the coherent buildup can only take place in the presence of the pump beam, then the beam width also limits the maximum coherent buildup length – it cannot be longer than the width of the beam. So there exists a minimal width of the beam from which further reduction in the beam width will also cause the reduction in the efficiency of the process.

These are the five main factors influencing the generation of SPDC in resonant structures. To reliably model and to provide insight into the mechanisms of the SPP-enhanced SPDC, these factors must be addressed. To do

that, several extensions were developed for the standard TMM to fully model the SPDC generation in resonant structures. The new methods were used to estimate, compare and address the limitations of the generation of SPDC in three types of resonant structures supporting SPPs, LRSPPs and GDWs (Sec. 4.3).

4.2 Methods

4.2.1 Transfer-matrix method (TMM)

4.2.1.1 Introduction

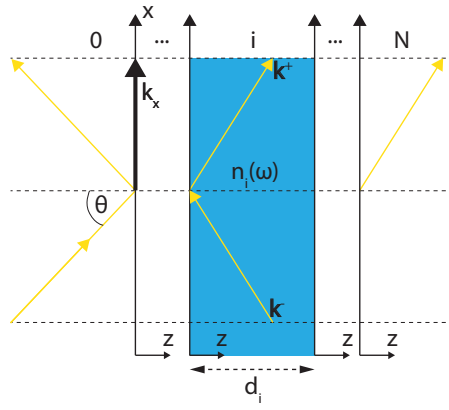

Figure 4.1: The schematic of a layered structure modeled by TMM. The layers are numbered by $i \in \{0 \dots N\}$ and each layer is described by a complex refractive index $n_i(\omega)$ and thickness d_i. The light is incident from the left at an angle of incidence θ. [III]

One of the main methods to model optical stratified (layered) structures is the transfer-matrix method (TMM, also standard/usual TMM). TMM is a fast and accurate method to solve Maxwell equations in layered structures. The matrix formalism of TMM was first proposed by F. Abeles in Ref. [92] and several good reviews of the method have been written since the original publication [93, 94]. Here, also a short review of the method will be presented, as several extensions were built on top of it.

The schematic of a layered structure is shown in Fig. 4.1. The layers are numbered from 0 to N and the first and last mediums are taken to be semi-infinite. The plane of incidence is taken to be xz-plane and in the x- and y-direction the structure is assumed to be uniform. In the simplest case, if the optical materials are assumed to be non-magnetic and isotropic, each layer is described only by its thickness d_i and its complex refractive index $n_i(\omega)$, where i denotes the index of the layer (see Fig. 4.1). The structure is illuminated by a

plane wave incident from the leftmost layer at an angle of incidence θ. The goal of TMM is to calculate the power flows of the reflected and transmitted plane waves and electrical/magnetic field distributions everywhere in the structure. Note, that every layer has its separate origin of the z-axis.

We only consider a s-polarized light to introduce the main components of TMM: the only independent field component is E_y, the other two non-zero field components H_x and H_z directly follow from the electrical field by Eq. 2.19. In each layer i, the solution of the electrical field is given as a sum of a forward- and backward-propagating waves

$$E_{y,i} = E^{+}_{y,i} + E^{-}_{y,i}. \tag{4.1}$$

The forward- and backward-propagating plane waves are defined in usual way $E^{\pm}_{y,i} = A^{\pm}_{y,i} e^{i\mathbf{k}^{\pm}_i \cdot \mathbf{r}}$, where $A^{\pm}_{y,i}$ is the complex amplitude and $\mathbf{k}^{\pm}_i = k_x \hat{\mathbf{x}} + k^{\pm}_{z,i} \hat{\mathbf{z}}$ is the wavevector. All plane waves in the structure have the same x-component of the wavevector as the incident plane wave $k_x = \omega n_0(\omega) \sin(\theta)/c$, because of the continuity of the tangential components of wavevectors. This is also the reason, why the solution in a layer (Eq. 4.1) could be represented only as a sum of two plane waves. The y-component of the wavevector is zero and the z-component depends on the layer's refractive index and is given by

$$k^{\pm}_{z,i} = \pm\sqrt{k_i^2 - k_x^2}, \tag{4.2}$$

where the magnitude of the wavevector is $k_i = \left|\mathbf{k}^{\pm}_i\right| = \omega n_i(\omega)/c$. As the propagation of all plane waves in the x-direction is the same, $E^{\pm}_{y,i}(\mathbf{r}) = E^{\pm}_{y,i}(z)\, e^{ik_x x}$, and determined only by the angle of incidence θ, only the z-dependence of the fields $E^{\pm}_{y,i}(z)$ is unknown.

4.2.1.2 Matrices

The main components of TMM are the propagation and transfer matrices, which relate the field amplitudes from the beginning of the layer to the end and from one layer to the next one, respectively. The propagation of the plane wave from the beginning of the layer ($z = 0$) to the end of the same layer ($z = d_i$) is given by a multiplication by a phase factor. In compact matrix form, where hat symbol denotes column vector (see Eq. 2.1), the propagation of fields in a single layer is given by

$$\hat{\mathbf{E}}_{y,i}(d_i) = \mathbf{M}^{i}_{P} \cdot \hat{\mathbf{E}}_{y,i}(0), \tag{4.3}$$

where dot implies matrix multiplication and propagation matrix is given by

$$\mathbf{M}_P^i = \begin{pmatrix} e^{ik_{z,i}^+ d_i} & 0 \\ 0 & e^{ik_{z,i}^- d_i} \end{pmatrix}. \tag{4.4}$$

Note, that absorption coefficients are incorporated into complex wavevectors $\hat{\mathbf{k}}_{z,i}$.

Another component of TMM formalism is the transfer matrix, which relates the field amplitudes from the end of layer i to the beginning of the next layer $j = i + 1$

$$\hat{\mathbf{E}}_{y,j}(0) = \mathbf{M}_T^{ij} \cdot \hat{\mathbf{E}}_{y,i}(d_i). \tag{4.5}$$

The transfer matrix straight-forwardly follows from the continuity of the E_y and H_x components of the fields and is given by

$$M_T^{ij} = \frac{1}{2} \begin{bmatrix} 1 + \frac{k_{z,i}^+}{k_{z,j}^+} & 1 - \frac{k_{z,i}^+}{k_{z,j}^+} \\ 1 - \frac{k_{z,i}^+}{k_{z,j}^+} & 1 + \frac{k_{z,i}^+}{k_{z,j}^+} \end{bmatrix} \tag{4.6}$$

for s-polarization, currently under interest.

The system matrix, a single matrix describing the propagation and transfer of fields through the whole structure, is given by a multiplication of all transfer and propagation matrices

$$\mathbf{M}_S = \prod_{i=0}^{N-1} \mathbf{M}_P^i \cdot \mathbf{M}_T^{ij}. \tag{4.7}$$

The amplitudes of the main field components in the first and last medium are then related by

$$\begin{bmatrix} E_{y,N}^+(0) \\ E_{y,N}^-(0) \end{bmatrix} = \mathbf{M}_S \cdot \begin{bmatrix} E_{y,0}^+(0) \\ E_{y,0}^-(0) \end{bmatrix}. \tag{4.8}$$

Usually, the system is illuminated from the leftmost layer by a plane wave with a known amplitude $E_{y,0}^+(0) = 1$ (one is arbitrarily chosen) and no illumination is incident from the opposite direction $E_{y,N}^-(0) = 0$. The two unknowns in Eq. 4.8, the amplitudes of the reflected ($E_{y,0}^-(0)$) and transmitted ($E_{y,N}^+(0)$) plane waves, can be easily found

$$E_{y,0}^-(0) = \mathbf{M}_S[2,1] / \mathbf{M}_S[2,2] \tag{4.9}$$

$$E_{y,N}^+(0) = \det(\mathbf{M}_S) / \mathbf{M}_S[2,2]. \tag{4.10}$$

Eqs. 4.9 and 4.10 solve the system. The field amplitudes in every layer can now be easily found by transferring and propagating the $\hat{\mathbf{E}}_{y,0}(0)$ from the first layer to every other layer.

4.2.1.3 Power flows and fields

As a final step, the amplitudes in every layer must be converted to the quantities we are really interested in: reflection/transmission coefficients and electric/magnetic field distributions. The calculation of power flows is straightforward by time averaged Poynting vector

$$\langle \mathbf{S} \rangle = \frac{1}{2} \operatorname{Re} [\mathbf{E} \times \mathbf{H}^*] \tag{4.11}$$

and in the case of s-polarization, the z-component is simply given by

$$\hat{\mathbf{S}}_{z,i} = \frac{1}{2\omega\mu_0} \operatorname{Re} \left[k_{z,i}^+ \right] \left| \hat{\mathbf{E}}_{y,i} \right|^2 . \tag{4.12}$$

The reflection and transmission coefficients could be calculated by $R = S_{z,0}^-/S_{z,0}^+$ and $T = S_{z,N}^+/S_{z,0}^+$, respectively.

The field distribution of the main component inside the layer i can be found as

$$\hat{\mathbf{E}}_{y,i}(\mathbf{r}) = \hat{\mathbf{E}}_{y,i}(0)\, e^{i\hat{\mathbf{k}}_i \cdot \mathbf{r}} \tag{4.13}$$

and the corresponding magnetic field components are given by Eq. 2.19 and can be written in a compact form as

$$\hat{\mathbf{H}}_i = \frac{1}{\omega\mu_0} \left(\hat{\mathbf{k}}_i \times \hat{\mathbf{E}}_i \right). \tag{4.14}$$

The total fields are just sums of the forward and backward-propagation components as in Eq. 4.1.

4.2.2 Transfer-matrix method for realistic waves

One of the limitations of standard TMM is that it only uses infinite plane waves for calculations. In general, this is a very good approximation of realistic beams (e.g. a Gaussian laser beam with a waist size $w_0 = 1\,\mathrm{mm}$), however in the case of resonant structures with very narrow resonances (e.g. LRSPPs and GDWs) this approximation does not hold.

The reason for this was explained in Sec. 2.1.4: all realistic beams could be decomposed into plane waves with different propagation directions

and amplitudes. Plane wave approximation works well until the resonances of a structure are not narrower than the angular spread of the exciting beam. For an example, the angular spread (see Fig. 2.2b) of 1 mm wide Gaussian beam is around 0.001°. Indeed, such beam could be approximated with a plane wave very well in most cases as we usually do not have a resonance in a structure that is so narrow. However, this is not so in the case of LRSPPs and GDWs – the resonances can be even narrower. Using infinite plane waves in such case would not provide correct results – actually only a part of the realistic beam interacts with the resonance.

To overcome this limitation of standard TMM and to reliably model structures with very narrow resonances the standard TMM were extended to support excitation with realistic beams [III, 95]. The strategy to achieve it is straight-forward. Firstly, the angular spectrum representation (2.1.4) is used to decompose the realistic beam into plane wave components. Secondly, the propagation of each plane wave component is solved separately by the standard TMM. Finally, the resulting fields are integrated to get the final field distribution inside the structure.

From the computational point of view, it is convenient to use a fast Fourier transform (FFT) to calculate the amplitudes of the plane wave components of an arbitrary beam profile. For integration, the trapezoidal rule can be used. It is found, that it is sufficient to use only 50 plane wave components to represent a common Gaussian beam reasonably well in not too complicated structure [95].

To calculate reflected and transmitted power flows, the simple formula Eq. 4.12 does not hold because the calculation of Poynting vector is a nonlinear operation. Moreover, straight-forwardly calculating Poynting vector (by Eq. 4.11) means the calculation of triple integral: over x-coordinate (see Fig. 4.1) and the other two over x-components of the wavevectors (one for calculating electric field and the other for magnetic field). Numerical calculation of such integral requires a fair amount of computational power. Fortunately, it turns out that the calculation of the power flows could be simplified [II, 95]: integrals could be rearranged and one, integration over coordinate, could be solved analytically. For the s-polarization, the power flow through the window with size $(x_0 \dots x_1, 0 \dots L_y)$ is given by

$$P_s = \frac{L_y}{2\omega\mu_0} \operatorname{Re}\left[I_{ks}\right] \tag{4.15}$$

$$I_{ks} = \iint_{-k}^{k} dk_x dk'_x \, k'_z \hat{E}^*_{0y}\left(k'_x\right) \hat{E}_{0y}\left(k_x\right) F_x F_z, \tag{4.16}$$

where F_x and F_z describe the interference between the plane waves in x- and z-direction, respectively. Those coefficients are defined by

$$F_x(\Delta k) = \int_{x_0}^{x_1} dx\, e^{i\Delta k x} = \frac{-i}{\Delta k}\, e^{i\Delta k x}\Big|_{x_0}^{x_1} \tag{4.17}$$

$$F_z(k_z, k_z') = e^{i\left(k_z - k_z'\right)z}, \tag{4.18}$$

where $\Delta k = k_x - k_x'$. Calculation of double integral in Eq. (4.15) is readily doable by numerical methods.

4.2.3 Nonlinear transfer-matrix method (NLTMM)

4.2.3.1 Introduction

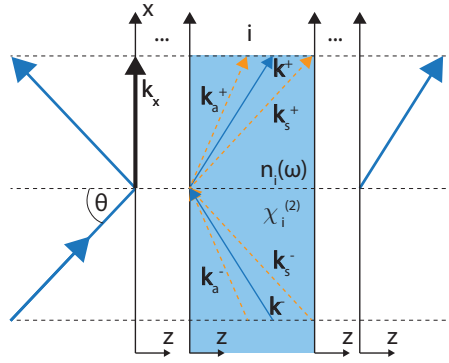

Figure 4.2: The schematic of a layered structure modeled by NLTMM. The layers are numbered by $i \in \{0 \ldots N\}$ and each layer is described by a complex refractive index $n_i(\omega)$, thickness d_i and second-order nonlinearity $\chi_i^{(2)}$. The light is incident from the left at an angle of incidence θ. [III]

As discussed in Sec. 2.1.3.1, the solution of the nonlinear wave equation is no longer a simple plane wave, as the generation of nonlinear signal happens in a nonlinear medium. In the case of non-depleted pump wave approximation, the solution of nonlinear wave equation is given by a sum of three plane waves (in each direction) by Eq. 2.43 (see Fig. 4.2): one usual homogeneous solution (no subscript) and two inhomogeneous solutions (denoted by subscripts "s" and "a"). It is the general case if both pump waves have both the backward- and forward-propagating components.

Conveniently, the amplitudes of the three plane waves of the solution of nonlinear wave equation are not independent/unknown. Actually all the amplitudes of the inhomogeneous waves $\mathbf{B}_{s|a}^{\pm}$ are constants fixed by Eqs. 2.44 and 2.45 – the only unknowns are the amplitudes of the homogeneous plane waves $\mathbf{A}^{\pm}$. Finding these amplitudes means solving the structure.

In this section, ordinary TMM is extended to calculate the second-order nonlinear processes. The nonlinear TMM (NLTMM) covered in this section is general and the method will be further specified in Sec. 4.2.4 to calculate the generation of SPDC. Like in Sec. 4.2.1, we assume the generated wave to be s-polarized (the pump beams may also be p-polarized). Again, the task reduces to finding the z-dependence of the y-component of the electric field, the magnetic field components directly follow from it by Eq. 2.46. Here only a short summary of the method will be given, the derivations can be found in Ref. [III].

4.2.3.2 Matrices

As in Sec. 4.2.1.2, the propagation matrix connects the fields at the beginning $\hat{\mathbf{E}}_{y,i}(0)$ and at the end $\hat{\mathbf{E}}_{y,i}(d_i)$ of a layer. As materials are nonlinear, the general solution is no longer a single plane wave, but is given by Eq. 2.43 instead. Still, the connection between $\hat{\mathbf{E}}_{y,i}(0)$ and $\hat{\mathbf{E}}_{y,i}(d_i)$ is easy to find if the $\hat{\mathbf{A}}_y$ is expressed from $\hat{\mathbf{E}}_{y,i}(0)$ and substituted into $\hat{\mathbf{E}}_{y,i}(d_i)$ [III]. The resulting expression could be organized into a compact matrix form as in the case of linear TMM, however now we have an additional nonlinear term $\hat{\mathbf{N}}_P^i$

$$\begin{aligned} \hat{\mathbf{E}}_{y,i}(d_i) &= \mathbf{M}_P^i \cdot \hat{\mathbf{E}}_{y,i}(0) + \hat{\mathbf{N}}_P^i, && (4.19) \\ \hat{\mathbf{N}}_P^i &= \hat{\mathbf{B}}_{sy,i}\left(e^{i\hat{\mathbf{k}}_{sz,i}d_i} - e^{i\hat{\mathbf{k}}_{z,i}d_i}\right) + \\ &\quad \hat{\mathbf{B}}_{ay,i}\left(e^{i\hat{\mathbf{k}}_{az,i}d_i} - e^{i\hat{\mathbf{k}}_{z,i}d_i}\right). && (4.20) \end{aligned}$$

The matrix $\mathbf{M}_P^i$ is the same matrix as in the case of linear TMM and is given by Eq. 4.4.

By implying the continuity of E_y and H_x (calculated by Eq. 2.46) at the boundary of the layers i and $j = i+1$ we can derive the transfer matrix, which relates the electrical fields from the end of the layer $\hat{\mathbf{E}}_{y,i}(d_i)$ to the beginning of the next layer $\hat{\mathbf{E}}_{y,j}(0)$. Without explicit derivation, it is again possible to express the nonlinear contribution as an additional term to the linear transfer matrix

$$\hat{\mathbf{E}}_{y,j}(0) = \mathbf{M}_T^{ij} \cdot \hat{\mathbf{E}}_{y,i}(d_i) + \hat{\mathbf{N}}_T^{ij}, \tag{4.21}$$

where $\mathbf{M}_T^{ij}$ is the usual linear transfer matrix given by Eq. 4.6 and $\hat{\mathbf{N}}_T^{ij}$ is nonlinear contribution given by

$$\hat{\mathbf{N}}_T^{ij} = \hat{\mathbf{c}}_{s,ij} + \hat{\mathbf{c}}_{a,ij}, \tag{4.22}$$

where

$$c_{s,ij}^{\pm} = \frac{\pm 1}{2k_{z,j}^{+}}\left[\left(k_{sz,j}^{+}-k_{z,j}^{+}\right)\left(B_{sy,j}^{-}-B_{sy,j}^{+}\right)+ \left(k_{sz,i}^{+}-k_{z,i}^{+}\right)\cdot\left(B_{sy,i}^{+}e^{ik_{sz,i}^{+}d_i}-B_{sy,i}^{-}e^{-ik_{sz,i}^{+}d_i}\right)\right] \quad (4.23)$$

and completely analogous expression for $c_{a,ij}^{\pm}$.

The final part of NLTMM is to combine nonlinear propagation (Eq. 4.19) and transfer (Eq. 4.21) matrices into a nonlinear system matrix $\hat{\mathbf{N}}_S$ so the propagation of the fields through the whole structure is

$$\hat{\mathbf{E}}_{y,N}(0) = \mathbf{M}_S \cdot \hat{\mathbf{E}}_{y,0}(0) + \hat{\mathbf{N}}_S, \quad (4.24)$$

where $\mathbf{M}_S$ is usual system matrix given by Eq. 4.7. Again, the nonlinear contribution is just an additional term to linear TMM and is given by a recursive function

$$\hat{\mathbf{N}}_S = \hat{\mathbf{f}}(N) \quad (4.25)$$

$$\hat{\mathbf{f}}(i) = \mathbf{M}_T^{i-1,i}\cdot\left(\mathbf{M}_P^{i}\cdot\hat{\mathbf{f}}(i-1)+\mathbf{N}_P^{i}\right)+\mathbf{N}_T^{i-1,i} \quad (4.26)$$

with termination condition $\hat{\mathbf{f}}(i) = \hat{0}$ if $i \leq 0$.

To solve the Eq. 4.24, it is usually assumed (not a requirement), that the generated field is only due to the nonlinear interaction (i.e. there is no generated field incident on the structure). In such case, we have additional equations $E_{y,0}^{+}(0) = E_{y,N}^{-}(0) = 0$, which allows to solve Eq. 4.24 and to express reflected ($E_{y,0}^{-}$) and transmitted ($E_{y,N}^{+}$) electrical fields (generated inside the structure)

$$E_{y,0}^{-} = -\mathbf{N}_S[2,1]/\mathbf{M}_S[2,2], \quad (4.27)$$

$$E_{y,N}^{+} = \mathbf{N}_S[1,1] - \frac{\mathbf{N}_S[2,1]\,\mathbf{M}_S[1,2]}{\mathbf{M}_S[2,2]}. \quad (4.28)$$

4.2.3.3 Power flows and fields

The electrical fields inside the layer i can be found by

$$\hat{\mathbf{E}}_{y,i}(\mathbf{r}) = \left[\hat{\mathbf{E}}_{y,i}(0)\,e^{i\hat{\mathbf{k}}\cdot\mathbf{r}}+\hat{\mathbf{B}}_{sy,i}\left(e^{i\hat{\mathbf{k}}_s\cdot\mathbf{r}}-e^{i\hat{\mathbf{k}}\cdot\mathbf{r}}\right) +\hat{\mathbf{B}}_{ay,i}\left(e^{i\hat{\mathbf{k}}_a\cdot\mathbf{r}}-e^{i\hat{\mathbf{k}}\cdot\mathbf{r}}\right)\right] \quad (4.29)$$

and resulting magnetic field components can be calculated by Eq. 2.46. The total fields can be found by summation of forward- and backward propagating waves.

As we are usually interested only in the power generated by a nonlinear crystal sandwiched between the linear mediums, it is possible to use formulas of standard TMM (Eq. 4.12) .

4.2.3.4 NLTMM for realistic beams

Currently, NLTMM is only considered in the context of infinite plane waves like standard TMM. However, for similar reasons as in Sec. 4.2.2, it is necessary to extend NLTMM to realistic beams as well. Fortunately, it is possible to do it in a similar manner as in the case of standard TMM. However, as in the case of NLTMM, two input beams are present so that the number of integrals of angular spectrum representation (Eq. 2.52) is doubled. The plane wave amplitudes of angular spectrum representation could be readily calculated by NLTMM.

The calculation of the powers of the generated beam could be done in the same way as in Sec. 4.2.2 as the formulas to calculate the power (Eqs. 4.15 and 4.16) depend only on $\hat{E}_{0y}(k_x)$. Those dependencies are readily calculable by NLTMM.

4.2.4 Transfer-matrix method for SPDC

In the context of SPDC, usually pump ("p"), idler ("i") and signal ("s") notation is used to represent the participating waves (also used previously in Sec. 2.3 and in chapter 3). However, from here on we switch to the notation used in classical nonlinear optics (Sec. 2.1.3), because we model SPDC as a limiting case of DFG. The pump beam of SPDC is now denoted by subscript "1", the second input beam represents the idler beam and the signal has no subscript.

In this section, we finally arrive to a method to model SPDC in an arbitrary stratified structure. The general idea is to model SPDC as a limiting case of DFG: the second input beam of DFG is replaced with a very weak classical electrical field to replace vacuum fluctuations. Such methodology has been used before and it has been shown, that in such a way it is possible to exactly reproduce the results of the quantum theory of SPDC [84].

The vacuum fluctuations are present in every electromagnetic mode. To extract the electric field intensities associated with every mode, the quantum theory (Eq. 2.68) of SPDC and the classical theory of DFG (Eq. 2.51) were compared (Ref. [IV]) and the electric field intensity for the second input beam (in a vacuum) was found to be

$$|A_2|^2 = \Delta\lambda dk_{x2}\omega_2 \frac{\Omega_v}{\theta_v} \frac{\hbar}{8\varepsilon_0\pi^4} \frac{\omega^3}{c^3}. \tag{4.30}$$

As expected, the electric field intensity of vacuum fluctuation mode (given in a vacuum) with bandwidth ($\Delta\lambda dk_{x2}$) does not depend on the properties of the nonlinear crystal nor on the wavevector. Note, that the dependence on the generated frequency ω is due to the phase-matching condition (Eq. 2.64).

The electric field intensity by Eq. 4.30 is given only for a single electromagnetic mode with bandwidth $\Delta\lambda dk_{x2}$. However, in the process of SPDC, many modes of vacuum fluctuations participate in the generation of the signal detectable by a sensor. It is already assumed on the derivation of the quantum theory of SPDC (see Sec. 2.3.3), that the wavelength bandwidth $\Delta\lambda$ is small (signal is detected through a narrow-band filter), so the integration over $\Delta\lambda$ is not required.

On the other hand, the inclusion of vacuum fluctuation modes propagating to different directions is still required (integral over dk_{z2} in Eq. 2.68) as the viewing angle of the sensor θ_v is wide in comparison to the resonances. It means, that to include vacuum fluctuations into NLTMM an electric field intensity given by Eq. 4.30 must be included in every mode in the range $\bar{k}_{x2} - \Delta k_{x2} \ldots \bar{k}_{x2} + \Delta k_{x2}$ defined by Eqs. 2.69 and 2.70, because all of them participate in the generation of the signal reaching the detector. In reality, the situation is, of course, vice versa: the vacuum fluctuations are present in every mode and some limited amount of signal is collected by the sensor depending on the size and position of the sensor. Here, however, it is more convenient to include only these vacuum fluctuation modes that participate in the generation of the SPDC signal detectable by the sensor.

Computationally, it is convenient to use the functionality derived for beams with arbitrary profiles (see Secs. 4.2.2 and 4.2.3.4). We can just define a special kind of beam, that has an intensity of vacuum fluctuations in every mode in the range $\bar{k}_{x2} - \Delta k_{x2} \ldots \bar{k}_{x2} + \Delta k_{x2}$ and zero in every other mode. In such manner, the integration over vacuum fluctuation modes happens automatically. Special attention must be devoted to the coherence properties of the fields and taking account, that the vacuum fluctuation modes have an arbitrary phase relationship.

All of the methods described in this section were implemented in C++ for maximum performance and as an easy to use Python library. The code is open-source, documented and readily available at `github.com/ardiloot/NonlinearTMM`.

4.3 Results

This section will begin with a review of the results of full modeling of SPP-enhanced SPDC in the structure that was already introduced in chapter 3. Next, the results for structures supporting LRSPPs and GDWs will be presented in a comparative manner.

4.3.1 SPP-enhanced SPDC

4.3.1.1 Model setup

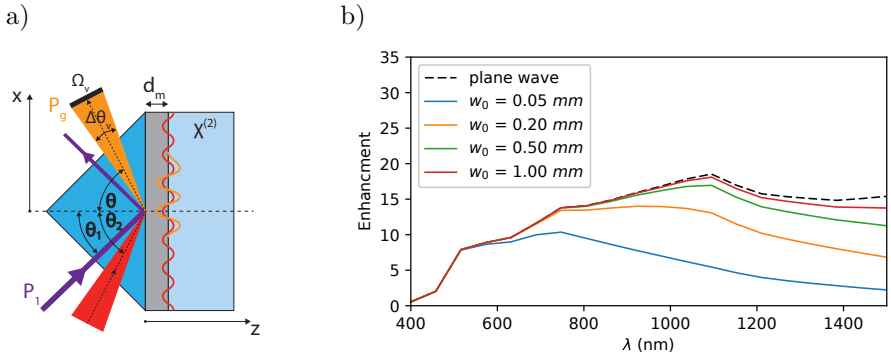

Figure 4.3: a) The structure for the modeling of SPP-enhanced SPDC: high refractive index prism, metal film and nonlinear crystal. The pump laser (power P_1) is incident through the prism at an angle of incidence θ_1. The artificial vacuum fluctuations are incident at an angle θ_2 and the generated SPDC signal (power P_g) is detected at an angle θ by a sensor (solid angle Ω_v and angular span $\Delta\theta_v$). b) The dependence of the field enhancement of SPPs on the wavelength and the waist size of the exciting Gaussian beam. [IV]

The structure under the investigation is shown in Fig. 4.3a. The refractive index of the prism is taken to be $n_p = 2.2$, the refractive index of the thin ($d_m = 50\,\mathrm{nm}$) silver film is from Ref. [38] and the refractive index of the nonlinear crystal is taken to be that of single crystal alpha quartz (Ref. [39]). Single crystal alpha quartz is preferred because of the relatively small refractive index – around 1.55 in the visible spectral region. The second-order nonlinear susceptibility of the nonlinear crystal is artificially taken to be

$$\chi^{(2)}_{xxx} = \chi^{(2)}_{yyy} = \chi^{(2)}_{zzz} = 4.4\,\mathrm{pm/V}, \tag{4.31}$$

which is comparable to the nonlinearity of BBO crystal. Such selection of the second-order susceptibility tensor helps to simplify the comparison of different

structures, as the effective nonlinearity does not depend on the polarization or on the field distributions of the participating fields.

The structures are illuminated by a green laser beam with wavelength $\lambda_1 = 532\,\text{nm}$ at an angle of incidence θ_1 (see Fig. 4.3a). If not further specified, the laser beam is a Gaussian shaped beam (in xz-plane) with waist size $w_0 = 1\,\text{mm}$, is p-polarized and the power of the beam is $P_1 = 100\,\text{mW}$.

The second input beam (red cone in Fig. 4.3a), representing vacuum fluctuations, consists of a range of modes $k_{x2} = \overline{k}_{x2} - \Delta k_{x2} \ldots \overline{k}_{x2} + \Delta k_{x2}$, where $\overline{k}_{x2}$ is connected to the angle θ_2 in Fig. 4.3a by

$$\overline{k}_{x2} = \frac{\omega_2}{c} n_p\left(\omega_2\right) \sin\theta_2 \tag{4.32}$$

and the limiting term Δk_{x2} follows from the sensor viewing angle $\Delta\theta_v$ by Eq. 2.70.

The angle of incidence of the generated beam is determined by the angle of incidences of both input beams and is

$$\theta = \operatorname{asin}\left(\frac{\omega_1 n_p\left(\omega_1\right)\sin\theta_1 - \omega_2 n_p\left(\omega_2\right)\sin\theta_2}{\omega n_p\left(\omega\right)}\right). \tag{4.33}$$

To be concrete, the solid angle window of the sensor is taken to be $\Omega_v = 7.6\,10^{-5}\,\text{sr}$ and the angular span in xz-plane to be $\theta_v = 0.5°$. In terms of frequency, we are only looking for the process where pump photons are equally split.

4.3.1.2 Yield of SPDC

Like in chapter 3, the calculations mainly focus on the "fpp" process in table 3.1, as it displays the highest enhancement and the phase-matching conditions are easy to fulfill. In this process, the second input beam, representing vacuum fluctuations, is in the plasmonic mode as is also the generated signal. As the vacuum fluctuations are fixed to excite plasmon mode, the only remaining free parameter is the angle of incidence of the pump beam θ_1 (the angle of the generated beam θ follows from it by Eq. 4.33) and we can calculate the yield of SPDC.

The yield of the SPP-enhanced SPDC is shown in Fig. 4.4a. The black dashed line corresponds to single plane wave excitation and the colored solid line corresponds to the realistic Gaussian beam excitation. Two peaks are present in Fig. 4.4a, the first one (highest, marked by vertical red line) corresponds to "fpp" process (see table 3.1) we are mainly interested in. The other peak corresponds to the alternative process of enhanced SPDC "ppf", where the pump beam directly excites plasmons as well, however, the generated

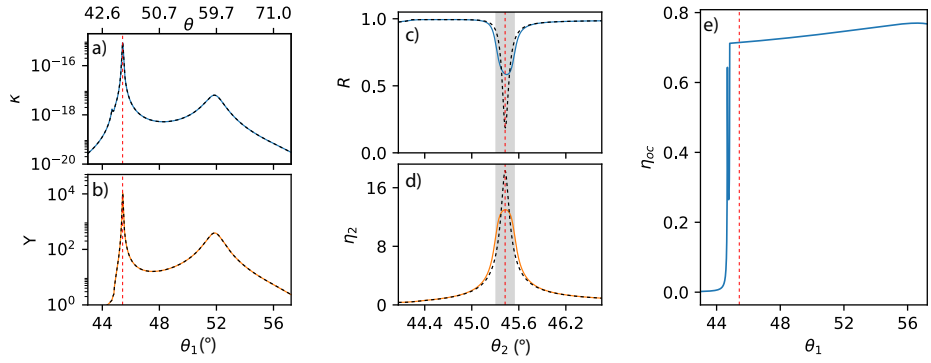

Figure 4.4: The dependence of the yield (a) and the enhancement factor (b) of SPP-enhanced SPDC on the angle of incidence of the pump beam θ_1. Also, the reflection curve (c) and the enhancement factor (d) of the second pump beam is shown. In Fig. 4.4e the dependence of the out-coupling factor on the angle of incidence of the pump beam is displayed. [IV]

quanta are in photonic mode instead of plasmonic. Between the peaks, the process is described by "fpf", as only the vacuum fluctuations are in plasmonic mode.

The maximum yield of SPP-enhanced SPDC is only around $\kappa \approx 9{\cdot}10^{-16}$, which is small. To address the reasons for a small yield, the five main factors influencing the generation of SPDC (see Sec. 4.1) will be addressed in the following sections.

4.3.1.3 Enhancement

By comparing the yield (Fig. 4.4a) to the enhancement factor (Fig. 4.4b) we see, that the enhancement by plasmonic fields is working as expected – the enhancement factor Υ and the yield κ have almost identical dependence on the angle of the pump beam. This is an expected result and proves that the simple enhancement considerations presented in Sec. 3.2 holds well. The enhancement factor of SPDC is up to 10^4, which is slightly smaller than estimated in Sec. 3.2. As mentioned in Sec. 4.1, the two influencing factors are: enhancement of participating vacuum fluctuation modes and the interaction of the pump beam with the narrow resonances.

Firstly, let's consider the possibility that not all of the participating vacuum fluctuation modes are equally enhanced. To illustrate, the angular sweep of reflection R and enhancement factor η_2 of the second input beam is calculated in Figs. 4.4c – 4.4d, where colored solid lines represent the calculations by artificial vacuum fluctuations beam and the dashed black lines correspond to the plane wave calculations. As expected, there is a minimum

in the reflection curve and a matching maximum in the enhancement factor near $\theta_2 \approx 45.4°$ corresponding to the SPP resonance. The second input beam (artificial vacuum fluctuations) are tuned to this resonance. The shaded areas in Figs. 4.4c – 4.4d represent the angular span of the artificial vacuum fluctuations corresponding to the sensor viewing angle $\Delta\theta_v$. Every mode in this shaded angular span will contribute to the generation of the useful SPDC signal detected by the sensor. From Fig. 4.4d it is visible, that not all of the modes of artificial vacuum fluctuations are equally enhanced, as the resonance of SPPs is narrow. It leads to a reduced enhancement (colored line in Fig. 4.4b) of the second input beam. Such kind of effect was not accounted in the simple model presented in Sec. 3.2 and is the main reason why the enhancement factor Υ is reduced in Fig. 4.4b. However, in this case, the effect is small, the enhancement is only reduced around ≈ 3 times as the resonance is not too narrow.

Secondly, let's consider the interaction of pump beam with narrow resonances. It is immediately clear, that our default Gaussian beam ($w_0 = 1\,\mathrm{mm}$) interacts with the resonances in this structure very well – the results of the yield of SPP-enhanced SPDC in Fig. 4.4a are identical for Gaussian beam and plane wave excitations. However, it is not the case if the beam width is reduced. In Fig. 4.3b, the maximum field enhancement of SPPs over the wide spectral range is calculated and the effect of the finite pump beam waist size is studied. The Gaussian beam with waist $w_0 = 1\,\mathrm{mm}$ interacts with SPPs in this structure very well – the enhancement factor closely resembles the enhancement with plane wave excitation in the visible spectral region and only slightly deviates from it in NIR spectral region. On the other hand, if the beam waist of the Gaussian beam is made narrower (eg. $w_0 = 0.05\,\mathrm{mm}$), only a fraction of the enhancement factor would be available and it will have a considerable effect on the enhancement of SPDC. In this case, the difference between infinite plane wave and Gaussian beam ($w_0 = 1\,\mathrm{mm}$) excitation is small, however, in the case of LRSPPs and GDWs, where resonances are considerably narrower, using realistic pump beam has a major effect on results.

Despite the large enhancement, the maximum yield of SPDC is small. The initial (not enhanced) yield of SPDC is very low (less than 10^{-20}), so the enhancement of four orders of magnitude is not enough. To understand the reasons for this low yield of SPDC in this geometry, the remaining four main factors influencing the SPDC will be studied.

4.3.1.4 Out-coupling efficiency

The next factor influencing the generation of SPDC in the SPP-enhanced structure is that the generated quanta is in lossy plasmonic mode and only a fraction of the generated signal outcouples to the prism. The calculated out-coupling efficiency is shown in Fig. 4.4e. In the case of "fpp" process, denoted by a vertical red line, the out-coupling efficiency is $\eta_{oc} \approx 71\%$. It is high and

is not a reason for a low yield of SPDC – only $\approx 29\%$ of the SPDC signal is lost by the absorption in the metal.

4.3.1.5 Phase-matching and coherent buildup

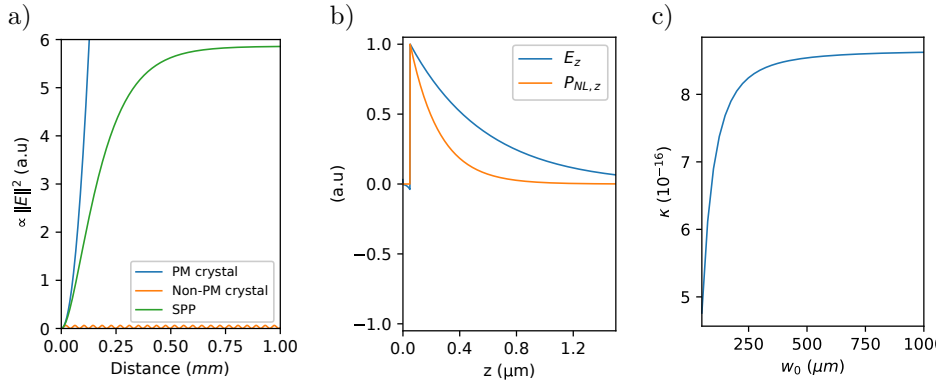

Figure 4.5: a) The coherent buildup curves of the SPDC signal. The buildup of SPP-enhanced SPDC signal is compared to perfect phase-matching (PM) and not phase-matched generation in an usual SPDC setup. b) The electrical field z-component of the SPP mode and the z-component of the nonlinear polarization. c) Dependence of the yield of SPP-enhanced SPDC on the width of the exciting Gaussian beam. [IV]

In the case of ordinary SPDC, fulfilling the phase-matching conditions are really important for an efficient generation of the signal. The coherent buildup curve for the SPP-enhanced SPDC is shown in Fig. 4.5a along with a comparison to ordinary SPDC buildup in perfectly phase-matched (PM) and not phase-matched (Non-PM) crystal. Note, that no influence of the field enhancement nor the effective nonlinearity is accounted for in the coherent buildup curves. It is visible, that at smaller distances $< \delta_c = 64\,\mu$m, the signal displays also a quadratic dependence on the distance, as in the case of perfect phase-matching. However, after $\approx 0.5\,$mm the coherent buildup curve is almost flat and approaching a constant value. To understand the behavior, the phase mismatch is calculated by methods described in Ref. [IV] and the results are presented in table 4.1. It turns out, that in the case of SPP-enhanced SPDC, the phase is perfectly matched $\mathrm{Re}\,[\Delta k] = 0\,\mathrm{m}^{-1}$, explaining the quadratic dependence at small distances, however, phase mismatch has also a considerable imaginary component $\Delta k = 7700i\,\mathrm{m}^{-1}$, which corresponds to the losses and leads to the limited coherent buildup length $\delta_c = 64\,\mu$m.

In terms of coherent buildup, the SPP-enhanced SPDC is indeed much weaker than the perfectly phase-matched generation in a thick nonlinear crystal in a conventional setup, because the coherent buildup is limited to the distance $< \delta_c = 64\,\mu$m. However, if one takes into account the enhancement of

four orders of magnitude, then at smaller distances ($< \delta_c$) the SPP-enhanced SPDC structure displays a superior yield of SPDC.

Table 4.1: The comparison of different surface waves for the enhancement of SPDC. Here plus signs (+) denote advantages and minus signs (–) disadvantages.

	SPPs	**LRSPPs**	**GDWs**
Yield of SPDC (κ)	$9 \cdot 10^{-16}$ (–)	$3 \cdot 10^{-14}$ (+)	$7 \cdot 10^{-14}$ (+)
Enhancement (Υ)	10^4 (++)	10^3 (+)	500 (–)
Out-coupling (η_{oc})	71 % (+)	68 % (+)	100 % (++)
Coherent buildup distance	$\Delta k = 7700i\,\mathrm{m}^{-1}$ $\delta_c = 64\,\mu\mathrm{m}$ (–)	$\Delta k = 36i\,\mathrm{m}^{-1}$ $\delta_c = 13.9\,\mathrm{mm}$ (++)	$\Delta k = 54i\,\mathrm{m}^{-1}$ $\delta_c = 9.2\,\mathrm{mm}$ (++)
Effective nonlinearity ($\chi^{(2)}_{eff}$)	2.5 pm/V (+)	0.80 pm/V (–)	0.44 pm/V (–)
Yield of SPDC ($w_0 = 10\,\mathrm{cm}$)	$9 \cdot 10^{-16}$ (–)	$0.3 \cdot 10^{-12}$ (++)	$0.08 \cdot 10^{-12}$ (+)

4.3.1.6 Effective nonlinearity

Another factor influencing the generation of SPP-enhanced SPDC signal is the value of effective nonlinearity. The study of the buildup curves revealed that the effective nonlinearity is approximately half of its maximum value (see table 4.1). It is an expected result, as only a part of the field distribution of SPPs is in nonlinear medium (metal is taken to be linear).

4.3.1.7 Beam width study

From Sec. 4.3.1.5, it becomes clear that a coherent buildup of the signal is really important. In the case of ordinary SPDC setup, the beam width does not influence the coherent buildup, however, in the case of a SPP-enhanced SPDC, it is an important parameter. Let's illustrate this by a simple example. If the beam width is very narrow (e.g. $10\,\mu$m), it is evident that the coherent buildup of the signal is also limited to the distance $< 10\,\mu$m. In other words, the beam width must have some minimal width in order not to destructively influence the yield of the SPP-enhanced SPDC, as the maximum interaction length is dictated by the width of the pump beam. The dependence of the yield of the SPP-enhanced SPDC on the waist size of the Gaussian pump

beam is shown in Fig. 4.5c. It is evident that the beam waist size $w_0 = 1\,\mathrm{mm}$ is sufficient. However, if the beam is made narrower, the yield reduces.

4.3.1.8 Conclusion

The summary of the results of the modeling of SPP-enhanced SPDC is shown in table 4.1. The enhancement factor up to four orders of magnitude is readily available, however, the yield of SPDC is still small in such structure. The study reveals, that the reason for the low yield is the limited coherent buildup distance ($64\,\mu\mathrm{m}$) and the yield of SPDC is small in comparison to the thick nonlinear crystal. On the other hand, in the case of miniature sources, the SPP-enhanced SPDC shows superior performance as the fields are enhanced and the coherent buildup distance is not yet a problem.

4.3.2 LRSPP-enhanced SPDC

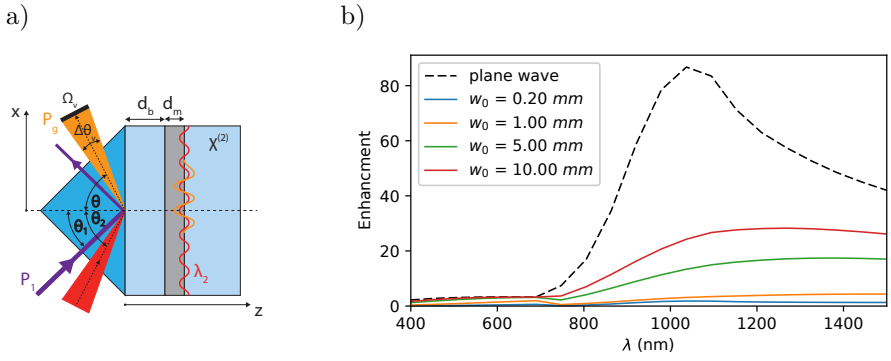

Figure 4.6: a) The structure for the modeling of LRSPP-enhanced SPDC: high refractive index prism, buffer layer, metal film and nonlinear crystal. The pump laser (power P_1) is incident through the prism at an angle of incidence θ_1. The artificial vacuum fluctuations are incident at angle θ_2 and the generated SPDC signal (power P_g) is detected at angle θ by a sensor (solid angle Ω_v and angular span $\Delta\theta_v$). b) The dependence of field enhancement of LRSPPs on the wavelength and the waist size of the exciting Gaussian beam.[IV]

The main problem limiting the enhancement of SPP-enhanced SPDC was the short coherent buildup length (see table 4.1). As a possible solution to increase the coherent buildup length, a structure supporting LRSPPs (Sec. 2.2.2) was considered. The structure under study is shown in Fig. 4.6a with an extra buffer layer between the prism and the metal film. The refractive index of the buffer layer is taken to be identical to the nonlinear medium's to support symmetric LRSPP modes and the thicknesses of the buffer layer

and the metal film are fixed at $d_b = 10\,\mu$m and $d_m = 10\,$nm, respectively. Otherwise, the model setup is identical to the case of SPP-enhanced SPDC (Sec. 4.3.1.1).

A summary of the results is shown in table 4.1. The yield of the LRSPP-enhanced SPDC ($\kappa \approx 3 \cdot 10^{-14}$) in the case of default Gaussian beam ($w_0 = 1\,$mm) is significantly higher than in the case of SPP-enhanced SPDC. This, however, is not connected to the increase in the enhancement factor, as it is decreased by a factor of ten in comparison to the SPP-enhanced SPDC. It is controversial, as the LRSPPs are known to display higher enhancement factors than SPPs.

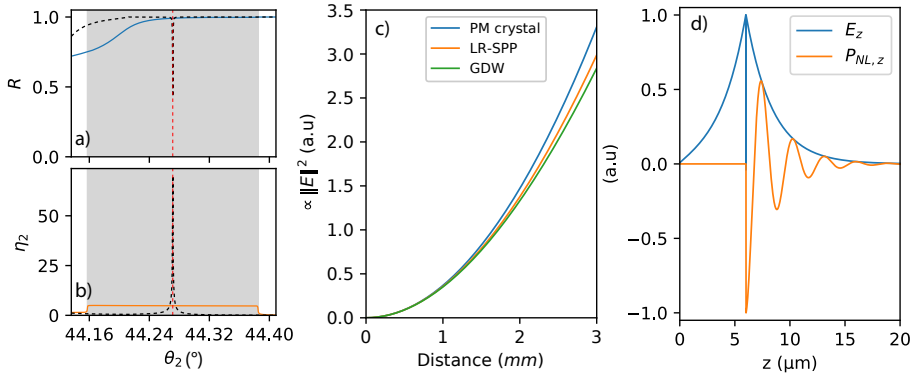

Figure 4.7: The angular sweep of the reflection (a) and the enhancement factor (b) of the second input beam. The buildup curve over the distance is shown in graph (c) for perfectly phase-matched crystal (PM) and for LRSPP- and GDW-enhanced SPDC. The electrical field z-component of the LRSPP mode and the z-component of the nonlinear polarization (d). [IV]

The reasons here are twofold: only a small part of the participating vacuum fluctuations are enhanced and the interaction of the realistic Gaussian beam ($w_0 = 1\,$mm) with the very narrow resonances of LRSPPs is weak. The latter is illustrated in Fig. 4.6b with maximum enhancement factor calculations. Indeed, in the case of plane wave excitation, the available enhancement factor is significantly higher than in the case of SPPs (see Fig. 4.3b). However, in the case of Gaussian beams, these enhancement factors are not realistically available due to the poor interaction with the very narrow resonances of LRSPPs. A similar problem appears also in the case of enhancement of the participating vacuum fluctuations. The angular sweep of the reflection and the enhancement factor of the second input beam are shown in Figs. 4.7a and 4.7b. Again, the second input beam is tuned to the resonance (denoted by red vertical line) and the participating vacuum fluctuations are denoted by the gray shaded area. It is clearly visible, that the resonance of LRSPP (black dashed line) is much narrower than the angular span of the vacuum fluctua-

tions – only a small part of the vacuum fluctuations are enhanced and thus only a fraction of the enhancement of LRSPPs is available (colored lines).

In terms of out-coupling, the LRSPP-enhanced SPDC works well and more than two thirds (table 4.1) of the generated signal is outcoupled to the prism.

The coherent buildup distance is significantly longer in comparison to the SPP-enhanced SPDC and is up to 13.9 mm. It is more than enough to not to be a limiting factor for SPDC. The coherent buildup curve over the distance is also shown in Fig. 4.7c, where clear quadratic buildup is visible as in the case of perfectly phase-matched (PM) crystal.

However, a new limiting factor is arising from the calculation of effective nonlinearity – it is only 18 % of its maximal value (see table 4.1). Moreover, if the buffer layer between the prism and the metal film is made nonlinear, then the effective nonlinearity decreases even further. To understand the origin of the effect, the z-dependence of the nonlinear polarization and the electric field of the LRSPP mode is plotted in Fig. 4.7d. It is evident, that the nonlinear polarization has oscillatory behavior over z-coordinate. It is caused by the fact, that now the pump wave is not evanescent nor in the buffer layer nor in the nonlinear crystal (contrary to the case of SPP-enhanced SPDC in Fig. 4.5b). Due to the oscillatory behavior over z-coordinate, the generation of the plasmonic mode is affected destructively by the interference resulting in the reduction of the effective nonlinearity.

In the case of SPP-enhanced SPDC, the increase of the beam width did not provide any additional increase in the yield of SPDC. However, in this case, the beam width is really important as the coherent buildup distance is large. Increasing the beam width up to $w_0 = 10\,\mathrm{cm}$ allows longer coherent buildup and boosts the yield of SPDC up to $0.3 \cdot 10^{-12}$, which is already comparable to the usual SPDC generation form a thick nonlinear crystal.

4.3.3 GDWs-enhanced SPDC

Another very promising type of resonant modes are GDWs (see Sec. 2.2.3). The structure for the GDW-enhanced SPDC is shown in Fig. 4.8a. It is very similar to the structure supporting LRSPPs (Fig. 4.6a), only the metal film is replaced with a dielectric waveguiding layer with refractive index $n_w = 2.2$. Such structure is interesting, as it displays high field enhancement like LRSPPs, however, it contains no metal layers and thus is completely free of absorption losses.

The summary of the results is shown in table 4.1. The calculated yield of SPDC is slightly higher than the yield of LRSPP-enhanced SPDC. Again, this effect is not caused by the increase of the enhancement, as the enhancement factor is around two times smaller than in the case of LRSPPs. The field

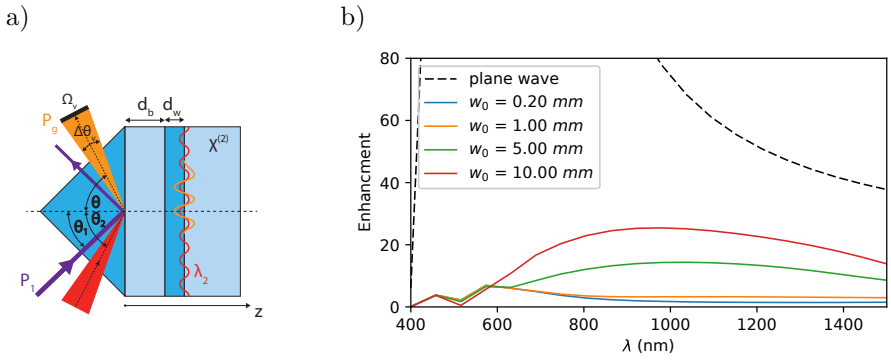

Figure 4.8: a) The structure for the modeling of GDW-enhanced SPDC: high refractive index prism, buffer layer, waveguide layer and nonlinear crystal. The pump laser (power P_1) is incident through the prism at an angle of incidence θ_1. The artificial vacuum fluctuations are incident at angle θ_2 and the generated SPDC signal (power P_g) is detected at angle θ by a sensor (solid angle Ω_v and angular span $\Delta\theta_v$). b) The dependence of field enhancement of GDWs on the wavelength and the waist size of the exciting Gaussian beam. [IV]

enhancement of GDWs is shown in Fig. 4.8b: the plane wave approximation does not hold again.

One of the benefits of GDWs is the all-dielectric structure, which leads to 100 % out-coupling efficiency, as the absorption of the generated SPDC signal is not possible. Also, the coherent buildup distance is long and allows to boost the yield of SPDC up to $0.08 \cdot 10^{-12}$.

On the negative side, the effective nonlinearity is only 10 % of its maximum value due to the oscillatory behavior of nonlinear polarization leading to destructive interference like in the case of LRSPPs.

4.4 Conclusions

In this chapter the enhancement of SPDC by three different structures supporting resonant surface waves were realistically modeled. In the case of SPP-enhanced SPDC, it was discovered, that indeed, the enhancement of SPDC by surface waves really work as expected (up to 10^4 times), however, the enhancement is only realistically available in the case of miniature sources (propagation distance up to 64 μm). In the case of larger propagation distance, the coherent buildup of the SPDC signal is strongly limited by the losses of the SPP mode.

Modeling also explains the results of the experimental work in Sec. 3.3, where no enhanced SPDC was detected and the upper limit of the yield of the SPP-enhanced SPDC was estimated to be $6 \cdot 10^{-14}$. It matches the calculations in table 4.1, as the estimated yield of SPDC is only up to $9 \cdot 10^{-16}$ (under optimal conditions) – the estimated yield of SPDC is considerably lower than the minimum experimentally detectable yield and no detection of SPP-enhanced SPDC is possible.

Next, the LRSPPs and GDWs were studied in the context of enhanced SPDC. The main difference in comparison to SPPs is the low propagation loss. Indeed, the short coherent buildup distance, the main limiting factor in the case of SPP-enhanced SPDC, is no longer a problem – coherent buildup happens efficiently for several millimeters and the yield of SPDC up to $0.3 \cdot 10^{-12}$ is achievable. On the negative side, also new limiting factors arise. Firstly, the enhancement factor is limited by the very narrow resonances of the LRSPPs and GDWs and secondly, the effective nonlinearity is reduced by the inefficient interaction with the nonlinear medium.

We see the greatest potential in SPP-enhanced SPDC in order to increase the efficiency of miniature SPDC sources.

5 Leaky Dyakonov SPPs for SPDC (publication V)

5.1 Introduction

The structure of SPP-enhanced SPDC (see Fig. 4.3a) is the simplest of the three studied in chapter 4 in the context of the experimental realization. It consists of a high refractive index prism, thin metal film and a nonlinear crystal. Still, one of the experimental challenges is to fabricate such structure.

One possibility is to take a nonlinear crystal, deposit a metal film on it and then attach a prism with an IML (realized in Sec. 3.3). However, the selection of nonlinear crystals are quite limited as a low refractive index is required – it is only possible to excite SPPs if the refractive index of the prism is substantially higher than the refractive index of the crystal. Moreover, commercially available IMLs are limited to the refractive index below 1.8 and they are often hazardous and difficult to handle. Another problem here is the photostability of IMLs.

The other possibility to fabricate the structure in Fig. 4.3a is to take a prism and deposit both a metal and a nonlinear medium on it. In such case, no use of IMLs are required. The only problem here is the deposition of properly oriented second-order nonlinear medium on the metal film. The fabrication of such layers via deposition has been investigated by many research groups with great progress: large second-order susceptibilities were registered for Si_3N_4, ZnO and SiO films [96–99]. However, all of them display very high refractive index (> 2 in the visible spectral region), which greatly limits the selection of the prisms.

Alternative setup is studied in this chapter: a new type of surface waves will be presented that have built-in excitation method and do not require Kretschmann prism to be excited. We have carefully studied the combination of SPPs and Dyakonov waves at the interface of a metal and uniaxial anisotropic crystal. Surface waves at the interface of the isotropic and anisotropic crystal have been studied before, however, always an excitation scheme similar to the Kretschmann configuration has been required. In Ref. V we showed, that it is not always the case: under special conditions, the DSPPs at the interface of a metal and anisotropic crystal becomes leaky (LDSPPs), which allows exciting DSPPs without any excitation scheme.

This chapter will begin with a short overview of methods that were used to study LDSPPs. Next, the main results and the possibility to use LDSPPs for the enhancement of SPDC will be outlined.

5.2 Methods

5.2.1 Complex root finder

The dispersion relationship of DSPPs (Eq. 2.60) is given in an implicit form and the task of finding complex propagation constants is not trivial, especially, if several closely spaced roots exist. Often iterative optimization routines (e.g. Newton–Raphson method) are employed to find the roots of complex functions, however, such methods inherently require initial estimates of the zeros and are unreliable in a sense that some zeros may remain undiscovered [100]. In this work, a superior method, based on Cauchy's theorem, is used, which is able to reliably find all zeros of a complex analytic function without any iterative optimization.

The method, used in this work, is described in depth in Ref. [101] and here only a short review is presented. The method relies on Cauchy's theorem that in the case of complex analytic function $f(z)$ with complex argument z, the contour integration around the closed region in the complex plane of z satisfies the relation

$$s_N = \frac{1}{2\pi i} \oint_C z^N \frac{f'(z)}{f(z)} dz = \sum_{i=1}^{\nu} z_i^N, \tag{5.1}$$

where z_i $(i = 1, 2 \ldots \nu)$ are zeros inside the region surrounded by the contour C and $N = 0, 1, \ldots$ is arbitrary number. If $N = 0$, then the integration

$$s_0 = \frac{1}{2\pi i} \oint_C \frac{f'(z)}{f(z)} dz = \nu \tag{5.2}$$

will give the number of zeros ν surrounded by the contour C as a result. Also, if only one zero is present in the region ($\nu = 1$), then it is possible to determine the zero z_1 just by integration of Eq. 5.1 by taking $N = 1$

$$s_1 = \frac{1}{2\pi i} \oint_C z \frac{f'(z)}{f(z)} dz = z_1. \tag{5.3}$$

Similarly, if two zeros are present in the region, we have a system of equations

$$\begin{cases} s_1 = z_1 + z_2 \\ s_2 = z_1^2 + z_2^2 \end{cases}, \tag{5.4}$$

which could be combined into polynomial respect to one of the solutions

$$2z_1^2 - 2s_1 z_1 + s_1^2 - s_2 = 0 \tag{5.5}$$

and be easily solved. Similarly, it is possible to compose a polynomial if the number of zeros inside the contour is higher, however, due to numerical inaccuracies, the optimal strategy is the following:

1. Evaluate the number of zeros $\nu = s_0$ in the initial region. If the number is small, then continue with step 3. If not, do step 2.
2. Divide the region on the complex plane to four smaller subregions and recursively do step 1 for each.
3. Evaluate integrals $s_1 \dots s_N$ and compose a polynomial. Solve the polynomial with standard methods to find zeros $z_1 \dots z_\nu$.
4. (Optional) Use Newton-Raphson method to fine-tune solutions for maximum accuracy.

Such method has proven to be reliable and fast to solve any dispersion relationship given in implicit form. The main requirement of the method is the knowledge of the first derivative $f'(z)$ in addition to the function itself.

5.2.2 Anisotropic TMM

In Sec. 4.2.1 a standard TMM was described for solving electromagnetic fields in stratified structures, where each layer is described by a thickness and a complex refractive index. However, a standard TMM is not sufficient to study DSPPs as Dyakonov waves relay on the anisotropy of a refractive index. For the inclusion of anisotropic optical mediums, another variation of TMM has been developed [28, 102–104].

In this work, the formalism developed by I. J. Hodgkinson, et. al. (Ref. [28]) is used. The main differences in comparison to a standard TMM are the requirement of full dielectric permittivity tensor for every layer and the coupling of polarizations. Here we only give a general description of the method, all details are described in Ref. [28].

As already described in Sec. 2.1.2.3, only three components of the dielectric permittivity tensor are truly independent. Together with two rotational angles of the principal axes in relation to the laboratory axes, the full dielectric tensor is specified. So four extra parameters are available in comparison to the isotropic case.

Also, in the case of a standard TMM, two orthogonal polarizations were totally independent (Sec. 2.1.2.2) and the propagation through the structure could be solved separately. It is not so in anisotropic mediums, which, in general, alter the polarization of the input beam. As a consequence, the solution in the case of anisotropic mediums consists of four plane wave components: two orthogonally polarized modes in the forward direction and another two in the backward direction. Also, the transfer and the propagation matrices are now with size 4×4. To find the orthogonal polarizations inside the anisotropic

crystal, an eigenequation is solved: eigenvectors correspond to the basis fields of orthogonal modes and eigenvalues are connected to the mode's effective refractive indices.

Although the technical details of anisotropic TMM are quite different (not presented here), the method still essentially uses the same matrix formalism to conveniently transfer fields between layers and propagate fields within the layer to fully solve electromagnetic fields inside the structure.

The method described in Ref. [28] is implemented in C++ for maximum performance and is available as an easy to use Python library. The code is open-source, documented and readily available at `github.com/ardiloot/GeneralTmm`.

5.3 Results

5.3.1 Leaky Dyakonov SPPs (LDSPPs)

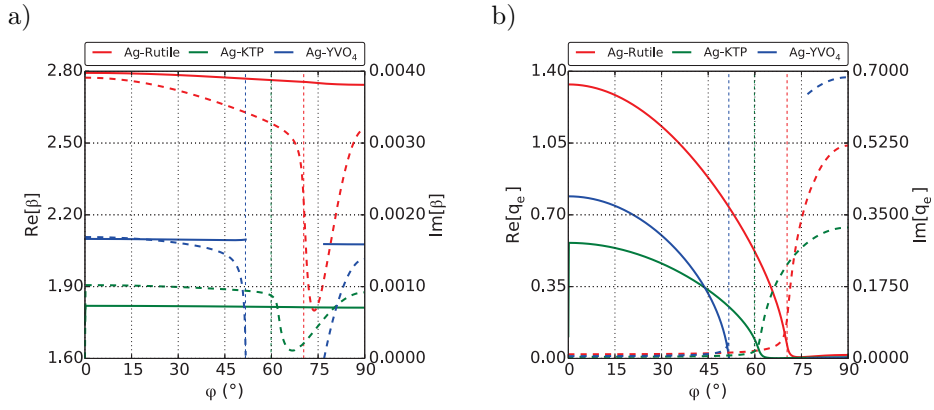

Figure 5.1: The dependence of the propagation constant (a) and the extraordinary decay factor (b) on the orientation of the OA for several interfaces. [V]

In Ref. [71] DSPPs were studied by solving the dispersion relationship of the interface of a metal and anisotropic crystal. It was found that DSPPs exist only for a limited range of the orientation of OA $\varphi < \varphi_c$ (critical angle given by Eq. 2.62). Here we study a possibility, that DSPPs become (half) leaky after critical angle ($\varphi > \varphi_c$) instead of experiencing cutoff.

To do that, the properties of DSPPs were also studied by solving the dispersion relationship (Eq. 2.60) by the method described in Sec. 5.2.1. The results (only propagation constant β and extraordinary decay constant q_e) for several interfaces are shown in Figs. 5.1a and 5.1b. Vertical colored lines represent critical angles defined by Eq. 2.62, essentially defined by condition $q_e = 0$.

Note, that here the similar notation is used as in Sec. 2.2.4: propagation and decay constants are scaled by the vacuum wave number.

Indeed, solutions exist for Ag-rutile and Ag-KTP interface even after the critical angle, the real part of the propagation constant remains unchanged and the imaginary part displays a minimum (see Fig. 5.1a). From Fig. 5.1b it is clear, that indeed DSPPs become leaky after the critical angle as the decay constant of the extraordinary wave becomes purely imaginary (corresponds to propagating wave). Interestingly, the other three waves associated with the DSPP mode remain evanescent (not shown here).

To sum up, from the analysis of the dispersion relationship of DSPPs we have found, that after the critical angle, the DSPP mode becomes leaky instead of experiencing cutoff. Those LDSPPs display very interesting field properties as only one of the four waves (extraordinary) is leaky, the other three remain bound to the interface.

5.3.2 LDSPPs in Kretschmann configuration

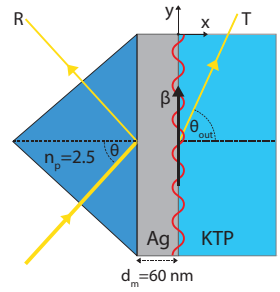

Figure 5.2: LDSPPs in Kretschmann configuration: a high refractive index prism, thin silver film and KTP anisotropic crystal. [V]

The defining property of surface waves is that the fields of the mode are bounded to the surface. In other words, the fields have maximums at the interface. A valid question is if it is justified to name LDSPPs to surface waves, as one of the components of the wave is not bounded to the surface. To answer this question, LDSPPs were studied in Kretschmann configuration by anisotropic TMM.

The structure under investigation is shown in Fig. 5.2. It consists of high refractive index ZnSe prism ($n_p = 2.5$), a silver film with thickness $d_m = 60\,\text{nm}$ and KTP crystal as an anisotropic medium [105, 106]. In Fig. 5.3a the reflection R_{pp} ("pp" means p-polarized excitation and p-polarized detection) dependence on the angle of incidence θ and on the angle of the OA φ is calculated at wavelength $\lambda = 900\,\text{nm}$. A clear minimum in the reflection curve is present for every orientation of the OA, corresponding to the excitation

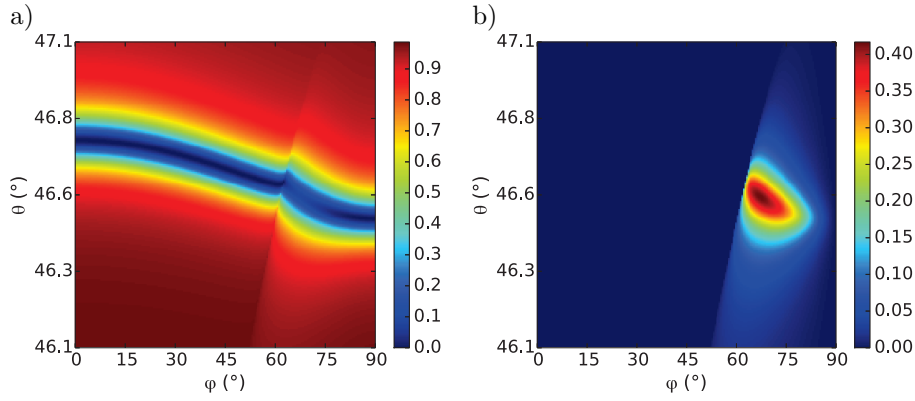

Figure 5.3: The reflection R_{pp} (a) and transmission T_{pe} (b) coefficient dependence on the orientation of the OA φ and on the angle of incidence θ for the structure in Fig. 5.2 at the wavelength 900 nm. The "pp" in the subscript means p-polarized excitation and p-polarized detection and similarly "pe" means p-polarized excitation and the detection of extraordinary polarization. [V]

of surface waves, even after the critical angle ($\varphi_c \approx 60°$). It supports the idea that the DSPP mode does not experience cutoff after the critical angle.

The transmission coefficient of the extraordinary mode T_{pe} is displayed in Fig. 5.3b. At small angles of the OA ($\varphi < \varphi_c$) the transmission coefficient is zero as expected – the DSPP mode is bounded to the interface. However, after the critical angle ($\varphi > \varphi_c$) the structure exhibits extraordinary transmission up to 40 %, while the transmission of the 60 nm thick silver film is only around 0.5 %. This effect is explained by a fact that the extraordinary component of LDSPPs is leaky. The incident light is effectively used to excite LDSPPs, which leak into the anisotropic crystal through the extraordinary component.

In Fig. 5.4a the effect of the orientation of the OA is studied at the fixed angle of incidence $\theta = 46.552°$. It is visible that only the extraordinary component of the mode becomes leaky. Perhaps the most interesting is the distribution of electrical fields of LDSPPs ($\varphi = 66.411°$, black vertical line in Fig. 5.4a) shown in Fig. 5.4b. The electrical fields of LDSPPs are indeed bounded to the interface of the metal and the crystal – the fields have a maximum at the interface and decay with distance from it. Interestingly, the z-component of the electrical field starts to increase with the distance from the interface while the x- and y-component decay to zero. Essentially it means, that the extraordinary component is almost fully s-polarized opposite to the exciting light.

To sum up, the electrical field distribution of LDSPPs (Fig. 5.4a) shows, that the main surface wave properties remain even after the critical angle – the fields have a maximum at the interface and decay with a distance from it.

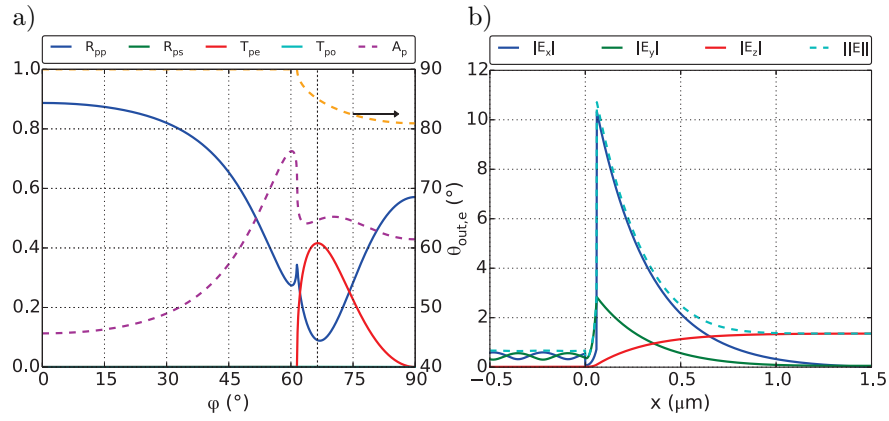

Figure 5.4: a) The reflection, transmission and absorption coefficients dependence on the orientation of the OA φ at a fixed angle of incidence $\theta = 46.552°$. b) The electrical field distribution of LDSPPs at $\theta = 46.552°$ and $\varphi = 66.411°$ (vertical line in Fig. 5.4a). [V]

In addition to usual surface wave, there is a leaky extraordinary component inside the anisotropic crystal that in this case is almost fully s-polarized.

5.3.3 Alternative excitation scheme

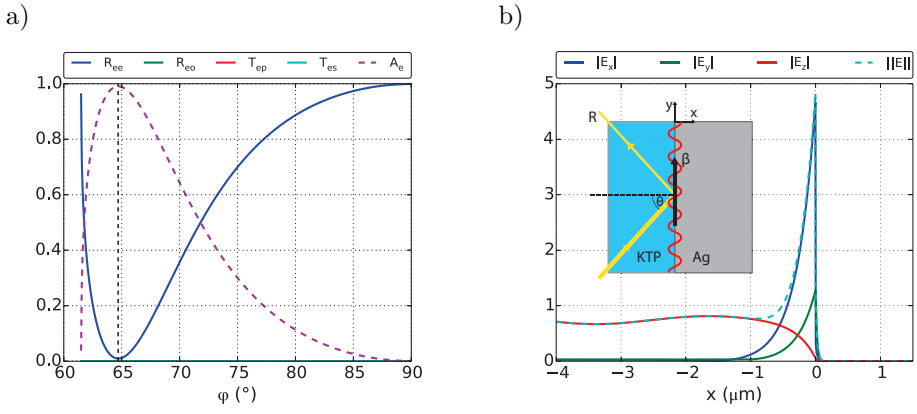

Figure 5.5: a) The reflection, transmission and absorption coefficients for a fixed angle of incidence ($\beta = 1.815$). b) The electrical field distribution at $\beta = 1.815$ and $\varphi = 66.694°$ (vertical line in Fig. 5.5a). [V]

To excite traditional surface waves, there is always need for some kind of excitation setup (e.g. Kretschmann scheme). Essentially, the task of excitation setup is to make surface waves leaky and to use it to channel energy into the

surface mode. In the case of LDSPPs, one component of the mode is already leaky – it is possible to excite LDSPPs without any excitation scheme. In other words, we explore the possibility to reverse the extraordinary transmission in Fig. 5.3b to excite the surface wave.

To study it, we modeled the simple two-layer structure (essentially the reversed structure in Fig. 5.2 without the prism) in the inset of Fig. 5.5b with anisotropic TMM. In Fig. 5.5a the reflection, transmission and absorption coefficients are shown for a fixed angle of incidence ($\beta = 1.815$). From the reflection curve of the extraordinary wave (R_{ee}), it turns out, that it is indeed possible to directly excite LDSPPs. The reflection curve reaches zero and all of the energy of the light is transferred to the surface waves and finally, all of the energy is absorbed. In other words, such kind of very simple two-layer excitation scheme is also 100 % effective.

The electrical field distribution ($\varphi = 66.694°$) is shown in Fig. 5.5b. Again, the field distribution has the characteristics of the surface wave: fields have maximums at the interface and decay with a distance from it.

5.3.4 LDSPPs for SPDC

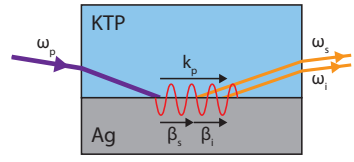

Figure 5.6: The schematic of the experiment of LDSPP-enhanced SPDC. [V]

Previously we have shown, that a new kind of surface wave exists at the interface of a metal and anisotropic crystal – LDSPPs. Moreover, LDSPPs display interesting properties, one component of the four is leaky that enables to excite the surface mode without any excitation scheme – the method for excitation is already built-in. In this section, we explore the possibility to use LDSPPs for the enhancement of SPDC.

As already discussed in the introduction, one of the main experimental challenges of SPP-enhanced SPDC is the fabrication of the structure. One strategy requires the use of IMLs that have limited range of refractive indices and are not photostable. The other strategy relies on the deposition of properly oriented nonlinear material on top of the metal film, which is still an experimental challenge.

One way to overcome the complexities of the fabrication is to use the LDSPPs, as the excitation method is built-in into LDSPPs, there is no need for the Kretschmann prism or any other excitation method. The schematic for the LDSPP-enhanced SPDC is shown in Fig. 5.6. It only consists of anisotropic

crystal with appropriate nonlinearities (KTP in this case) and a metal layer (silver in this case). Under the proper angle of incidence of the pump beam, it is possible that due to nonlinear interaction with the material pump photons split into two quanta of LDSPPs (denoted by β_s and β_i). After propagation of a short distance, the generated signal and idler modes leak back to the crystal as photons.

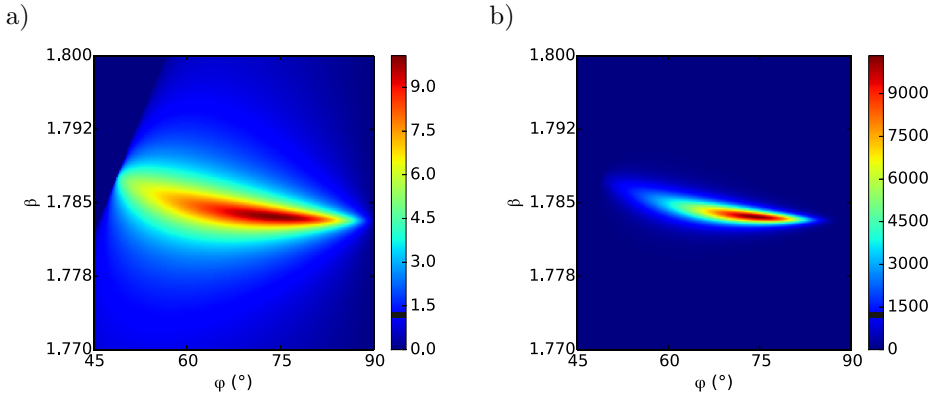

Figure 5.7: a) The maximum enhancement of the LDSPP mode. b) The enhancement factor of SPDC. [V]

The mechanism of the enhanced SPDC is completely analogous to the SPP-enhanced SPDC presented in chapter 3. To quantify the possible enhancements, field enhancement factors were calculated as in chapter 3 and are shown in Fig. 5.7 for pump wavelength $\lambda = 540\,\mathrm{nm}$ in the case of equal splitting. The maximum enhancement of the LDSPP mode is around nine times in the case of proper alignment (Fig. 5.7a). Taking into account that we are again interested in the "fpp" process then the total enhancement factor of SPDC becomes around 9000 (shown in Fig. 5.7b). It is however reduced by the weakening of the pump beam due to the metal surface and the final enhancement factor of the SPDC in this structure is estimated to be around $\Upsilon \approx 240$ times.

5.4 Conclusions

In this chapter, the dispersion relationship of DSPPs was carefully studied and half-leaky mode was discovered. The properties of LDSPPs were studied in the usual Kretschmann configuration with anisotropic TMM and extraordinary transmission was demonstrated. Next, the half-leaky properties of LDSPPs were investigated as an alternative excitation method without any coupling prism. It was demonstrated, that indeed, LDSPPs could be excited by the leaky component – LDSPPs have built-in excitation method.

The built-in excitation method was studied to simplify the experimental realization of the enhanced SPDC by surface waves. It was demonstrated, that indeed, LDSPPs could be used to enhance SPDC and simplify the experimental realization – a nonlinear crystal with a high refractive index could be used and no coupling prism is required.

Future work

The plasmonic and dielectric structures in chapter 4 were fully modeled for enhancing SPDC. The obvious future work here is the continuation of the experimental realization and the verification of the predicted enhancements of SPDC. In addition, also the optimization of the plasmonic and dielectric structures for maximally enhanced SPDC was out of the scope of this work. This work only shows that the optimal structure is somewhere between SPPs and LRSPPs (or GDWs): SPP-enhanced SPDC displays a high enhancement factor but low coherent buildup length and vice versa in the case of LRSPP- and GDW-enhanced SPDC. Also, the reduction in the effective nonlinearity should be studied further in the case of LRSPPs and GDWs, as by careful design of the nonlinear layers, a full nonlinearity could be available.

In the case of LDSPPs (chapter 5), the experimental verification of the predicted results was also out of the scope of this work. Moreover, no full modeling of the LDSPP-enhanced SPDC was conducted as in chapter 4. It requires a generalization of the methods developed in Sec. 4.2 for anisotropic mediums and it is left as a topic for a future study.

Furthermore, only the case of low excitation intensity was considered in this thesis and the process of SPDC was considered in the framework of perturbation theory. However, in the case of field enhancement of resonant modes, higher-order effects may become important already for a moderate excitation power far less than the atomic field – strong-field effects are already important for a relatively weak laser excitation [107]. In Ref. [107] a non-perturbative theory of SPDC is developed for a metal-dielectric interface to study the strong-field effects. It is predicted, that the process is resonantly enhanced at the characteristic power of the excitation, typically of the order of tens of watts per square centimeter. One of the future tasks is to generalize the non-perturbative theory of SPDC for realistic structures and excitation conditions like in this study.

Summary

This thesis is devoted to experimentally and numerically study the possibilities to enhance the process of spontaneous parametric down-conversion (SPDC), one of the main sources of entangled photon pairs, by surface waves.

In the first original part of the thesis, the idea of surface plasmon polariton (SPP) enhanced SPDC is introduced. The idea was first explored theoretically and an enhancement factor of SPDC up to $4 \cdot 10^4$ was estimated by a simplistic model. Next, the idea of SPP-enhanced SPDC was studied experimentally in a custom-built goniometric setup, however, no SPP-enhanced SPDC signal was observed – the yield of SPDC must be lower than $6 \cdot 10^{-14}$. It is concluded, that a full modeling of SPP-enhanced SPDC is required in order to explain the experimental results.

The second original part of the thesis focuses on the full modeling of enhanced SPDC. The enhancement was considered by three type of surface waves: SPPs, long-range SPPs (LRSPPs) and guided dielectric waves (GDWs). To do that, methods to model SPDC in layered structures were developed as extensions to the standard transfer-matrix method (TMM). Firstly, an extension to model second-order nonlinear processes was developed. Secondly, a standard TMM was extended to include beams with realistic profiles (e.g. Gaussian) to replace infinite plane wave approximation, which breaks down for very narrow resonances. And finally, the process of SPDC was modeled as a limiting case of a classical difference-frequency generation.

In the case of SPP-enhanced SPDC, enhancement factor around 10^4 was predicted, however, the effect of enhancement is limited by the short coherent buildup distance ($\approx 64\,\mu$m) – the superior performance of SPP-enhanced SPDC is only available in miniature devices. To extend the coherent buildup distance, LRSPPs and GDWs were studied. Indeed, due to lower losses of both surface waves, the coherent buildup distance was extended up to several millimeters, which is comparable to the thicknesses of nonlinear crystals usually used for SPDC. However, the use of LRSPPs and GDWs also lead to additional limitations.

Firstly, the resonances of LRSPPs and GDWs are very narrow and the enhancement of vacuum fluctuation modes are strongly inhibited – only a small fraction of participating modes are enhanced. Also, the interaction of narrow resonances with a realistic Gaussian beam (waist size 1 mm) is weak. Together those two factors limit the field enhancement factor bellow 10^3, which is less than in the case of SPPs. It is possible to relieve the limitations by increasing the waist size of the pump beam. It allows enhancing the yield of SPDC up to

$0.3 \cdot 10^{-12}$, which is already comparable to a perfectly phase-matched SPDC from a nonlinear crystal in a conventional setup.

Secondly, the coherent buildup study revealed that only a fraction of the second-order susceptibility is effectively available due to oscillatory behavior of nonlinear polarization leading to a destructive interference. This could be avoided by a careful placement of nonlinear mediums, however, it is not within the scope of this work.

In the third original part of the thesis, Dyakonov SPPs (DSPPs) were investigated and conditions for the leaky nature of DSPPs was discovered. Leaky DSPPs (LDSPPs) have very interesting properties: only one of the four components of a mode is leaky and it could be used to excite LDSPPs without any extra coupling prism or similar. LDSPPs with built-in excitation method were studied to simplify the structure required for the experiments of SPP-enhanced SPDC.

Summary in Estonian

Spontaanse parameetrilise allamuundamise võimendamine pinnaplasmonite ja dielektriliste pinnalainetega

Käesoleva doktoritöö eesmärgiks on spontaanse parameetrilise allamuundamise (edaspidi allamuundamine) võimendamine pinnalainetega, et suurendada põimitud footonpaaride allika efektiivsust.

Töö esimene põhiosa keskendub allamuundamise võimendamisele pinnaplasmonitega. Esiteks viidi läbi esialgsed teoreetilised arvutused, arvestades vaid väljavõimendustega, ja ennustati protsessi võimendamist kuni $4 \cdot 10^4$ korda. Järgmiseks katsetati pinnaplasmonitega põimitud footonpaaride allika võimendamist eksperimentaalselt. Selleks disainiti ja ehitati goniomeetriline mõõtesüsteem ja viidi läbi esialgsed mõõtmised. Mõõtmiste käigus võimendatud signaali ei registreeritud ja footonpaaride allika maksimaalseks efektiivsuseks hinnati $6 \cdot 10^{-14}$. Et seletada saadud tulemusi, on vaja läbi viia detailne allamuundamise modelleerimine.

Töö teise põhiosa eesmärgiks on välja töötada arvutusmeetodid allamuundamise võimendamise uurimiseks. Selleks töötati välja mitu laiendust standardsele ülekandemaatriksi meetodile. Esiteks laiendati ülekandemaatriksi meetodit mittelineaarsetele protsessidele. Teiseks lisati funktsionaalsus realistliku kujuga valguskiirte (näiteks Gaussi kiir) kasutamiseks, sest lõpmatu tasalaine lähendus ei tööta väga kitsaste resonantside korral. Viimasena täiendati meetodit, et modelleerida allamuundamist kui vahesageduse genereerimise piirjuhtu.

Arvutused viidi läbi kolme eri tüüpi pinnalainetega: (tavalised) pinnaplasmonid (*surface plasmon polaritons*), pika levikukaugusega pinnaplasmonid (*long-range surface plamon polaritons*) ja dielektriliste moodidega (*guided dielectric waves*). Tavaliste pinnaplasmonitega allamuundamise võimendusteguriks hinnati taaskord kuni 10^4 korda, kuid leiti, et võimenduse avaldumist takistab lühike koherentse genereerimise pikkus ($\approx 64\,\mu$m) – võimendus avaldub reaalselt vaid miniatuurse footonpaaride allika korral. Koherentse genereerimise pikkuse suurendamiseks uuriti pika levikukaugusega pinnaplasmoneid ja dielektrilise moode. Tõepoolest, tänu madalatele kadudele, hinnati mõlema pinnalaine korral koherentse genereerimise pikkuseks rohkem kui mõned millimeetrid, mis footonpaaride genereerimisele takistusi ei sea, aga esile kerkisid ka uued võimendamist takistavad tegurid.

Esiteks on nii pika levikukaugusega pinnaplasmonid kui ka dielektrilised moodid väga kitsaste resonantsidega, mistõttu ainult väike osa osalevatest vaakumfluktuatsiooni moodidest on reaalselt võimendatud. Lisaks on nõrgendatud ka laserkiire ja pinnalainete vaheline interaktsioon, sest 1 mm läbimõõduga laserkiire nurkspekter on tunduvalt laiem kui antud pinnalainete resonantsid. Mõlema teguri koosmõjul väheneb võimendustegur alla tuhande, mis on vähem kui tavaliste pinnaplasmonite korral. Kitsaste resonantside negatiivset mõju on võimalik vähendada, kui suurendada ergastava laseri kiire laiust. See võimaldab saavutada allamuundamise efektiivsuseks kuni $0.3 \cdot 10^{-12}$.

Teiseks takistavaks teguriks on materjali mittelineaarsuse ebaefektiivne kasutamine. Arvutused näitavad, et nii pika levikukaugusega pinnaplasmonid kui ka dielektrilised moodid kasutavad vaid väikest osa materjali mittelineaarsusest. See tuleneb mittelineaarse polarisatsiooni ostsileerimisest mittelineaarses keskkonnas ja põhjustab genereeritava signaali vähenemist läbi destruktiivse interferentsi. Töös on välja toodud, et seda on võimalik vältida mittelineaarsete keskkondade hoolika paigutamisega, kuid täpsed arvutused pole antud töö teemaks.

Viimane töö põhiosa keskendub Dyakonovi pinnaplasmonite uurimisele allamuundamise kontekstis. Peatükk algab Dyakonovi pinnalainete dispersiooniseose uurimisega ja näidatakse, et teadud tingimustel pole üks neljast Dyakonovi pinnaplasmonite komponendist enam pinnaga seotud. See huvitav omadus võimaldab ergastada Dyakonovi pinnaplasmoneid ilma ühegi prisma või muu ergastusskeemita. Seda uudset ergastusskeemi uuritakse allamuundamise võimendamise kontekstis, et lihtsustada nõutud eksperimendiskeemi.

Acknowledgments

First and foremost I would like to thank my supervisor Vladimir Hizhnyakov for a really interesting topic for the Ph.D. studies, for invaluable contributions to the publications and for a continuous support and help. I appreciate all his contributions of time, ideas, and funding. Also, I would like to thank my other supervisors Valter Kiisk and Ilmo Sildos for their assistance with experimental work, for their encouragement and for their insightful comments. Special thanks go for Tavo Romann, Aarne Kasikov and Mikk Vahtrus for the collaboration on the experimental work. I am also grateful to all my colleagues and fellow students for interesting collaborations and for stimulating discussions.

This dissertation was supported by the Estonian research projects IUT2-27, IUT34-27, ETF9283 and the European Union through the European Regional Development Fund (project 3.2.0101.11-0029) and through the ERA.Net Rusplus project "88 DIABASE".

Bibliography

[1] P. Kwiat, E. Waks and A. White, "Ultrabright source of polarization-entangled photons," *Physical Review A*, 60(2), pp. 773–776, 1999.

[2] P. Kwiat, K. Mattle, H. Weinfurter, A. Zeilinger, A. Sergienko and Y. Shih, "New high-intensity source of polarization-entangled photon pairs." *Physical review letters*, 75(24), pp. 4337–4341, 1995.

[3] M. Oberparleiter and H. Weinfurter, "Cavity-enhanced generation of polarization-entangled photon pairs," *Optics Communications*, 183(1), pp. 133–137, 2000.

[4] Y. Jeronimo-Moreno, S. Rodriguez-Benavides and A. B. U'Ren, "Theory of cavity-enhanced spontaneous parametric downconversion," *Laser Physics*, 20(5), pp. 1221–1233, 2010.

[5] Y. J. Lu and Z. Y. Ou, "Optical parametric oscillator far below threshold: Experiment versus theory," *Physical Review A - Atomic, Molecular, and Optical Physics*, 62(3), p. 11, 2000.

[6] P. Hariharan and B. C. Sanders, "Cavity-enhanced parametric down-conversion as a source of correlated photons," *Journal of Modern Optics*, 47(10), pp. 1739–1744, 2000.

[7] Z. Y. Ou and Y. J. Lu, "Cavity Enhanced Spontaneous Parametric Down-Conversion for the Prolongation of Correlation Time between Conjugate Photons," *Physical Review Letters*, 83(13), pp. 2556–2559, 1999.

[8] P. Thomas, M. Dunn, D. Stothard, D. Walsh and C. Chunnilall, "A pump enhanced source of telecom-band correlated photon pairs," *Journal of Modern Optics*, 58(8), pp. 631–639, 2011.

[9] S. Tanzilli, H. De Riedmatten, W. Tittel, H. Zbinden, P. Baldi, M. De Micheli, D. Ostrowsky and N. Gisin, "Highly efficient photon-pair source using periodically poled lithium niobate waveguide," *Electronics Letters*, 37(1), p. 26, 2001.

[10] K. Sanaka, K. Kawahara and T. Kuga, "New high-efficiency source of photon pairs for engineering quantum entanglement," *Physical Review Letters*, 86(24), pp. 5620–5623, 2001.

[11] K. Banaszek, a. B. U'ren and I. a. Walmsley, "Generation of correlated photons in controlled spatial modes by downconversion in nonlinear waveguides." *Optics letters*, 26(17), pp. 1367–1369, 2001.

[12] S. Tanzilli, W. Tittel, H. De Riedmatten, H. Zbinden, P. Baldi, M. Demicheli, D. B. Ostrowsky and N. Gisin, "PPLN waveguide for quantum communication," *European Physical Journal D*, 18(2), pp. 155–160, 2002.

[13] E. J. Mason, M. a. Albota, F. König and F. N. C. Wong, "Efficient generation of tunable photon pairs at 0.8 and 1.6 microm." *Optics letters*, 27(23), pp. 2115–7, 2002.

[14] A. Yoshizawa and H. Tsuchida, "Generation of polarization-entangled photon pairs in 1550 nm band by a fiber-optic two-photon interferometer," *Applied Physics Letters*, 85(13), pp. 2457–2459, 2004.

[15] Y.-k. Jiang and A. Tomita, "Highly efficient polarization-entangled photon source using periodically poled lithium niobate waveguides," *Optics Communications*, 267(1), pp. 278–281, 2006.

[16] S. M. Spillane, M. Fiorentino and R. G. Beausoleil, "Spontaneous parametric down conversion in a nanophotonic waveguide," *Optics Express*, 15(14), p. 8770, 2007.

[17] M. Bock, A. Lenhard, C. Chunnilall and C. Becher, "Highly efficient heralded single-photon source for telecom wavelengths based on a PPLN waveguide," *Optics Express*, 24(21), p. 23992, 2016.

[18] B.-S. Shi and A. Tomita, "Highly efficient generation of pulsed photon pairs with bulk periodically poled potassium titanyl phosphate," *Journal Oprical Society of America B*, 21(12), pp. 2081–2084, 2004.

[19] A. Vamivakas, B. Saleh, A. Sergienko and M. Teich, "Theory of spontaneous parametric down-conversion from photonic crystals," *Physical Review A*, 70(4), pp. 1–7, 2004.

[20] M. Centini, J. Peřina, L. Sciscione, C. Sibilia, M. Scalora, M. J. Bloemer and M. Bertolotti, "Entangled photon pair generation by spontaneous parametric down-conversion in finite-length one-dimensional photonic crystals," *Physical Review A - Atomic, Molecular, and Optical Physics*, 72(3), pp. 1–11, 2005.

[21] S. Wei, Y. Dong, H. Wang and X. Zhang, "Enhancement of correlated photon-pair generation from a positive-negative index material heterostructure," *Physical Review A - Atomic, Molecular, and Optical Physics*, 81(5), 2010.

[22] R. Horn, P. Abolghasem, B. J. Bijlani, D. Kang, A. S. Helmy and G. Weihs, "Monolithic Source of Photon Pairs," 153605(April), pp. 1–5, 2012.

[23] A. Vallés, M. Hendrych, J. Svozilík, R. Machulka, P. Abolghasem, D. Kang, B. J. Bijlani, A. S. Helmy and J. P. Torres, "Generation of

polarization-entangled photon pairs in a Bragg reflection waveguide," *Optics Express*, 21(9), p. 10841, 2013.

[24] N. B. Grosse, J. Heckmann and U. Woggon, "Nonlinear Plasmon-Photon Interaction Resolved by k-Space Spectroscopy," *Physical Review Letters*, 108(136802), pp. 1–5, 2012.

[25] J. Heckmann, M.-E. Kleemann, N. B. Grosse and U. Woggon, "The dual annihilation of a surface plasmon and a photon by virtue of a three-wave mixing interaction." *Optics express*, 21(23), pp. 28856–61, 2013.

[26] L. Novotny and B. Hecht, Principles of Nano-Optics, Cambridge University Press, 2006.

[27] M. Born and E. Wolf, Principles of optics, Cambridge University Press, 1999.

[28] I. Hodgkinson, S. Kassam and Q. Wu, "Eigenequations and Compact Algorithms for Bulk and Layered Anisotropic Optical Media: Reflection and Refraction at a Crystal-Crystal Interface," *Journal of Computational Physics*, 133(1), pp. 75–83, 1997.

[29] R. W. Boyd, Nonlinear Optics, Academic Press, San Diego, 3rd edition, 2008.

[30] H. Raether, Surface Plasmons on Smooth and Rough Surfaces and on Gratings, Springer, 1988.

[31] S. Maier, Plasmonics : Fundamentals and Applications, Springer, 2004.

[32] S. Hayashi and T. Okamoto, "Plasmonics: visit the past to know the future," *Journal of Physics D: Applied Physics*, 45(43), p. 433001, 2012.

[33] Y. Wang, E. W. Plummer and K. Kempa, "Foundations of Plasmonics," *Advances in Physics*, 60, pp. 799–898, 2011.

[34] J. Lakowicz, "Radiative decay engineering 3. Surface plasmon-coupled directional emission," *Analytical Biochemistry*, 324, pp. 153–169, 2004.

[35] H. Boersch, J. Geiger, A. Imbusch and N. Niedrig, "High resolution investigation of the energy losses of 30 keV electrons in aluminum foils of various thicknesses," *Physics Letters*, 22(2), pp. 146–147, 1966.

[36] J. B. Swan, A. Otto and H. Fellenzer, "Observed Retardation Effects on the Energy of the $\omega+$-Surface Plasmons in Thin Aluminium Foils," *physica status solidi (b)*, 23(1), pp. 171–176, 1967.

[37] E. Kretschmann and H. Raether, "Radiative Decay of Non Radiative Surface Plasmons Excited by Light," *Zeitschrift für Naturforschung*, 23, pp. 2135–2136, 1968.

[38] P. B. Johnson and R. W. Christy, "Optical Constants of the Noble Metals," *Physical Review B*, 6(12), pp. 4370–4379, 1972.

[39] G. Ghosh, "Dispersion-equation coefficients for the refractive index and birefringence of calcite and quartz crystals," *Optics Communications*, 163(1-3), pp. 95–102, 1999.

[40] B. Liedberg, C. Nylander and I. Lundström, "Biosensing with surface plasmon resonance–how it all started." *Biosensors & bioelectronics*, 10, pp. i–ix, 1995.

[41] J. Homola, S. S. Yee and G. Gauglitz, "Surface plasmon resonance sensors: review," *Sensors and Actuators B*, 54, pp. 3–15, 1999.

[42] W. Barnes, A. Dereux and T. Ebbesen, "Surface plasmon subwavelength optics," *Nature*, 424(August), pp. 824–831, 2003.

[43] D. K. Gramotnev and S. I. Bozhevolnyi, "Plasmonics beyond the diffraction limit," *Nature Photonics*, 4(2), pp. 83–91, 2010.

[44] M. Stockman, "Nanofocusing of Optical Energy in Tapered Plasmonic Waveguides," *Physical Review Letters*, 93(13), p. 137404, 2004.

[45] M. Bauch, K. Toma, M. Toma, Q. Zhang and J. Dostalek, "Plasmon-Enhanced Fluorescence Biosensors: A Review," *Plasmonics*, 9(4), pp. 781–799, 2014.

[46] P. Törmä and W. L. Barnes, "Strong coupling between surface plasmon polaritons and emitters," *Reports on Progress in Physics*, 78, p. 013901, 2015.

[47] M. Kauranen and A. V. Zayats, "Nonlinear plasmonics," *Nature Photonics*, 6(October), pp. 737–748, 2012.

[48] H. J. Simon, D. E. Mitchell and J. G. Watson, "Optical Second-Harmonic Generation with Surface Plasmons in Silver Films," *Physical Review Letters*, 33(26), pp. 1531–1534, 1974.

[49] H. Simon, R. Benner and J. Rako, "Optical second harmonic generation with surface plasmons in piezoelectric crystals," *Optics Communications*, 23(2), pp. 245–248, 1977.

[50] D. Sarid, "Long-range surface-plasma waves on very thin metal films," *Physical Review Letters*, 47(26), pp. 1927–1930, 1981.

[51] J. C. Quail, J. G. Rako and H. J. Simon, "Long-range surface-plasmon modes in silver and aluminum films," *Opt. Lett.*, 8(7), pp. 377–379, 1983.

[52] A. E. Craig, G. A. Olson and D. Sarid, "Experimental observation of the long-range surface-plasmon polariton," *Optics Letters*, 8(7), p. 380, 1983.

[53] P. Berini, "Long-range surface plasmon polaritons," *Advances in Optics and Photonics*, 1(3), p. 484, 2009.

[54] L. Wendler and R. Haupt, "Long-range surface plasmon-polaritons in asymmetric layer structures," *Journal of Applied Physics*, 59(9), pp. 3289–3291, 1986.

[55] G. I. Stegeman, J. J. Burke and D. G. Hall, "Nonlinear optics of long range surface plasmons," *Applied Physics Letters*, 41(10), pp. 906–908, 1982.

[56] R. T. Deck and D. Sarid, "Enhancement of second-harmonic generation by coupling to long-range surface plasmons," *J. Opt. Soc. Am.*, 72(12), pp. 1613–1617, 1982.

[57] J. Quail, J. Rako, H. Simon and R. Deck, "Optical second-harmonic generation with long-range surface plasmons," *Physical review letters*, 50(25), pp. 1987–1989, 1983.

[58] P. West, S. Ishii, G. Naik, N. Emani, V. Shalaev and a. Boltasseva, "Searching for better plasmonic materials," *Laser & Photonics Reviews*, 4(6), pp. 795–808, 2010.

[59] R. Sainidou, J. Renger, T. V. Teperik, M. U. Gonzalez, R. Quidant and F. J. Garcia de Abajo, "Extraordinary All-Dielectric Light Enhancement over Large Volumes," *Nano Letters*, 10(11), pp. 4450–4455, 2010.

[60] Y. Yang, I. I. Kravchenko, D. P. Briggs and J. Valentine, "High Quality Factor Fano-Resonant All-Dielectric Metamaterials," 4826(2011), 2014.

[61] P. Kapitanova, V. Ternovski, A. Miroshnichenko, N. Pavlov, P. Belov, Y. Kivshar and M. Tribelsky, "Giant field enhancement in high-index dielectric subwavelength particles," *Scientific Reports*, 7(1), pp. 1–8, 2017.

[62] S. Jahani and Z. Jacob, "All-dielectric metamaterials," *Nature Nanotechnology*, 11(1), pp. 23–36, 2016.

[63] A. E. Krasnok, A. E. Miroshnichenko, P. a. Belov and Y. S. Kivshar, "All-dielectric optical nanoantennas." *Optics express*, 20(18), pp. 20599–604, 2012.

[64] D. Marcuse, Light Transmission Optics, Van Nostrand Reinhold, 1982.

[65] M. D'yakonov, "New type of electromagnetic wave propagating at an interface," *Sov. Phys. JETP*, 67(4), pp. 714–716, 1988.

[66] O. Takayama, L. Crasovan, D. Artigas and L. Torner, "Observation of Dyakonov Surface Waves," *Physical Review Letters*, 102(4), p. 043903, 2009.

[67] O. Takayama, L.-C. Crasovan, S. K. Johansen, D. Mihalache, D. Artigas and L. Torner, "Dyakonov Surface Waves: A Review," *Electromagnetics*, 28(3), pp. 126–145, 2008.

[68] L. Torner, J. P. Torres and D. Mihalache, "New type of guided waves in birefringent media," *IEEE Photonics Technology Letters*, 5(2), pp. 201–203, 1993.

[69] L. Torner, J. P. Torres, C. Ojeda and D. Mihalache, "Hybrid waves guided by ultrathin films," *Journal of Lightwave Technology*, 13(10), pp. 2027–2033, 1995.

[70] Z. Jacob and E. E. Narimanov, "Optical hyperspace for plasmons: Dyakonov states in metamaterials," *Conference Proceedings - Lasers and Electro-Optics Society Annual Meeting-LEOS*, 221109(2008), pp. 563–564, 2009.

[71] R. Li, C. Cheng, F. F. Ren, J. Chen, Y. X. Fan, J. Ding and H. T. Wang, "Hybridized surface plasmon polaritons at an interface between a metal and a uniaxial crystal," *Applied Physics Letters*, 92(141115), pp. 1–3, 2008.

[72] O. Takayama, D. Artigas and L. Torner, "Practical dyakonons." *Optics letters*, 37(20), pp. 4311–3, 2012.

[73] A. Loot and V. Hizhnyakov, "Leaky Dyakonov surface plasmon polaritons for birefringent crystals," *Applied Physics A*, 122:327(4), pp. 1–8, 2016.

[74] V. G. Dmitriev, G. G. Gurzadyan and D. N. Nikogosyan, Handbook of optical nonlinear crystals, Springer, 1999.

[75] J. R. Devore, "Refractive Indices of Rutile and Sphalerite," 1951.

[76] S. E. Harris, K. K. Oshman and R. L. Byer, "Observation of Tunable Optical Parametric Fluorescence," *Physical Review Letters*, 18(18), pp. 732–734, 1967.

[77] D. N. Klyshko, "Coherent photon decay in a nonlinear medium," *JETP Letters*, 6(1), pp. 490–492, 1967.

[78] D. N. Klyshko, "Parametric luminescence of lithium niobate excited by an argon laser," *JETP Letters*, 6(23), 1968.

[79] D. N. Klyshko, Photons and Nonlinear Optics, Gordon and Breach Science Publishers, 1988.

[80] D. C. Burnham and D. L. Weinberg, "Observation of Simultaneity in Parametric Production of Optical Photon Pairs," *Physical Review Letters*, 25(2), pp. 84–87, 1970.

[81] P. G. Kwiat, P. H. Eberhard, A. M. Steinberg and R. Y. Chiao, "Proposal for a loophole-free Bell inequality experiment," *Physical Review A*, 49(5), pp. 3209–3220, 1994.

[82] L. Mandel and E. Wolf, Optical coherence and quantum optics, Cambridge University Press, 1995.

[83] C. Gerry and P. Knight, Introductory Quantum Optics, Cambridge University Press, Cambridge, 2004.

[84] D. A. Kleinman, "Theory of Optical Parametric Noise," *Physical Review*, 174(3), pp. 1027–1041, 1968.

[85] W. H. Louisell, A. Yariv and A. E. Siegman, "Quantum Fluctuations and Noise in Parametric Processes. I." *Physical Review*, 124(6), pp. 1646–1654, 1961.

[86] C. K. Hong and L. Mandel, "Theory of parametric frequency down conversion of light," *Physical Review A*, 31(4), pp. 2409–2418, 1985.

[87] D. Eimerl, L. Davis, S. Velsko, E. K. Graham and a. Zalkin, "Optical, mechanical, and thermal properties of barium borate," *Journal of Applied Physics*, 62(1987), pp. 1968–1983, 1987.

[88] D. Braun and A. Libchaber, "Computer-based photon-counting lock-in for phase detection at the shot-noise limit." *Optics letters*, 27(16), pp. 1418–1420, 2002.

[89] P. Clarkson, T. J. Esward, P. M. Harris, A. A. Smith and I. M. Smith, "Software simulation of a lock-in amplifier with application to the evaluation of uncertainties in real measuring systems," *Measurement Science and Technology*, 21(4), p. 045106, 2010.

[90] A. D. Rakic, A. B. Djurisic, J. M. Elazar and M. L. Majewski, "Optical properties of metallic films for vertical-cavity optoelectronic devices." *Applied optics*, 37(22), 1998.

[91] Y. Jiang, S. Pillai and M. A. Green, "Realistic Silver Optical Constants for Plasmonics," *Scientific Reports*, 6, pp. 1–7, 2016.

[92] F. Abeles, "Optical Properties of Thin Absorbing Films," *JOSA*, 47(6), pp. 473–482, 1957.

[93] O. S. Heavens, "Optical properties of thin films," *Reports on Progress in Physics*, 23(1), p. 301, 1960.

[94] J. Chilwell and I. Hodgkinson, "Thin-films field-transfer matrix theory of planar multilayer waveguides and reflection from prism-loaded waveguides," *J. Opt. Soc. Am.*, 1(7), pp. 742–753, 1984.

[95] A. Loot and V. Hizhnyakov, "Transfer-matrix method for second-order nonlinear processes with realistic beams," *arXiv:1707.00461 [physics.optics]*, pp. 1–5, 2017.

[96] T. Ning, H. Pietarinen, O. Hyvärinen, J. Simonen, G. Genty and M. Kauranen, "Strong second-harmonic generation in silicon nitride films," *Applied Physics Letters*, 100(16), pp. 21–25, 2012.

[97] S. V. Andersen and K. Pedersen, "Second-harmonic generation from electron beam deposited SiO films," *Optics Express*, 20(13), p. 13857, 2012.

[98] G. Wang, G. T. Kiehne, G. K. L. Wong, J. B. Ketterson, X. Liu and R. P. H. Chang, "Large second harmonic response in ZnO thin films," *Applied Physics Letters*, 80(3), pp. 401–403, 2002.

[99] H. Cao, J. Y. Wu, H. C. Ong, J. Y. Dai and R. P. H. Chang, "Second harmonic generation in laser ablated zinc oxide thin films," *Applied Physics Letters*, 73(5), pp. 572–574, 1998.

[100] R. M. Corless and N. Fillion, A Graduate Introduction to Numerical Methods, Springer New York, New York, NY, 2013.

[101] L. Delves and J. N. Lyness, "A Numerical Method for Locating the Zeros of an Analytic Function," 1966.

[102] S. Teitler and B. W. Henvis, "Refraction in anisotropic stratified media," *J. Opt. Soc. Am.*, 60(830), 1966.

[103] D. W. Berreman, "Optics in Stratified and Anisotropic Media: 4x4-Matrix Formulation," *Journal of the Optical Society of America*, 62(4), pp. 502–510, 1972.

[104] K. Eidner, "Light propagation in stratified anisotropic media: orthogonality and symmetry properties of the 4x4 matrix formalisms," *Journal of the Optical Society of America A*, 6(11), p. 1657, 1989.

[105] B. Tatian, "Fitting refractive-index data with the Sellmeier dispersion formula." *Applied optics*, 23(24), p. 4477, 1984.

[106] J. Connolly, B. DiBenedetto and R. Donadio, "Specifications Of Raytran Material," *SPIE*, 181(141), 1979.

[107] V. Hizhnyakov and A. Loot, "Spontaneous down conversion of surface plasmon polaritons: strong-field consideration," *arXiv:1609.08329 [physics.optics]*, 2016.

Publications

Curriculum vitae

Personal data:

Name:	Ardi Loot
Date of birth:	September 25, 1990
Citizenship:	Estonian
Telephone:	+372 5280132
Email:	ardi.loot@ut.ee

Education:

2012 – 2014	University of Tartu, Master's studies, Physics
2013 – 2014	University of Toronto, Canada (one semester)
2009 – 2012	University of Tartu, Bachelor's studies, Physics
2006 – 2009	Hugo Treffner's High School, secondary education

Employment:

2016 – ...	University of Tartu, Institute of Physics, Engineer
09.2014 – 2015	University of Tartu, Institute of Physics, Specialist
2010 – 09.2014	University of Tartu, Institute of Physics, Laboratory Assistant

Awards:

2014	3rd prize at scholarship contest organized by Estonian Research Council
2012	1st prize at scholarship contest organized by Estonian Research Council

Elulookirjeldus

Isikuandmed:

Nimi:	Ardi Loot
Sünniaeg:	25.09.1990
Kodakondsus:	Eesti
Telefon:	+372 5280132
E-post:	ardi.loot@ut.ee

Haridustee:

2012 – 2014	Tartu Ülikool, magistriõpe, füüsika
2013 – 2014	Toronto Ülikool, Kanada (üks semester)
2009 – 2012	Tartu Ülikool, bakalaureuseõpe, füüsika
2006 – 2009	Hugo Treffneri Gümnaasium, keskharidus

Teenistuskäik:

2016 – ...	Tartu Ülikooli Füüsika Instituut, insener
09.2014 – 2015	Tartu Ülikooli Füüsika Instituut, spetsialist
2010 – 09.2014	Tartu Ülikooli Füüsika Instituut, laborant

Tunnustus:

2014	III preemia Eesti Teadusagentuur üliõpilaste teadustööde konkursil
2012	I preemia Eesti Teadusagentuur üliõpilaste teadustööde konkursil

DISSERTATIONES PHYSICAE UNIVERSITATIS TARTUENSIS

1. **Andrus Ausmees.** XUV-induced electron emission and electron-phonon interaction in alkali halides. Tartu, 1991.
2. **Heiki Sõnajalg.** Shaping and recalling of light pulses by optical elements based on spectral hole burning. Tartu, 1991.
3. **Sergei Savihhin.** Ultrafast dynamics of F-centers and bound excitons from picosecond spectroscopy data. Tartu, 1991.
4. **Ergo Nõmmiste.** Leelishalogeniidide röntgenelektronemissioon kiiritamisel footonitega energiaga 70–140 eV. Tartu, 1991.
5. **Margus Rätsep.** Spectral gratings and their relaxation in some low-temperature impurity-doped glasses and crystals. Tartu, 1991.
6. **Tõnu Pullerits.** Primary energy transfer in photosynthesis. Model calculations. Tartu, 1991.
7. **Olev Saks.** Attoampri diapasoonis voolude mõõtmise füüsikalised alused. Tartu, 1991.
8. **Andres Virro.** AlGaAsSb/GaSb heterostructure injection lasers. Tartu, 1991.
9. **Hans Korge.** Investigation of negative point discharge in pure nitrogen at atmospheric pressure. Tartu, 1992.
10. **Jüri Maksimov.** Nonlinear generation of laser VUV radiation for high-resolution spectroscopy. Tartu, 1992.
11. **Mark Aizengendler.** Photostimulated transformation of aggregate defects and spectral hole burning in a neutron-irradiated sapphire. Tartu, 1992.
12. **Hele Siimon.** Atomic layer molecular beam epitaxy of A^2B^6 compounds described on the basis of kinetic equations model. Tartu, 1992.
13. **Tõnu Reinot.** The kinetics of polariton luminescence, energy transfer and relaxation in anthracene. Tartu, 1992.
14. **Toomas Rõõm.** Paramagnetic H^{2-} and F^+ centers in CaO crystals: spectra, relaxation and recombination luminescence. Tallinn, 1993.
15. **Erko Jalviste.** Laser spectroscopy of some jet-cooled organic molecules. Tartu, 1993.
16. **Alvo Aabloo.** Studies of crystalline celluloses using potential energy calculations. Tartu, 1994.
17. **Peeter Paris.** Initiation of corona pulses. Tartu, 1994.
18. **Павел Рубин.** Локальные дефектные состояния в CuO_2 плоскостях высокотемпературных сверхпроводников. Тарту, 1994.
19. **Olavi Ollikainen.** Applications of persistent spectral hole burning in ultrafast optical neural networks, time-resolved spectroscopy and holographic interferometry. Tartu, 1996.
20. **Ülo Mets.** Methodological aspects of fluorescence correlation spectroscopy. Tartu, 1996.
21. **Mikhail Danilkin.** Interaction of intrinsic and impurity defects in CaS:Eu luminophors. Tartu, 1997.

22. **Ирина Кудрявцева.** Создание и стабилизация дефектов в кристаллах KBr, KCl, RbCl при облучении ВУФ-радиацией. Тарту, 1997.
23. **Andres Osvet.** Photochromic properties of radiation-induced defects in diamond. Tartu, 1998.
24. **Jüri Örd.** Classical and quantum aspects of geodesic multiplication. Tartu, 1998.
25. **Priit Sarv.** High resolution solid-state NMR studies of zeolites. Tartu, 1998.
26. **Сергей Долгов.** Электронные возбуждения и дефектообразование в некоторых оксидах металлов. Тарту, 1998.
27. **Kaupo Kukli.** Atomic layer deposition of artificially structured dielectric materials. Tartu, 1999.
28. **Ivo Heinmaa.** Nuclear resonance studies of local structure in $RBa_2Cu_3O_{6+x}$ compounds. Tartu, 1999.
29. **Aleksander Shelkan.** Hole states in CuO_2 planes of high temperature superconducting materials. Tartu, 1999.
30. **Dmitri Nevedrov.** Nonlinear effects in quantum lattices. Tartu, 1999.
31. **Rein Ruus.** Collapse of 3d (4f) orbitals in 2p (3d) excited configurations and its effect on the x-ray and electron spectra. Tartu, 1999.
32. **Valter Zazubovich.** Local relaxation in incommensurate and glassy solids studied by Spectral Hole Burning. Tartu, 1999.
33. **Indrek Reimand.** Picosecond dynamics of optical excitations in GaAs and other excitonic systems. Tartu, 2000.
34. **Vladimir Babin.** Spectroscopy of exciton states in some halide macro- and nanocrystals. Tartu, 2001.
35. **Toomas Plank.** Positive corona at combined DC and AC voltage. Tartu, 2001.
36. **Kristjan Leiger.** Pressure-induced effects in inhomogeneous spectra of doped solids. Tartu, 2002.
37. **Helle Kaasik.** Nonperturbative theory of multiphonon vibrational relaxation and nonradiative transitions. Tartu, 2002.
38. **Tõnu Laas.** Propagation of waves in curved spacetimes. Tartu, 2002.
39. **Rünno Lõhmus.** Application of novel hybrid methods in SPM studies of nanostructural materials. Tartu, 2002.
40. **Kaido Reivelt.** Optical implementation of propagation-invariant pulsed free-space wave fields. Tartu, 2003.
41. **Heiki Kasemägi.** The effect of nanoparticle additives on lithium-ion mobility in a polymer electrolyte. Tartu, 2003.
42. **Villu Repän.** Low current mode of negative corona. Tartu, 2004.
43. **Алексей Котлов.** Оксианионные диэлектрические кристаллы: зонная структура и электронные возбуждения. Tartu, 2004.
44. **Jaak Talts.** Continuous non-invasive blood pressure measurement: comparative and methodological studies of the differential servo-oscillometric method. Tartu, 2004.
45. **Margus Saal.** Studies of pre-big bang and braneworld cosmology. Tartu, 2004.

46. **Eduard Gerškevitš.** Dose to bone marrow and leukaemia risk in external beam radiotherapy of prostate cancer. Tartu, 2005.
47. **Sergey Shchemelyov.** Sum-frequency generation and multiphoton ionization in xenon under excitation by conical laser beams. Tartu, 2006.
48. **Valter Kiisk.** Optical investigation of metal-oxide thin films. Tartu, 2006.
49. **Jaan Aarik.** Atomic layer deposition of titanium, zirconium and hafnium dioxides: growth mechanisms and properties of thin films. Tartu, 2007.
50. **Astrid Rekker.** Colored-noise-controlled anomalous transport and phase transitions in complex systems. Tartu, 2007.
51. **Andres Punning.** Electromechanical characterization of ionic polymer-metal composite sensing actuators. Tartu, 2007.
52. **Indrek Jõgi.** Conduction mechanisms in thin atomic layer deposited films containing TiO_2. Tartu, 2007.
53. **Aleksei Krasnikov.** Luminescence and defects creation processes in lead tungstate crystals. Tartu, 2007.
54. **Küllike Rägo.** Superconducting properties of MgB_2 in a scenario with intra- and interband pairing channels. Tartu, 2008.
55. **Els Heinsalu.** Normal and anomalously slow diffusion under external fields. Tartu, 2008.
56. **Kuno Kooser.** Soft x-ray induced radiative and nonradiative core-hole decay processes in thin films and solids. Tartu, 2008.
57. **Vadim Boltrushko.** Theory of vibronic transitions with strong nonlinear vibronic interaction in solids. Tartu, 2008.
58. **Andi Hektor.** Neutrino Physics beyond the Standard Model. Tartu, 2008.
59. **Raavo Josepson.** Photoinduced field-assisted electron emission into gases. Tartu, 2008.
60. **Martti Pärs.** Study of spontaneous and photoinduced processes in molecular solids using high-resolution optical spectroscopy. Tartu, 2008.
61. **Kristjan Kannike.** Implications of neutrino masses. Tartu, 2008.
62. **Vigen Issahhanjan.** Hole and interstitial centres in radiation-resistant MgO single crystals. Tartu, 2008.
63. **Veera Krasnenko.** Computational modeling of fluorescent proteins. Tartu, 2008.
64. **Mait Müntel.** Detection of doubly charged higgs boson in the CMS detector. Tartu, 2008.
65. **Kalle Kepler.** Optimisation of patient doses and image quality in diagnostic radiology. Tartu, 2009.
66. **Jüri Raud.** Study of negative glow and positive column regions of capillary HF discharge. Tartu, 2009.
67. **Sven Lange.** Spectroscopic and phase-stabilisation properties of pure and rare-earth ions activated ZrO_2 and HfO_2. Tartu, 2010.
68. **Aarne Kasikov.** Optical characterization of inhomogeneous thin films. Tartu, 2010.
69. **Heli Valtna-Lukner.** Superluminally propagating localized optical pulses. Tartu, 2010.

70. **Artjom Vargunin.** Stochastic and deterministic features of ordering in the systems with a phase transition. Tartu, 2010.
71. **Hannes Liivat.** Probing new physics in e+e− annihilations into heavy particles via spin orientation effects. Tartu, 2010.
72. **Tanel Mullari.** On the second order relativistic deviation equation and its applications. Tartu, 2010.
73. **Aleksandr Lissovski.** Pulsed high-pressure discharge in argon: spectroscopic diagnostics, modeling and development. Tartu, 2010.
74. **Aile Tamm.** Atomic layer deposition of high-permittivity insulators from cyclopentadienyl-based precursors. Tartu, 2010.
75. **Janek Uin.** Electrical separation for generating standard aerosols in a wide particle size range. Tartu, 2011.
76. **Svetlana Ganina.** Hajusandmetega ülesanded kui üks võimalus füüsikaõppe efektiivsuse tõstmiseks. Tartu, 2011
77. **Joel Kuusk.** Measurement of top-of-canopy spectral reflectance of forests for developing vegetation radiative transfer models. Tartu, 2011.
78. **Raul Rammula**. Atomic layer deposition of HfO_2 – nucleation, growth and structure development of thin films. Tartu, 2011.
79. **Сергей Наконечный.** Исследование электронно-дырочных и интерстициал-вакансионных процессов в монокристаллах MgO и LiF методами термоактивационной спектроскопии. Тарту, 2011.
80. **Niina Voropajeva.** Elementary excitations near the boundary of a strongly correlated crystal. Tartu, 2011.
81. **Martin Timusk.** Development and characterization of hybrid electro-optical materials. Tartu, 2012, 106 p.
82. **Merle Lust.** Assessment of dose components to Estonian population. Tartu, 2012, 84 p.
83. **Karl Kruusamäe.** Deformation-dependent electrode impedance of ionic electromechanically active polymers. Tartu, 2012, 128 p.
84. **Liis Rebane.** Measurement of the $W \to \tau\nu$ cross section and a search for a doubly charged Higgs boson decaying to τ-leptons with the CMS detector. Tartu, 2012, 156 p.
85. **Jevgeni Šablonin.** Processes of structural defect creation in pure and doped MgO and NaCl single crystals under condition of low or super high density of electronic excitations. Tartu, 2013, 145 p.
86. **Riho Vendt**. Combined method for establishment and dissemination of the international temperature scale. Tartu, 2013, 108 p.
87. **Peeter Piksarv.** Spatiotemporal characterization of diffractive and non-diffractive light pulses. Tartu, 2013, 156 p.
88. **Anna Šugai.** Creation of structural defects under superhigh-dense irradiation of wide-gap metal oxides. Tartu, 2013, 108 p.
89. **Ivar Kuusik.** Soft X-ray spectroscopy of insulators. Tartu, 2013, 113 p.
90. **Viktor Vabson**. Measurement uncertainty in Estonian Standard Laboratory for Mass. Tartu, 2013, 134 p.

91. **Kaupo Voormansik.** X-band synthetic aperture radar applications for environmental monitoring. Tartu, 2014, 117 p.
92. **Deivid Pugal.** hp-FEM model of IPMC deformation. Tartu, 2014, 143 p.
93. **Siim Pikker.** Modification in the emission and spectral shape of photostable fluorophores by nanometallic structures. Tartu, 2014, 98 p.
94. **Mihkel Pajusalu**. Localized Photosynthetic Excitons. Tartu, 2014, 183 p.
95. **Taavi Vaikjärv.** Consideration of non-adiabaticity of the Pseudo-Jahn-Teller effect: contribution of phonons. Tartu, 2014, 129 p.
96. **Martin Vilbaste.** Uncertainty sources and analysis methods in realizing SI units of air humidity in Estonia. Tartu, 2014, 111 p.
97. **Mihkel Rähn.** Experimental nanophotonics: single-photon sources- and nanofiber-related studies. Tartu, 2015, 107 p.
98. **Raul Laasner.** Excited state dynamics under high excitation densities in tungstates. Tartu, 2015, 125 p.
99. **Andris Slavinskis.** EST Cube-1 attitude determination. Tartu, 2015, 104 p.
100. **Karlis Zalite**. Radar Remote Sensing for Monitoring Forest Floods and Agricultural Grasslands. Tartu, 2016, 124 p.
101. **Kaarel Piip.** Development of LIBS for *in-situ* study of ITER relevant materials. Tartu, 2016, 93 p.
102. **Kadri Isakar.** ^{210}Pb in Estonian air: long term study of activity concentrations and origin of radioactive lead. Tartu, 2016, 107 p.
103. **Artur Tamm.** High entropy alloys: study of structural properties and irradiation response. Tartu, 2016, 115 p.
104. **Rasmus Talviste.** Atmospheric-pressure He plasma jet: effect of dielectric tube diameter. Tartu, 2016, 107 p.
105. **Andres Tiko.** Measurement of single top quark properties with the CMS detector. Tartu, 2016, 161 p.
106. **Aire Olesk.** Hemiboreal Forest Mapping with Interferometric Synthetic Aperture Radar. Tartu, 2016, 121 p.
107. **Fred Valk.** Nitrogen emission spectrum as a measure of electric field strength in low-temperature gas discharges. Tartu, 2016, 149 p.
108. **Manoop Chenchiliyan.** Nano-structural Constraints for the Picosecond Excitation Energy Migration and Trapping in Photosynthetic Membranes of Bacteria. Tartu, 2016, 115p.
109. **Lauri Kaldamäe.** Fermion mass and spin polarisation effects in top quark pair production and the decay of the higgs boson. Tartu, 2017, 104 p.
110. **Marek Oja.** Investigation of nano-size α- and transition alumina by means of VUV and cathodoluminescence spectroscopy. Tartu, 2017, 89 p.
111. **Viktoriia Levushkina.** Energy transfer processes in the solid solutions of complex oxides. Tartu, 2017, 101 p.
112. **Mikk Antsov.** Tribomechanical properties of individual 1D nanostructures: experimental measurements supported by finite element method simulations. Tartu, 2017, 101 p.
113. **Hardi Veermäe.** Dark matter with long range vector-mediated interactions. Tartu, 2017, 137 p.

114. **Aris Auzans.** Development of computational model for nuclear energy systems analysis: natural resources optimisation and radiological impact minimization. Tartu, 2018, 138 p.
115. **Aleksandr Gurev**. Coherent fluctuating nephelometry application in laboratory practice. Tartu, 2018, 150 p.